UNIVERSITÀ DEGLI STUDI DI PADOVA

UNIVERSITÀ DEGLI STUDI DI PADOVA

Dipartimento di Ingegneria Industriale DII

Corso di Laurea Magistrale in Ingegneria dei Materiali

Correlation between cross-linking of the rubbery phase and aesthetic properties in ABS copolymers

Relatore: Chiar.mo Prof. Michele Modesti

Co-relatore: Dott. Dino Ferri

Co-relatore: Ing. Silvia Zanatta

Candidata: Laura Ongari

Matricola: 1205731

Anno Accademico 2022/2023

Abstract

This thesis work, carried out at the Rheology laboratory of *Eni Versalis S.p.a.*, was started with the aim of investigating why ABS copolymers appear significantly different in terms of gloss, with only a change in the swelling index. This is an indirect measure of cross-linking degree of the rubber particles inside ABS. Aesthetic defects in injection-molded objects, such as the gloss transition, must be mitigated as they lead to poor surface quality. Furthermore, in certain types of products, gloss is a fundamental property that must be enhanced. It is known that gloss depends on molding conditions, such as injection speed and mold temperature. In literature, a dimensionless parameter has been proposed, called replication factor *R*, as responsible for the gloss value. It is defined as the ratio between the pressure, to which the melt is subjected during the injection, and the Young's modulus *E* of the polymer layer in contact with the mold wall. The pressure generated by the melt acts as a driving force for replication and is related to injection speed and polymer viscosity. The increasing surface stiffness, during the cooling below the glass transition temperature (T_g), acts as a replication resistance factor and is also related to molding conditions, such as injection speed and mold temperature. A high replication factor is therefore the key point to achieve excellent surface quality. However, this parameter alone cannot explain the different gloss values obtained for the samples at study. These differ for the swelling index value but possess the same *R* value. It will be proposed that the difference in glossiness is due to the behavior exhibited by the polymer when stretched in the molten state, particularly to its elongational viscosity. It is in fact known that during the filling stage, the flow front presents a divergence giving rise to the so-called "fountain flow", in which the melt is subjected to very strong elongational stresses. These generate a stronger different orientation of the matrix polymer chains and of the rubber particles on the surface, which show a stretched shape, especially for the sample with more deformable particles (higher swelling index). In any case, many aspects, such as surface roughness, will be investigated to understand how differences in the cross-linking of the rubber can significantly affect gloss.

Riassunto

Il presente lavoro di tesi, principalmente svolto presso il laboratorio di Reologia del centro ricerche di *Eni Versalis S.p.a*, è nato con l'obiettivo di indagare il motivo per cui copolimeri ABS appaiano sensibilmente diversi in termini di lucentezza (*gloss*), con la sola variazione dell'indice di rigonfiamento (*swelling index*). Quest'ultimo rappresenta una misura indiretta del grado di reticolazione delle particelle di gomma presenti nell'ABS. I difetti estetici in oggetti stampati ad iniezione, come ad esempio la transizione *gloss-matt*, devono essere attenuati poiché conducono ad una cattiva qualità superficiale. Inoltre, in alcune tipologie di prodotti, la lucentezza è proprietà fondamentale che va quindi esaltata. È noto che il *gloss* dipende dalle condizioni di stampaggio, quali velocità di iniezione e temperatura dello stampo. In letteratura viene proposto un numero adimensionale, detto fattore di replicazione *R* (*replication factor*), come variabile in grado di predire il *gloss*. *R* è definito come il rapporto tra la pressione a cui è sottoposto il fuso durante l'iniezione e il modulo di Young *E* del sottile strato di polimero a contatto con la superficie dello stampo. La pressione generata dal fuso agisce come forza motrice per la replicazione ed è correlata alla velocità di iniezione ed alla viscosità del polimero. Il crescente modulo di Young, durante il processo di raffreddamento al di sotto della temperatura di transizione vetrosa (T_g), agisce invece come fattore resistente alla replicazione ed è anch'esso legato alle condizioni di stampaggio, quali velocità di iniezione e temperatura dello stampo. Un alto fattore di replicazione favorisce quindi l'ottenimento di un'ottima qualità superficiale. Tuttavia, non è l'unico parametro in gioco, infatti non riesce a dare la spiegazione dei diversi valori di *gloss* ottenuti per i campioni in oggetto. Quest'ultimi risultano infatti avere diverso indice di rigonfiamento ma identico valore di *R*. Verrà proposto che ciò che differenzia maggiormente i campioni è il comportamento mostrato dal polimero quando stirato allo stato fuso, ed in particolare la sua viscosità elongazionale. È infatti noto che, durante il riempimento di uno stampo, la divergenza del fronte di avanzamento del fuso da luogo al cosiddetto flusso a fontana (*fountain flow*), che lo sottopone a stress elongazionali molto forti. Ciò provoca una elevata orientazione sia delle catene polimeriche della matrice che delle particelle di

gomma in superficie, le quali risultano particolarmente stirate, in special modo per il campione con particelle più deformabili (indice di rigonfiamento maggiore). È proprio il recupero elastico delle particelle deformate che da origine alla rugosità superficiale, fonte di scattering della luce e del grado di opacità delle superfici. Il presente lavoro ha coinvolto numerosi laboratori ed ha portato alla luce numerosi aspetti finora sconosciuti all'azienda. Dalla caratterizzazione reologica dei campioni si sono indagati molti altri aspetti come la correlazione *gloss*-rugosità superficiale definita dal modello analitico di Simonsen. Il laboratorio di Ricerca e Sviluppo ha permesso la valutazione del *gloss* su placchette ottenute in diverse condizioni di stampaggio. Dal momento che è stato ottenuto un risultato in lieve controtendenza con quanto atteso, è stata di fondamentale importanza la collaborazione con il laboratorio di controllo, che ha altresì condotto ad interessanti considerazioni. La più importante, specialmente dal punto di vista produttivo, si è mostrata essere la variazione del grado di reticolazione della gomma durante il processo di stampaggio ad iniezione. È poi stata indagata una correlazione tra viscosità elongazionale e indice di rigonfiamento che potrebbe portare allo sviluppo futuro di un metodo reologico per la più semplice e veloce determinazione di quest'ultimo. Grazie alla collaborazione con il laboratorio di Microscopia abbiamo infine ottenuto importanti informazioni sulla diversa morfologia delle superfici delle placchette. Da queste è nata l'idea di un possibile affioramento delle particelle meno deformabili in superficie, che risultano anch'esse fonte di rugosità superficiale. Nonostante la migrazione laterale di particelle deformabili sia un fenomeno reale, ad oggi è studiato solamente in microfluidica attraverso laboriose simulazioni. Visti i promettenti risultati che potrebbero effettivamente dimostrare una causa a livello microscopico di un effetto macroscopico, quale è la lucentezza, sono in corso delle simulazioni in collaborazione con l'Università di Napoli. Il presente lavoro si è quindi rivelato molto utile nella comprensione di alcune complesse correlazioni proprietà-struttura.

Preface

Purpose of this thesis work is to try to understand the mechanisms and the reasons why ABS products with different swelling index values, have significantly different gloss values. The problem was born in *Eni Versalis S.p.a* when during a production campaign of ABS, the devolatilization temperature, which is applied at the end of the production for the removal of excess monomers and to properly cross-link the rubbery phase, was lowered. This led to higher swelling index values, and during the production sampling, the Quality Control laboratory (QC) found that gloss was significantly lowered. In the meanwhile, the devolatilization temperature has been raised up, the gloss recovered the standard specification values and some samples have been collected for subsequent analysis. It was found that samples had very similar structural property, except for the swelling index value, that is a different degree of crosslinking of the rubbery phase. It is known by the literature that molding conditions do affect glossiness together with structural parameters as for example the particle dimensions. No evidence has been reported in the literature to the best of our knowledge for the effect, if there is any, of the swelling index on the gloss values. The rheological properties of three ABS samples with different swelling index values, ranging from 16 to 34, were investigated in detail. These samples were also injection molded using both the Research and Development (R&D) and the Quality Control (QC) laboratories equipment using a matrix of different mold temperature and injection speed conditions to highlight and investigate gloss values trends. A possible correlation between the degree of crosslinking of the polybutadiene particles and the rheological and aesthetic properties of the injection molded samples is also proposed at the end of the work and represents the original part of this thesis.

Table of Contents

INTRODUCTION

The term “polymer” derives from the Greek *“poli”* (many) and *“meros”* (units) and is used to describe a material with long macromolecules, basically formed by carbon and hydrogen atoms. Nowadays plastic materials are present in many common objects thanks to their outstanding properties like low density, corrosion resistance, easy manufacturing, and relatively low cost. They have even disadvantages like low strength, low stiffness, low useful temperature range, flammability, etc. However, continuous research allows to improve some critical aspects. Particular attention should be paid to the mechanical behavior of these materials because they are viscoelastic. This means that they show a behavior between a perfectly elastic solid and a purely viscous liquid. For these types of materials rheology assumes an important role because it permits to study how materials behave when subjected to several states of stress or deformation. In 1929 Bingham defined rheology as *“the study of the deformation and flow of the matter”*. A meaningful example to understand the importance of rheology is the pitch drop experiment, where some pitch is contained in a funnel, free to flow through it. This experiment was started in 1927 at University of Queensland (Australia) and it is still in progress. The fundamental question is: is the pitch solid or liquid? It depends. If you hit the pitch with a hammer, pitch would break like a brittle solid but leaving the pitch in the funnel, it flows under the effect of its weight, although very slowly (one drop falls every eight/nine years). So, what changes is the stress condition to which the pitch is subjected as well as the observation time of the experiment.

This thesis will be focused on rubber-toughened styrene copolymers, particularly on Acrylonitrile-Butadiene-Styrene terpolymers (ABS). In the late 1940s, the demand of styrene monomer, acrylonitrile, and styrene-butadiene rubber (SBR) declined drastically.[1] For this reason, the rubber modification of polystyrene and styrene-acrylonitrile copolymers (SAN) became of industrial interest. ABS is used mainly in automobile manufacturing, appliances, electronics, pipes and, in general, to produce uncountable parts thanks to its high durability. PS and SAN are transparent and brittle thermoplastic materials but, with the addition of small, dispersed rubber particles, the

impact resistance and toughness increase considerably. In the past, the rubbery phase was made of SBR but nowadays this is replaced by polybutadiene (PB) thanks to its lower glass-transition temperature (-85°C) that results in an improvement of the low-temperature impact strength. This property is important in applications at low temperature, such as internal parts of refrigerators. The most significant structural properties of these two-phase materials are the molecular weight of the matrix, the volume fraction of disperse phase, the morphology of the particles, the particles size and distribution as well as the rubber degree of cross-linking. It is known that the addition of rubber particles to SAN leads to opacity and mattness. However, it is possible to obtain a glossy material if rubber particles are very small (lower than 1 μm). In the present work it will be discussed how and why processing conditions and material's characteristics, particularly the cross-linking degree of the rubbery phase, can affect the aesthetic appearance of the final product.

1 Acrylonitrile-Butadiene-Styrene Copolymers (ABS)

Acrylonitrile-Butadiene-Styrene terpolymers (ABS) are very versatile thermoplastic materials used in many applications, such as automotive, appliances, pipes, etc. Figure 1.1 shows the structural formula of ABS.

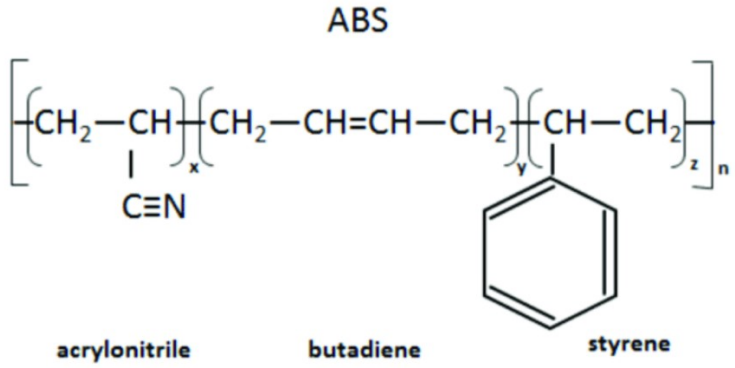

Figure 1. 1: *Structural formula of ABS (Acrylonitrile-Butadiene-Styrene) copolymer.*[2]

An ABS is substantially composed by a glassy matrix, made of SAN, with small, dispersed particles of rubber, mostly polybutadiene, which confers the impact strength to ABS. SAN is a styrene-acrylonitrile copolymer, typically used in applications which require high chemical resistance, high rigidity, and transparency.

1.1 Monomers

Styrene monomer is obtained by the dehydrogenation of ethylbenzene derived from Friedel-Crafts reaction of ethylene and benzene.

$$C_6H_6 + C_2H_4 \xrightarrow[AlCl_3]{} C_6H_5CH_2CH_3 \xrightarrow[600℃]{} C_6H_5CHCH_2 + H_2 \quad (1.\ 1)$$

Acrylonitrile is industrially produced by the propylene ammoxidation.

$$CH_2CHCH_3 + NH_3 + \frac{1}{2}O_2 \leftrightarrow CH_2CHCN + 3H_2O \quad (1.2)$$

1,3-butadiene ($CH_2CHCHCH_2$) is a petroleum hydrocarbon obtained from the C_4 fraction of steam cracking.[3]

1.2 Production of ABS

ABS copolymers can be made by bulk or emulsion polymerization.[1] Bulk process consists of polymerizing SAN in the presence of dissolved rubber. First, the rubber is dissolved in the monomers and when the polymerization begins, the monomers are copolymerized among themselves and as a graft on the rubber. Consequently, in the monomer there are two dissolved phases: the polymer and the rubber. Initially, the quantity of polymer in the monomer phase is lower compared to the rubber in the monomer phase but, as the polymerization proceeds, the polymer in the monomer phase becomes greater in volume. At this point, phase inversion occurs and the rubber in the monomer phase becomes dispersed as particles in polymer in the monomer phase. For this reason, in mass polymerization, rubber particles contain inclusions of matrix material. Emulsion is a discontinuous process which runs in several steps. The first is the production of a polybutadiene latex. Since butadiene polymerizes slowly, to reduce the cycle period, the reaction is stopped before the completion and small particles are made. So, a subsequent agglomeration step is necessary to achieve the optimum size and a grafting step follows the agglomeration. This consists of a seeded polymerization that cover the rubber particles with a matrix shell, thanks to the simultaneous presence of an initiator and matrix monomers. Finally, the graft dispersion is mixed with the matrix SAN dispersion. The latex mixture is then precipitated, washed, dried, and processed to granules. In general, products derived from mass polymerization are better in terms of mechanical properties showing a good balance between high impact resistance and modulus. Emulsion products are better in terms of aesthetic properties showing also good mechanical properties. These differences are due to different morphology, size and distribution of rubber particles. ABS produced by emulsion shows a bimodal distribution of spherical rubber particles, while rubber particles of mass products do show a

monomodal distribution with a “salami-like” morphology, like the one shown in Figure 1.2.

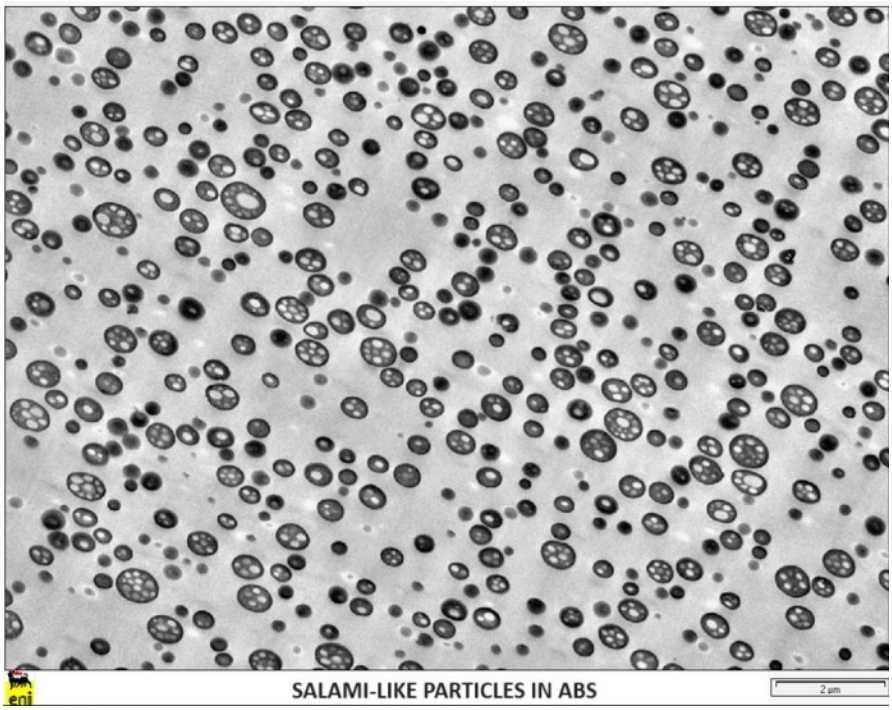

Figure 1. 2: *Salami-like morphology of rubber particles in ABS copolymers. The small white dots inside particles are matrix inclusions.*

Matrix molecular weight, rubber type, phase volume ratio, rubber particle size, particle morphology and cross-link density are all parameters governing technical properties.

1.3 Molecular and Morphological parameters of ABS

Matrix composition and molecular weight are determined by feed composition and reaction conditions. In most cases, the rubber used in ABS is polybutadiene, which is made from emulsion polymerization, usually at 60°C with potassium persulfate as initiator. The microstructure of polybutadiene depends on the reaction temperature, while the cross-link density depends on the final conversion, and generally takes place during the devolatilization phase of residual monomers. Both parameters influence the glass transition temperature, which is around -85°C, while the glass-transition temperature of

styrene is about 100°C. An important parameter is the phase-volume ratio because it affects the impact strength. In general, by increasing the rubber content the Young's modulus and the yield stress decrease but impact strength increases. In general, small rubber particles are preferable to make ABS stiff and gloss, while big particles are efficient to improve toughness. The two phases nature of ABS causes turbidity by light scattering at the dispersed phase. This occurs because normally particles are larger than the wavelength of visible light (400÷700 nm) and because they have different refractive index from those of the matrix. Furthermore, it is known that gloss, which relates the amount of specular reflected light from a surface, and then the shine of the product, can be related exponentially to particle size, as it will be shown in §5.2.

1.4 Toughening mechanism in rubber reinforced materials

As already mentioned, the impact resistance of these materials is given by the presence of small, dispersed rubber particles in a solid matrix. The strategy is based on the idea of maximizing the volume of material that participates in the process of energy dissipation during deformation and propagation of fracture. Furthermore, the presence of dispersed rubber particles in a glassy matrix allows to modify the stress field around the inclusions. Thanks to the low glass transition temperature of the rubber, these polymers are suitable for low temperatures applications. Usually, the rubber content present is around 5-20%, although the effective rubber content may be higher than the quantity added because the possible matrix inclusions inside. The adhesion between particles and matrix is fundamental for toughening properties. In general, the matrix and the rubber are chemically incompatible and immiscible so, to obtain this close adhesion, it is necessary to introduce a grafted copolymer, which affects the final dimension of particles and ensure the adhesion between the two phases during the deformation.

2 Mechanical behavior of polymers

2.1 Elastic behavior

The elastic behavior can be described by the Hooke's equation which states a linear relationship between stress, expressed in N/m^2, and deformation:

$$\sigma = E\varepsilon \tag{2. 1}$$

$$\tau = G\gamma \tag{2. 2}$$

Equation (2.1) refers to elongational stress while equation (2.2) refers to shear stress. The proportionality constants, expressed in Pascals, E and G, are the Young's modulus and the shear modulus, respectively, and they depend on the nature of the materials. This proportionality is restricted in a narrow range where the deformation is completely reversible, that is without any plastic deformation and any dissipation of energy. Obviously, this is not realistic but generally, in the case of small deformations, it is reasonable to consider a material as an elastic solid. Figure 2.1 shows the typical stress-strain curve for ductile materials. It is possible to recognize the elastic region and the plastic region in which the material deforms permanently.

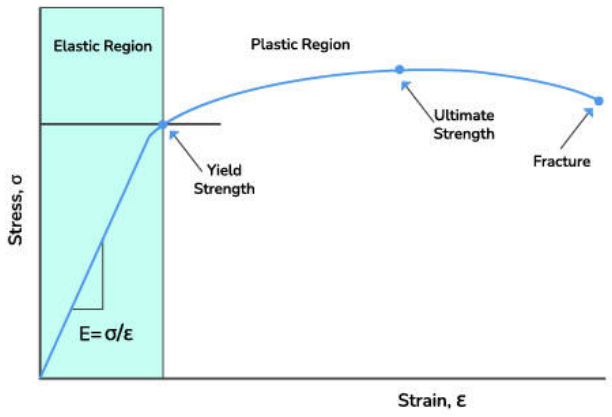

Figure 2.1: *Typical elongational stress-strain curve for ductile materials. In the elastic region the stress is directly proportional to the strain and the constant of proportionality is the Young's modulus E. In the plastic region there is a permanent deformation with dissipation of energy until reaching the fracture.*[4]

Furthermore, in the case of isotropic solids, whose properties are the same in all directions, the elastic behavior is described by three constants: the elastic modulus *E*, the shear modulus *G* and the Poisson's coefficient *v.* *E* and *G* are correlated by the following equation:

$$G = \frac{E}{2(1+\nu)} \tag{2. 3}$$

The Poisson's coefficient is given by the ratio between the lateral contraction and the longitudinal deformation. Obviously for incompressible materials ν is equal to zero.

2.2 Viscous behavior

A purely viscous liquid is described by the Newton's law, which expresses a direct proportionality between the shear stress τ, expressed in Pascals, and the strain rate $\dot{\gamma}$, expressed in s^{-1}, as follows:

$$\tau = \eta\dot{\gamma} \tag{2. 4}$$

Equation (2.4) characterizes Newtonian fluids and the term η represents the dynamic viscosity of the fluid, measured in $\mathrm{Pa}\cdot\mathrm{s}$ or Poise. So, in this case the time of stress application plays an important role. In fact, even if small stresses are applied, but for long periods, they can lead to large effects in terms of deformation. Vice-versa, large stresses can have small effects if applied instantaneously. For most of the fluids, viscosity decreases with increasing temperature and decreasing pressure, although for non-Newtonian fluids the correlation between temperature and viscosity is complex. In 1906 Frederick Thomas Trouton expressed the relationship between the elongational viscosity and the shear viscosity for Newtonian fluids as follows:

$$\eta_{el} = 3\eta \tag{2. 5}$$

As shown in Figure 2.2 there are three types of non-Newtonian time-independent fluids, based on their different behavior.

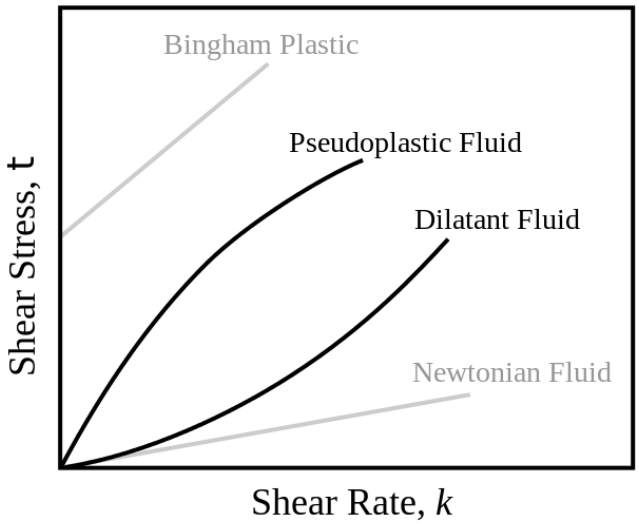

Figure 2. 2: *Shear stress versus shear rate for different types of fluids.*[5]

By increasing the shear rate, the viscosity decreases for pseudoplastic (or shear-thinning) fluids and increases for dilatant (or shear-thickening) fluids. Both are described by a power-law expression:

$$\sigma = K\dot{\gamma}^n \tag{2. 6}$$

K is a constant characteristic of the material an n is defined as flow index. So, pseudoplastic fluids have $n < 1$, while dilatant fluids have $n > 1$. Bingham fluids behave as solids at low stresses but when the stress exceeds a critical value, defined as yield stress, they flow like a viscous liquid.

The long uncross-linked macromolecules of polymers tend to contract to form random coils able to entangle each other. A “poorly entangled” structure has lower flow resistance, and this is the reason of shear-thinning behavior of polymers. Thanks to this property, polymers are suited to produce objects with complicate geometries, that are not only impossible to obtain with other materials, but in addition they allow to reduce consumption of energy and consequently CO_2 emissions. In Figure 2.3 the typical trend of viscosity for a pseudoplastic material is reported. It shows two plateaus at low and high shear rate values, called first and second Newtonian region respectively. The highest viscosity in the first Newtonian region is defined as zero-shear viscosity and is indicated as η_0.

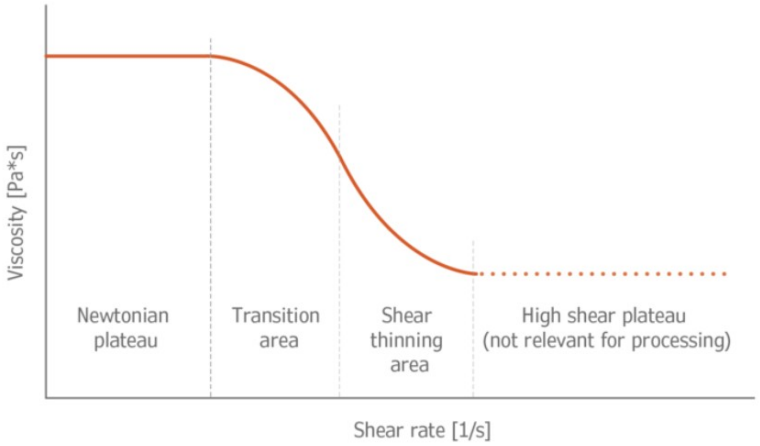

Figure 2. 3: *Viscosity vs. shear rate for pseudoplastic materials. The curve shows three regions: at low shear rates there is a high viscosity plateau called zero-shear viscosity, then there is a transition zone in which the viscosity rapidly drops by increasing the shear rate and the last region, at high shear rates, called low viscosity plateau, in which the viscosity remains low and constant.*[6]

The Cross equation (2.7) is usually a good model for the shear rate dependence of the viscosity:

$$\frac{\eta(\dot{\gamma}) - \eta_\infty}{\eta_0 - \eta_\infty} = \frac{1}{(1 + K\dot{\gamma})^m} \tag{2. 7}$$

K is a time parameter and m a dimensionless parameter equal to $(n - 1)$.

$$\eta(\dot{\gamma}) = \frac{\eta_0}{(K\dot{\gamma})^{(n-1)}} \tag{2. 8}$$

When $\eta(\dot{\gamma}) \ll \eta_0$ and $\eta(\dot{\gamma}) \gg \eta_\infty$ it is possible to approximate (2.7) with the power law previously mentioned, as shown in (2.8).

2.3 Viscoelasticity: somewhere in between

Viscoelasticity is the property of some materials to behave in an intermediate way between an elastic solid and a viscous liquid. Hooke and Newton derived the constitutive equations (2.1) and (2.4) representing extremely ideal cases. In 1964, Reiner defined a dimensionless number, the so-called Deborah number, as the ratio between two characteristic times:

$$De = \frac{\tau_{mat}}{\tau_{exp}} \tag{2. 9}$$

Where τ_{mat} is the relaxation time of the material and τ_{exp} is the characteristic time of the experiment. High De mainly result in a predominantly elastic behavior, while low De correspond to a predominantly liquid behavior. In this way, a material can behave as an elastic solid due to high τ_{mat} or because the process it is involved in is very fast (low τ_{exp}).

2.3.1 Viscoelastic models

It is possible to represent linear viscoelasticity using Equation (2.10) in which the stress is given by both the elastic and viscous contributions [7]:

$$\tau = G\gamma + \eta\dot{\gamma} \tag{2. 10}$$

The viscoelastic behavior of materials can be described thanks to constitutive equations derived from two significant empirical models obtained combining springs and dashpots: the Maxwell and the Voigt models. The Maxwell model consists of a purely elastic spring and a purely viscous damper placed in series, as reported in Figure 2.4. The stress is the same for both elements while the deformation is given by the sum of two different contributions. It describes qualitatively well the phenomenon of stress relaxation, as shown in Figure 2.5, for which imposing a constant deformation the stress decreases over time.

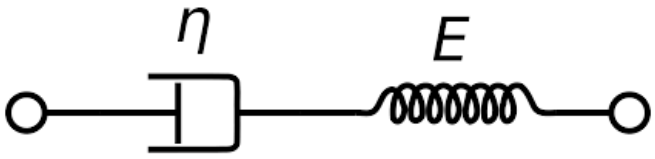

Figure 2. 4: *Maxwell model. It consists of a purely elastic spring and a purely viscous damper placed in series. It describes the stress-relaxation phenomenon for which imposing a constant deformation the stress decreases over time.*[8]

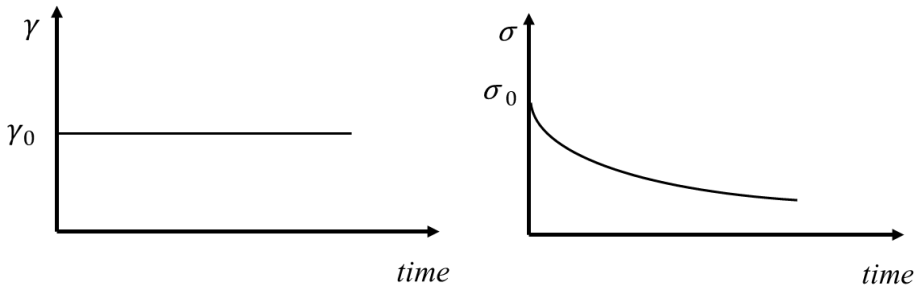

Figure 2. 5: *Maxwell model curves. The left graph represents the constant deformation applied over time and the right one the decreasing stress over time.*

Equations (2.11) and (2.12) show the exponential decrease of the stress and define and contain the characteristic relaxation time of the material (λ), respectively:

$$\sigma(t) = \sigma_0 e^{\left(-\frac{t}{\lambda}\right)} \tag{2. 11}$$

$$\lambda = \frac{\eta}{G} \tag{2. 12}$$

The Voigt model consists of a purely elastic spring and a purely viscous damper placed in parallel, as shown in Figure 2.6. It describes qualitatively well the phenomenon of creep as shown in Figure 2.7, performed imposing a constant stress and measuring the deformation increase over time. In this configuration the stress is shared by the two elements while the deformation is equal for both.

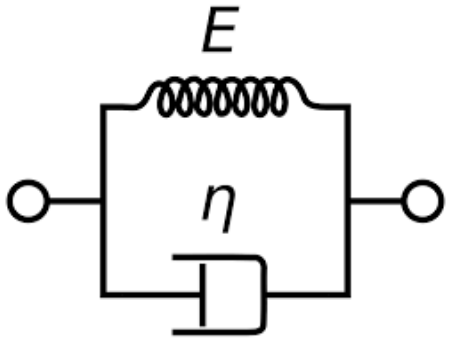

Figure 2. 6: *Voigt model. It consists of a purely elastic spring and a purely viscous damper placed in parallel. It represents the creep phenomenon for which imposing a constant stress the deformation increases over time.*[8]

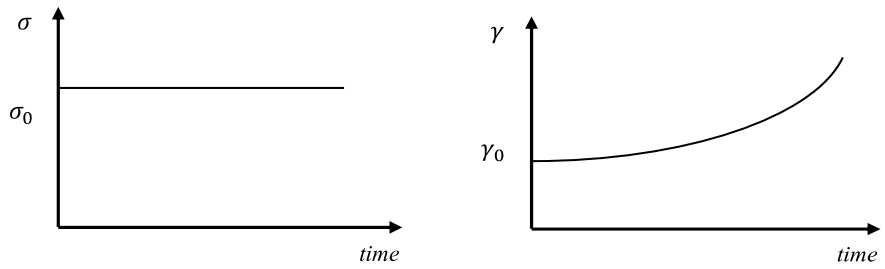

Figure 2. 7: *Voigt model curves. The right graph represents the constant stress applied over time and the right one the increasing deformation over time.*

The following constitutive equation expresses the increase in time of deformation:

$$\gamma(t) = \gamma_0 e^{\left(-\frac{t}{\lambda}\right)} \tag{2. 13}$$

2.3.2 Viscoelasticity in oscillatory regime

Dynamic mechanical analysis (DMA) allows to study viscoelastic systems and gives information on materials when they are subjected to oscillatory stresses. Assuming to impose on the material a sinusoidal solicitation, the deformation $\gamma(t)$ and the strain rate $\dot{\gamma}(t)$ are given by:

$$\gamma(t) = \gamma_0 sin(\omega t) \tag{2. 14}$$

$$\dot{\gamma}(t) = \gamma_0 \omega \, cos(\omega t) \tag{2. 15}$$

Where ω is the angular frequency, in rad/s, and γ_0 the amplitude. For a purely elastic solid, stress and strain are proportional and in phase as stated by the Hooke's law:

$$\sigma(t) = G\gamma_0 \, sin(\omega t) \tag{2. 16}$$

For a purely viscous liquid, the Newton's equation (2.4) states the proportionality between the stress and the strain rate. Then, stress and strain are out of phase by $\pi/2$:

$$\sigma(t) = \eta\gamma_0 \omega \, cos(\omega t) \tag{2. 17}$$

For a viscoelastic material, the stress is given by:

$$\sigma(t) = \sigma_0 \, sin(\omega t + \delta) \tag{2. 18}$$

Where $\sigma_0 = G\gamma_0$ and δ is the phase shift angle. If $\delta = 0$, equation (2.18) degenerates in equation (2.16), while if $\delta = {}^{\pi}/_{2}$, equation (2.18) degenerates in equation (2.17), expressing the case of a viscous liquid. Figure 2.8 shows the purely elastic, the purely viscous and the viscoelastic behaviors.

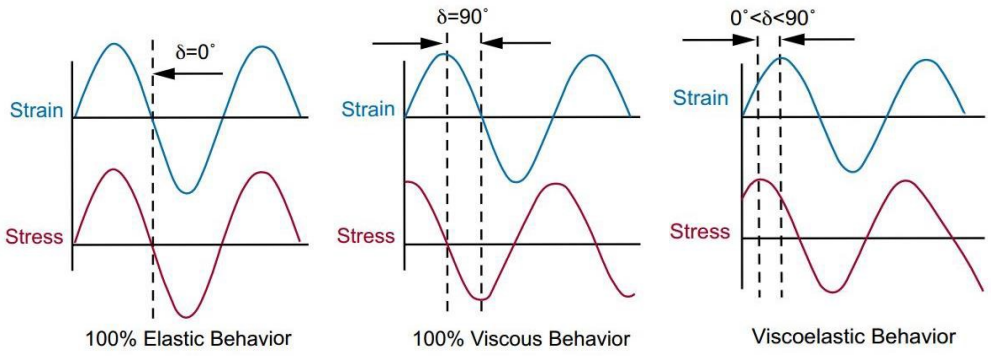

Figure 2. 8: *Stress-strain curves in oscillatory regime. The first represents the elastic behavior in which stress and strain are in phase. The second represents the viscous behavior for which stress and strain are out of phase of 90°. The last one represents the viscoelastic behavior in which stress and strain are out of phase by an angle between 0 and 90°.*[9]

Rewriting equation (2.18), it is possible to separate the elastic and the viscous contributions:

$$\sigma(t) = \sigma_0[sin(\omega t) \, cos \, \delta + cos(\omega t) \, sin \, \delta] \tag{2. 19}$$

It is also possible to define a storage modulus G', related to the stored elastic deformation energy:

$$G'(\omega) = \frac{\sigma_0}{\gamma_0} cos \, \delta \tag{2. 20}$$

and a loss modulus G'', related to the deformation energy lost because dissipated through internal friction when flow occurs:

$$G''(\omega) = \frac{\sigma_0}{\gamma_0} sin \, \delta \tag{2. 21}$$

The loss factor is defined as the ratio between the two moduli:

$$tan\,\delta = \frac{G''}{G'} \tag{2. 22}$$

When the loss factor is lower than 1 the elastic contribution prevails, while if it is greater than 1 the viscous one prevails. By substituting $\sin(\omega t)$ with $e^{i\omega t}$ and $\cos(\omega t)$ with $ie^{i\omega t}$ it is possible to express the strain and strain rate in exponential form as follows:

$$\gamma(t) = \gamma_0 e^{i\omega t} \tag{2. 23}$$

$$\dot{\gamma}(t) = i\omega\gamma_0 e^{i\omega t} \tag{2. 24}$$

and it is possible to obtain the following expression for the stress:

$$\sigma(t) = \sigma_0\left[e^{i\omega t}\,cos\,\delta + ie^{i\omega t}\,sin\,\delta\right] \tag{2. 25}$$

A complex modulus G* can also be defined as:

$$G^*(\omega) = \frac{\sigma(t)}{\gamma(t)} = G[cos\,\delta + i\,sin\,\delta] = G'(\omega) + iG''(\omega) \tag{2. 26}$$

The modulus of G^* is equal to the ratio between the stress and the strain, as expressed in equation (2.27), and equation (2.28) expresses the relationship between the complex modulus and the zero-shear viscosity.

$$|G^*(\omega)| = \sqrt{(G')^2 + (G'')^2} = \frac{\sigma_0}{\gamma_0} \tag{2. 27}$$

$$\lim_{\omega\to 0}\frac{|G^*(\omega)|}{\omega} = \eta_0 \tag{2. 28}$$

The ratio between the stress (2.25) and the strain rate (2.24) defines the complex viscosity:

$$\eta^*(\omega) = \frac{\sigma(t)}{\dot{\gamma}(t)} = \frac{G^*(\omega)}{i\omega} = \eta' - i\eta'' \tag{2. 29}$$

Figure 2.9 shows the geometrical approach in the complex plane.

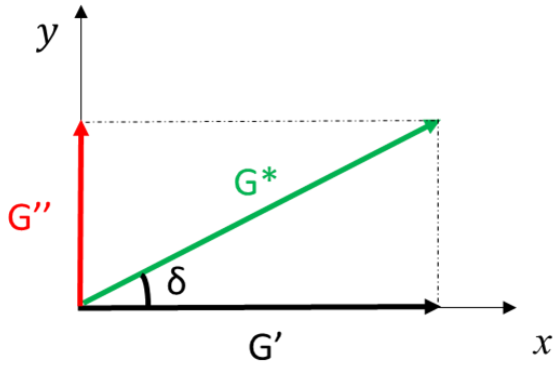

Figure 2. 9: *Graphical approach in the complex plane. G' is the storage modulus, G'' is the loss modulus, G* is the complex modulus and tanδ is the loss factor.*

Since the strain rate is proportional to the angular frequency, the complex viscosity, which is a function of ω, has the same expression of the shear viscosity. Equation (2.30) is the Cox-Merz's law:

$$|\eta^*(\omega)|_{\omega=\dot{\gamma}} = \eta(\dot{\gamma}) \tag{2. 30}$$

The Maxwell model in oscillatory regime is described by the following expressions:

$$G' = \frac{G\omega^2\tau^2}{1+\omega^2\tau^2} \tag{2. 31}$$

$$G'' = \frac{G\omega\tau}{1+\omega^2\tau^2} \tag{2. 32}$$

$$tan\,\delta = \frac{1}{\omega\tau} \tag{2. 33}$$

G', G'' and $tan\delta$ are function of ω and τ. Figure 2.10 shows an example of frequency sweep test. The curves are the loss modulus and the storage modulus, reported as function of the angular frequency. A cross-over point can be noticed. Here the two moduli are equal and consequently $tan\,\delta$=1.

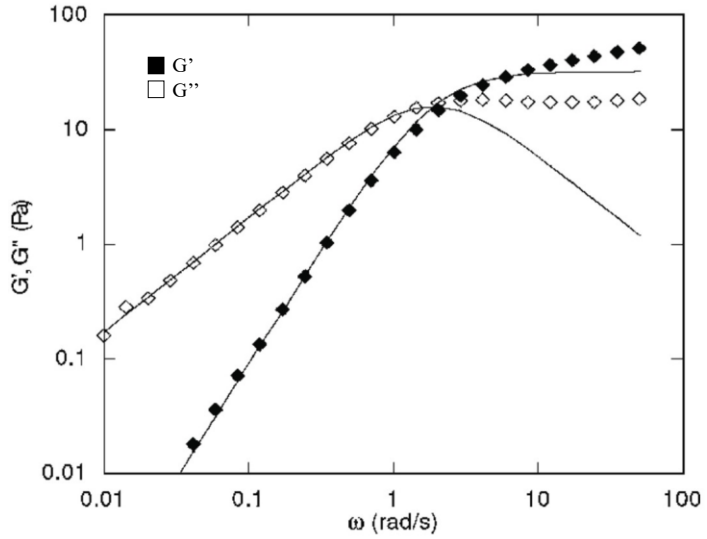

Figure 2. 10: *Example of frequency sweep test. The curves graph the storage modulus G' and the loss modulus G'', as function of the angular frequency. There is a point in which the two moduli are equal, called cross-over point. When G' is higher than G'' prevails the elastic behavior.*

DMA analysis can be performed in different ways by varying the angular frequency and the time: isochronous temperature scanning (ω fixed, τ variable), isothermal frequency scanning (ωvariable, τ fixed) or isochronous and isothermal time scanning (ω fixed, τ fixed).

2.3.2.1 Time-temperature superposition principle (TTS)

The viscoelastic behavior has a strong dependency on the stress frequency. Thanks to the correlation between time and temperature, it is possibile to extend the classic frequency range of measures (about four decades) to more than twenty decades. The basic idea is that the molecular relaxation or rearrangements in viscoelastic materials occur with higher rates at higher temperatures and then there is a direct equivalence between time (frequency) and temperature. In this way, it is possibile to reduce the time needed for the measure by conducting the experiment at elevated temperatures. The DMA isothermal curves, measured at different frequencies, are correlated with a reference temperature to create the so-called "master curve". This allows to describe the complete relaxation behavior of viscoelastic materials. The amount of shifting in the horizontal direction of

the data is generally described using the William-Landel-Ferry equation. This describes a shift factor a_T, as function of temperature as follows:

$$log\ a_T = \frac{-C_1(T - T_0)}{C_2 + (T - T_0)} \tag{2. 34}$$

where C_1 and C_2 are two constants, T_0 the reference temperature and T the measurement temperature, both expressed in Kelvin. The WLF equation is typically used to describe the time-temperature behavior of polymers in the glass transition zone or in the melt. Another model generally used to describe the behavior outside the glass transition zone for some melts is the Arrhenius equation:

$$log\ a_T = \frac{E}{R(T - T_0)} \tag{2. 35}$$

Where E is an activation energy associated to the energy barrier involved in the relaxation process, R is the gas constant, T is the measurement temperature and T_0 the reference temperature, both expressed in Kelvin. Figure 2.11 shows a typical trend for the shift factors and Figure 2.12 a typical master curve.

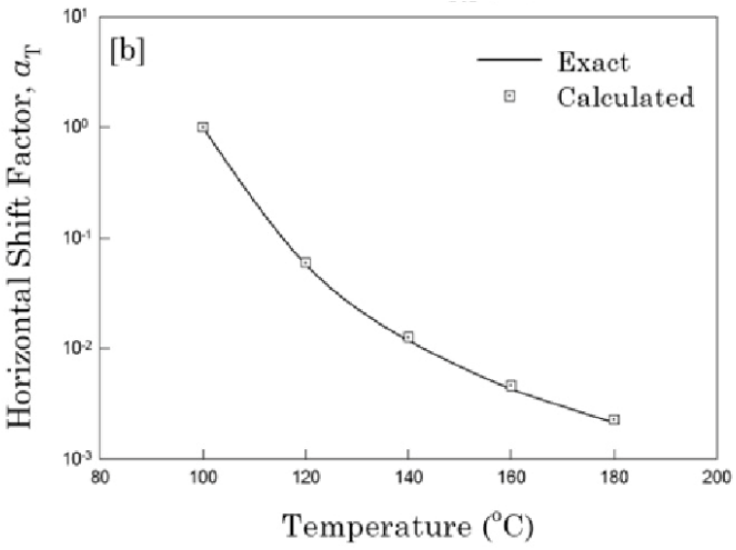

Figure 2. 11: *Shift factors. In the y-axis are represented the horizontal shift factors and on the x-axis the measurement temperatures.*[10]

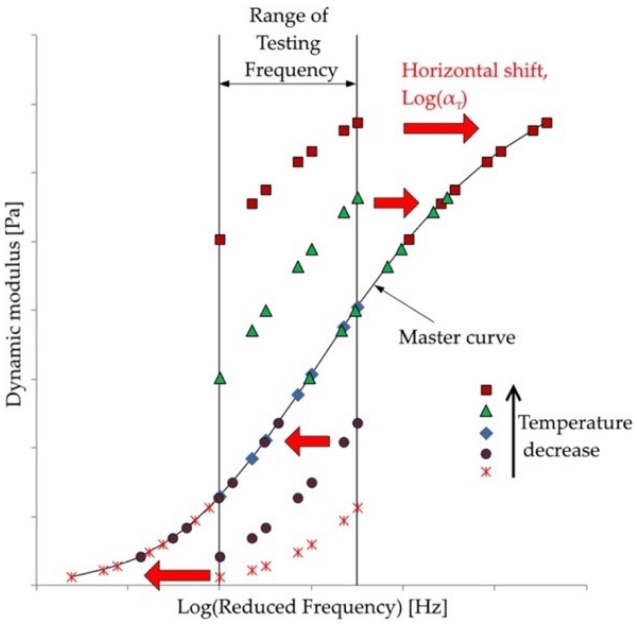

Figure 2. 12: *Master curve example. The experimental data are obtained in the range of testing frequencies by varying temperature, then with the determination of shift factors, the points are translated along the reduced frequency axis. High temperatures correspond to low frequencies.*[11]

The x-axis is represented by the reduced frequency obtained by the following equation:

$$\omega_{red}(T_0) = a_T \cdot \omega(T) \tag{2. 36}$$

It can be seen that the master curve is obtained with the translation of the experimental data, obtained at several temperatures in the frequency testing range, along the frequency axis. In some complex cases, connected with the not-negligible density variation with temperature, it is necessary to also apply a vertical translation, by a vertical shift factor defined as:

$$b_T = \frac{T_0 \cdot \rho_0}{T \cdot \rho} \tag{2. 37}$$

3 Rheology of filled suspensions

Since ABS is a two-phase material, it is important to understand how and why the dispersed phase can affect the properties of the system, for example the viscosity. There are many parameters governing the viscosity of filled systems, some of these are summarized in the follow list:

- the volume fraction of dispersed particles
- particles dimensions and distribution
- interaction between particles and the fluid
- deformability of the particles

The last parameter is the most important for the samples at study because they are significantly different in terms of particles deformability. In literature there are some models predicting the suspension viscosity of Newtonian fluids, depending on particle elasticity and on the fraction of dispersed phase. However, first the case of rigid spherical particles will be introduced and then the case of deformable particles.

3.1 Rigid spherical particles

The viscosity of a dilute suspension of rigid spheres in a Newtonian fluid can be expressed by the Einstein's equation [7]:

$$\eta_{suspension} = \eta_{fluid}(1 + 2.5\varphi) \tag{3. 1}$$

Where η_{fluid} is the viscosity of the suspending fluid and φ is the volume fraction of dispersed particles. Equation (3.1) is valid only for dilute systems in which there are no interparticle interactions. The relative viscosity of a semi-dilute suspension is expressed by the Batchelor relationship:

$$\eta_{rel} = \frac{\eta_{susp}}{\eta_{fluid}} = 1 + B\varphi + C\varphi^2 \tag{3. 2}$$

with B=2.5 and C=7.6. It is possible to see that the relative viscosity of a semi-dilute suspension is greater than that predicted by Einstein and does not depend on the particle size. A useful model for higher volume fractions is the Maron-Pierce equation (3.3) which describes the viscosity of a concentrate system defining a maximum packing fraction φ_m, a vertical asymptote for an infinite viscosity value:

$$\eta_{rel} = \frac{1}{\left(1 - \frac{\varphi}{\varphi_m}\right)^2} \tag{3. 3}$$

As a result, in the case of big and well-dispersed spheres, the relative viscosity depends only on the volume fraction φ.

3.2 Non-rigid dispersed phase

In the case of dilute suspensions in which both the suspended phase and the suspending fluid are Newtonian, the shear viscosity of the system is governed by the Taylor equation:

$$\eta_{susp} = \eta_{fluid}\left(1 + \frac{5k+2}{2k+2}\varphi\right) \tag{3. 4}$$

where k is the ratio between the viscosity of the dispersed phase and the viscosity of the matrix. In this way, the higher the k value, the higher the viscosity of the suspension. This means that particles with lower viscosity led to a lower suspension viscosity. Equation (3.4) provides two limiting cases: when particles have an infinite value of viscosity (rigid particles) the viscosity of the suspension approaches the one predicted by Einstein (3.1), but when the viscosity of the dispersed phase is near zero, for example in case of gases, k tends to zero and the viscosity of the system is given by:

$$\eta_{susp} = \eta_{fluid}(1 + \varphi) \tag{3. 5}$$

However, in the case of elastic particles it is more convenient and appropriate to consider the elastic modulus rather than their viscosity. For this reason, a different dimensionless

parameter, governing the flow behavior of elastic particles, will be introduced in the next paragraph.

3.3 Elastic spherical particles

The elastic capillary number Ca_e of a suspension of deformable particles is given by the ratio between the fluid viscous stresses and the elastic modulus of the particles.[12] It is easy to understand that Ca_e is higher when a higher stress is applied and lower for higher elastic modulus of the particles. In literature there are some models able to describe the mechanical behavior of deformable particles. The first is the Hookean model, which describes the linear elastic behavior, already mentioned in §2.1. The second is the neo-Hookean, which is a hyper-elastic model, like the Hooke's one at small deformations, but at high deformation it predicts a non-linear relation between stress and strain. The last is the hyper-elastic model introduced by Gent, which, by considering a parameter J_m known as "strain-locking parameter", includes the material stiffening at large deformations. Based on these models, and after a brief introduction on suspensions rheology, the different behavior of elastic particles in Newtonian fluids will be discussed, starting from the case of a single spherical particle, passing through dilute suspensions, and ending with the non-diluted case. Both the elongational flow and the shear flow for each case will be taken into account.

3.3.1 Single spherical particle

In 1967 Roscoe studied the deformation of a linear elastic particle suspended in a Newtonian fluid undergoing uniaxial extensional flow. Defining the deformation parameter as $D = (L - B)/(L + B)$, with L and B the semiaxis of an ellipse, this can be quantified as:

$$D = \frac{15}{8} Ca_e \tag{3. 6}$$

With $Ca_e = \eta\, \dot{\varepsilon}/G$. So, the higher the elastic modulus of the particle, the lower the capillary number and consequently the particle deformation.

Roscoe also considered the shear flow, finding that, for small Ca_e, the deformation parameter is:

$$D = \frac{5}{4} Ca_e \tag{3. 7}$$

Equations (3.6) and (3.7) are similar but, for the same Ca_e, the deformation of particle subjected to elongation is more pronounced compared to a sheared one as shown in Figure 3.1.

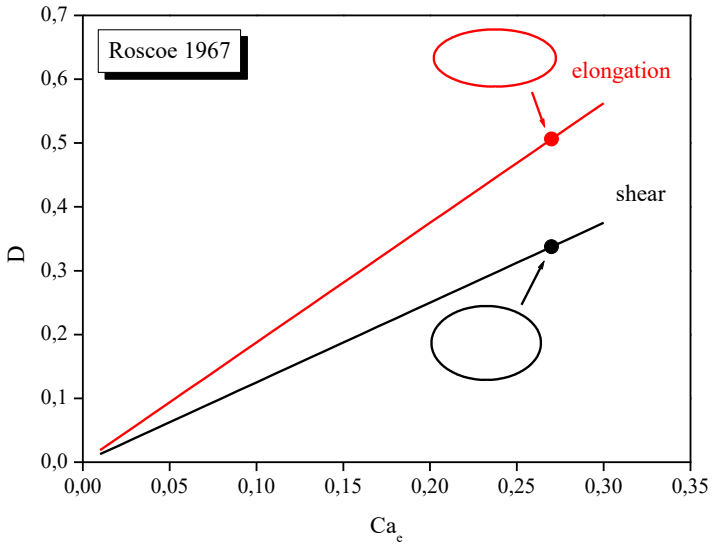

Figure 3. 1: *Particle deformation as function of elastic capillary number Ca_e. In case of simple elongation, the particle deforms more than in case of shear flow.*

3.3.2 Dilute suspensions

For a dilute suspension it is possible to assume well separated particles and no interparticle interactions. In 1967, Roscoe derived the expression (3.8) for the elongational viscosity of a suspension of linear elastic spheres in a Newtonian liquid undergoing uniaxial extensional flow:

$$\frac{\eta_{e,s}}{3\eta} = 1 + \frac{5}{2}\varphi + \frac{75}{28} Ca_e \varphi \tag{3. 8}$$

Where $\eta_{e,s}$ is the suspension extensional viscosity and 3η is the extensional viscosity of the pure suspending fluid. The first term, called “excess extensional viscosity”, is similar

to the strain hardening index, which represents the deviation of elongational viscosity of the system from the elongational viscosity of the system measured in the linear regime, which is three-times the shear viscosity as expressed by the Trouton rule reported in equation (2.5). The difference is that equation (3.8) defines only the contribution of the presence of deformable particles, because the contribution of the matrix is "cancelled" by dividing the extensional viscosity of the system by the viscosity of the matrix.

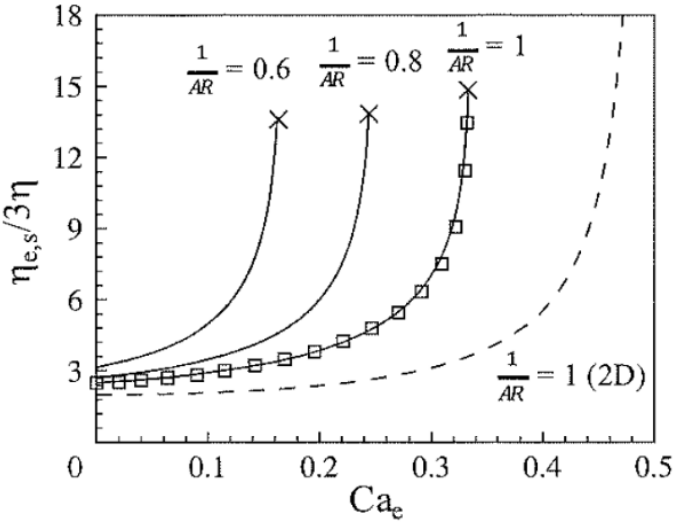

Figure 3. 2: *Excess of extensional viscosity of a dilute suspension of initially spherical particles. Increasing Ca_e (softer particles) the excess of extensional viscosity is higher. Furthermore, as the particle approaches an ellipsoidal shape (aspect ratio AR>1), the $\eta_{e,s}/3\eta$ increases faster than for AR=1.*[12]

As can be seen in Figure 3.2, an increase in Ca_e, by increasing the stress or decreasing the elastic modulus (softer particles) results in an increase of the strain hardening, with a significant increase in viscosity. Furthermore, as the aspect ratio grows, the excess of viscosity become larger, and the strain hardening occurs for lower Ca_e. Moving to the shear flow case, in 1967, Roscoe, Goddard and Miller obtained equation (3.9) by performing perturbative analysis. This expresses the ratio between the viscosity of a suspension of monodispersed elastic spheres and the viscosity of the Newtonian suspending fluid, undergoing simple shear flow.

$$\frac{\eta_s}{\eta} = 1 + \frac{5}{2}\varphi\left(1 - \frac{\frac{15}{4}Ca_e^2}{1 + \frac{9}{4}Ca_e^2}\right) \tag{3. 9}$$

Even though equations (3.8) and (3.9) refer to dilute suspensions, extending them to the present case (pseudoplastic matrix and non-dilute system) it is possible to obtain the trends reported in Figure 3.3. This is reported to give just an idea of the contrasting contribution to the viscosity of a suspension of deformable particles by the two kinds of flow, elongational vs. shear flow, for a constant value of $\varphi = 0.2$.

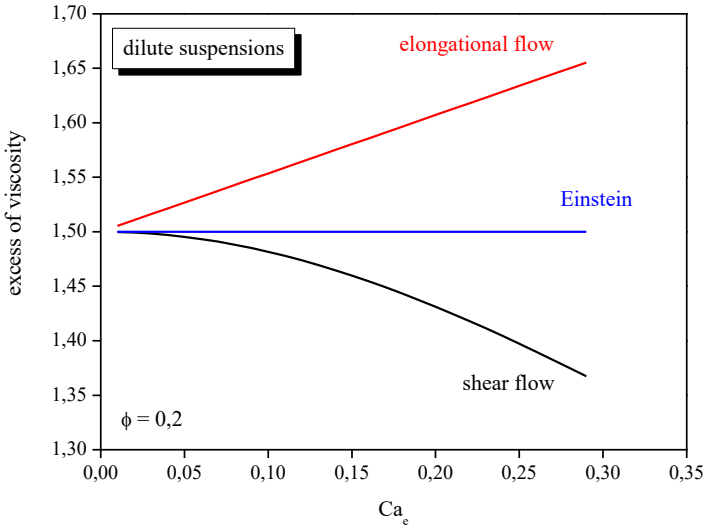

Figure 3. 3: *Approximation of excess of viscosity for non-dilute suspensions in Newtonian fluids. It has been used expressions valid for dilute suspension considering a phase-volume fraction of dispersed phase equal to 0.2. it is possible to see the different contribution of Ca_e in shear flow and in elongational flow.*

Although with a large approximation it is possible to say that, in case of elongational flow, softer particles lead to the strain hardening phenomenon, which is an upward deviation from the Einstein case (no capillary number contribution) and shear thinning in case of shear flow. The suspension average intrinsic viscosity (dimensionless) is defined as:

$$[\bar{\eta}] = \frac{\frac{\eta_s}{\eta} - 1}{\varphi} \tag{3. 10}$$

The Figure 3.4 shows $[\bar{\eta}]$ as a function of Ca_e, parametric in the aspect ratio AR.

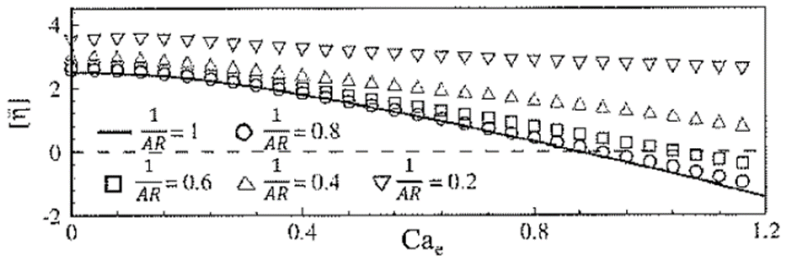

Fig. 14 The intrinsic viscosity $[\bar{\eta}]$ of a dilute suspension of initially prolate spheroidal neo-Hookean particles as funcion of Ca_e for several values of AR. Adapted with permission from Gao et al. (2012). Copyright American Physical Society 2012

Figure 3. 4: *Dimensionless intrinsic viscosity* $[\bar{\eta}]$ *of a dilute suspension of an elastic particle as function of* Ca_e *for several values of AR. It decreases by increasing the elastic capillary number and decreases more when particles approach the spherical shape.*[12]

By increasing the capillary number, the suspension intrinsic viscosity decreases. Furthermore, fixing Ca_e, $[\bar{\eta}]$ is higher for more elongated particles (higher AR).

3.3.3 Non dilute suspension

In 2015, Avazmohammadi and Castaneda modelled, through numerical simulations, the rheological behavior of initially spherical neo-Hookean elastic particles in a Newtonian liquid. In case of elongational flow, as shown in Figure 3.5, the excess of viscosity increases by increasing Ca_e and φ, as in the semi-dilute case. The major difference between the two models is that for neo-Hookean particles, Figure 3.5 a) and c), the excess viscosity reaches a maximum critical value with no viscosity finite value, while for the Gent's model, Figure 3.5 b) and d), the presence of the strain-locking parameter allows to suppress this problem. In fact, when $J_{m\to\infty}$ the Gent's model approaches the neo-Hookean one, while for finite values of J_m it provides the suspension viscosity. Furthermore, by increasing the volume fraction of dispersed phase, increases the suspension viscosity, as in case of dilute suspension. Then, the simulations provided the same viscosity trend of semi-dilute suspensions, but in this case the contribution of the volume fraction is taken into account.

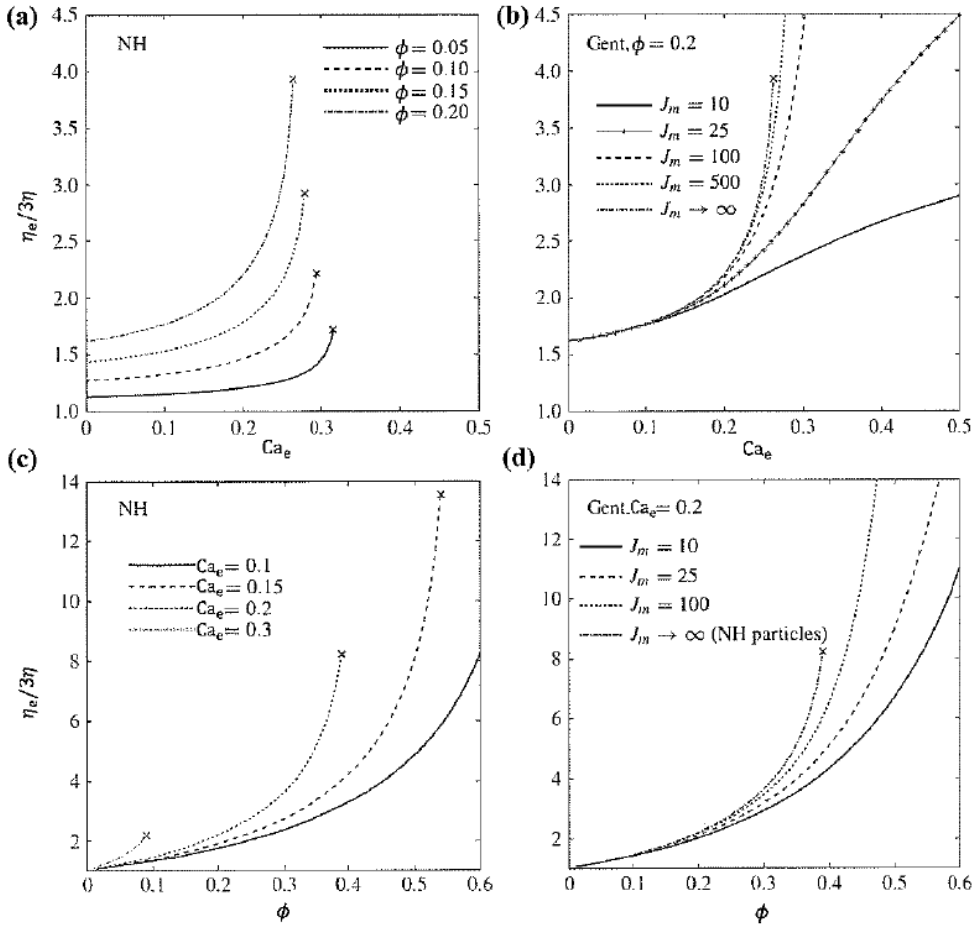

Fig. 13 Results for the steady-state relative viscosity of suspensions of initially spherical neo-Hookean and Gent particles in extensional flow. Adapted with permission from Avazmohammadi and Castañeda (2015). Copyright Cambridge University Press 2015

Figure 3. 5: *Excess of extensional viscosity of suspension of initially spherical neo-Hookean and Gent particles. Graphs a) and C) show the excess of viscosity for neo-Hookean particles, graphs b) and d) show Gent particles.*[12]

Figure 3.6 shows the suspension normalized shear viscosity as function of φ, for neo-Hookean and Gent particles. It is possible to see that varying the value of Ca_e the trend of the relative viscosity changes a lot, showing a Ca_e value for which the suspension viscosity equals the viscosity of the suspending fluid, independently on φ. In the case of the Gent model, Figure 3.6 b), curves are parametric in J_m for $Ca_e = 0.2$, but the trend is more or less the same.

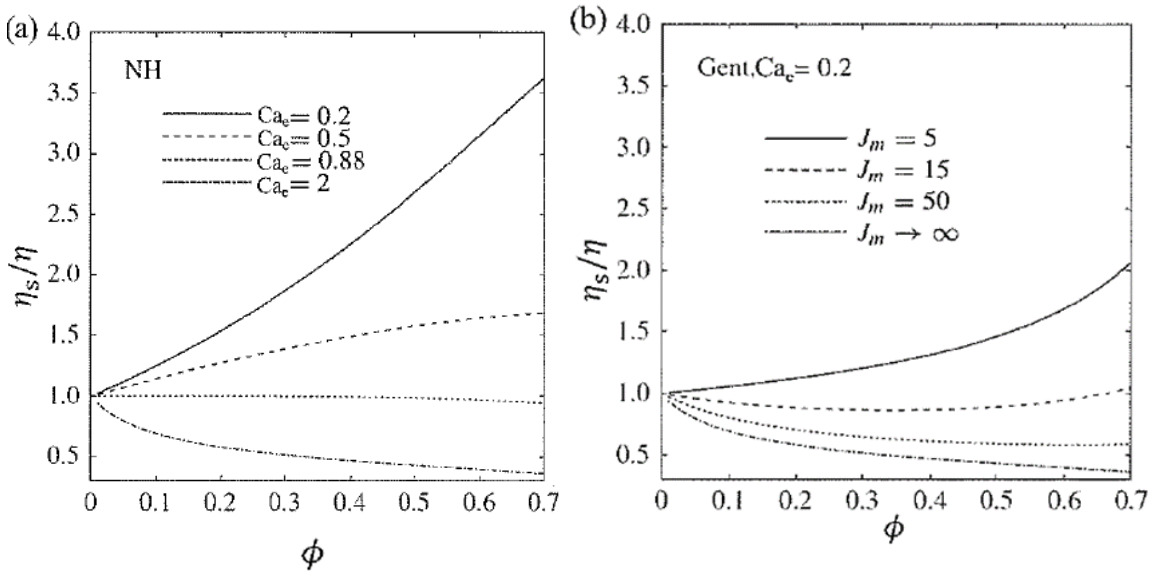

Figure 3. 6: *Excess of viscosity in shear flow for neo-Hookean and Gent particles. Exists a value of Ca_e, about 0.88, for which the viscosity of the suspension is like that of the matrix and for lower values the suspension has a lower viscosity and for higher values a higher viscosity.*[12]

So, for the non-dilute case the decrease of suspension shear viscosity occurs only for high values of Ca_e, then with high particles deformability. For more rigid particles an increase in shear viscosity is even found.

3.4 Migration of deformable particles

In 2016, Villone *et al*. performed numerical simulations of the lateral migration in tube flow of deformable particles, in Newtonian and viscoelastic media.[13] They studied the deformation and the cross-streamline migration of an elastic particle in pressure-driven flow in a cylindrical tube through 3D finite element method numerical simulations. The principal parameters considered were:

- the blockage ratio β, defined as the ratio between the diameter of the particle and the diameter of the channel;
- the elastic capillary number Ca_e;
- the Deborah number *De.*

Studying the case of a neo-Hookean elastic particles suspended in a Newtonian fluid, they found that independently on the initial position of the particle in the channel, this always moves toward the axis of the tube, with greater velocity for greater distances from the centre.

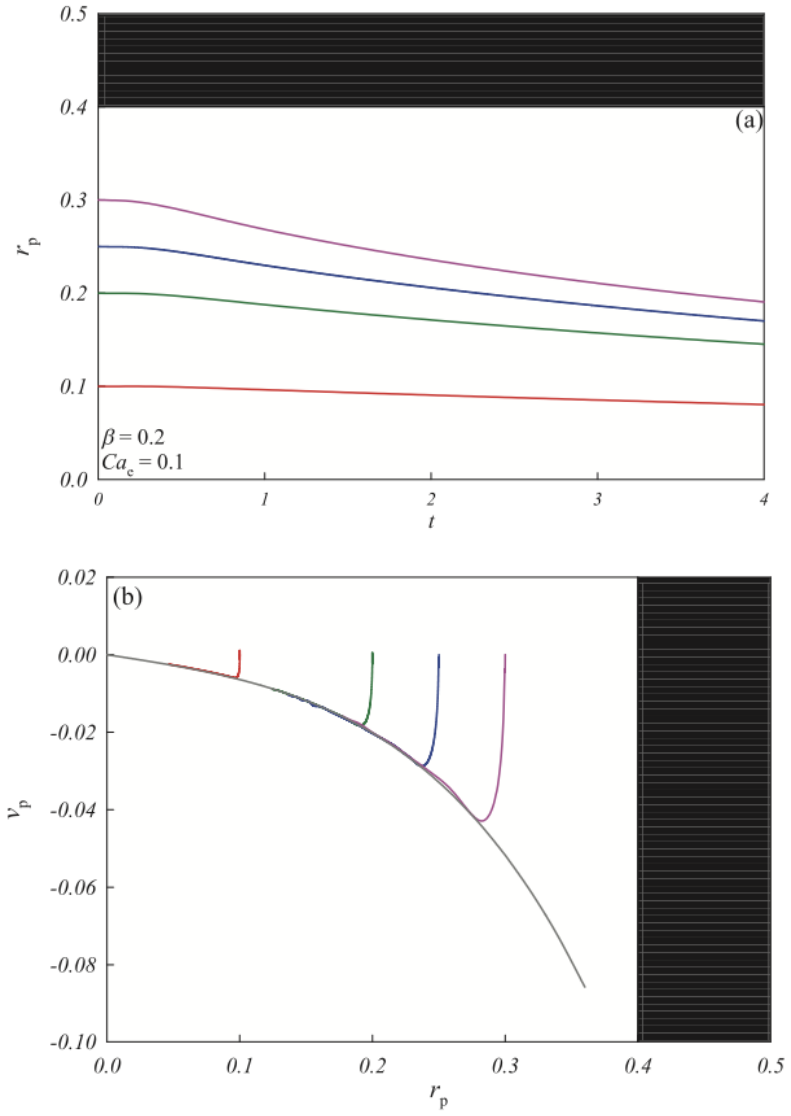

Figure 3. 7: *a) Trajectories as function of initial position of a neo-Hookean particle in a Newtonian fluid under pressure-driven tube flow. b) Migration velocity v_p of the particle as function of its radial position r_p. The negative sign represents the migration toward the tube axis.*[13]

Figure 3.7 a) shows the various trajectories of the particles based on their initial radial position, while Figure 3.7 b) shows on the y-axis the particles migration velocity v_p and

on x-axis the radial position r_p of the particle centre. The negative sign of velocity represents a migration toward the tube axis. The black zone represents the physically not accessible zone by the centre of volume of the particle, signed with $r_{p,max}$. Figure 3.8 shows, by varying β or Ca_e, the variation of the velocity profile. By increasing the elastic capillary number or the blockage ratio, particles migrate faster toward the tube axis.

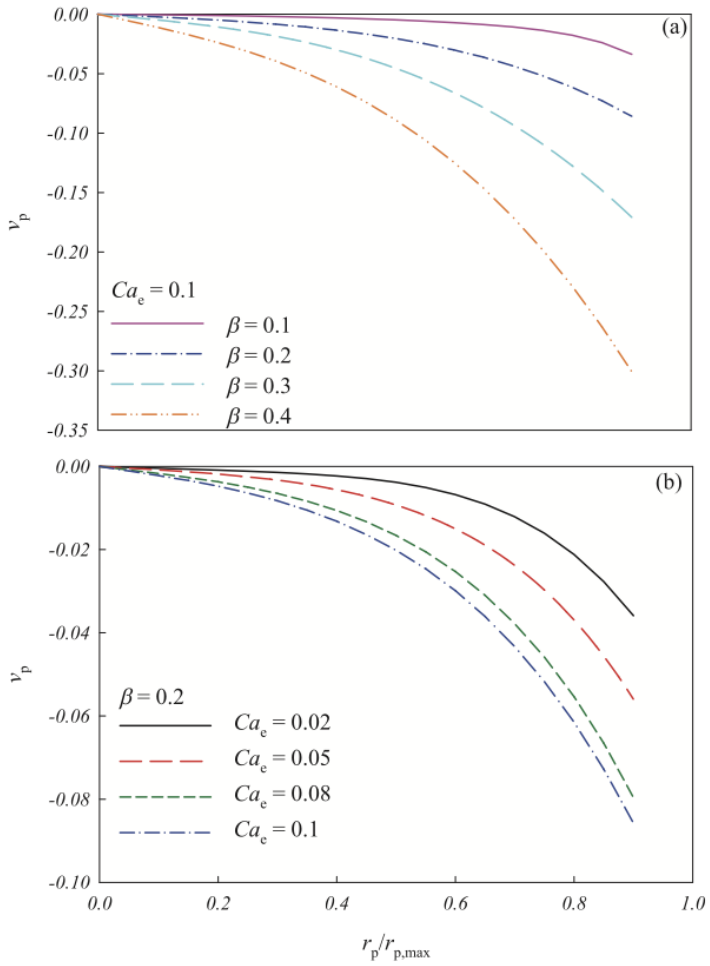

Figure 3. 8: *Effect of the blockage ratio β and of the elastic capillary number Ca_e on the migration velocity of a neo-Hookean particle suspended in a Newtonian fluid under pressure driven tube flow. The x-axis represents the normalized radial position.*[13]

Considering as suspending fluid a viscoelastic liquid (Olroyd-B) they found that the velocity profile changed, showing a maximum between the centre and $r_{p,max}$. So, both the axis and the wall are equilibrium positions, resulting as particle attractor and as particle

repulsor, respectively. Figure 3.9 shows that decreasing Ca_e or increasing the Deborah number slower the migration toward the axis of the tube.

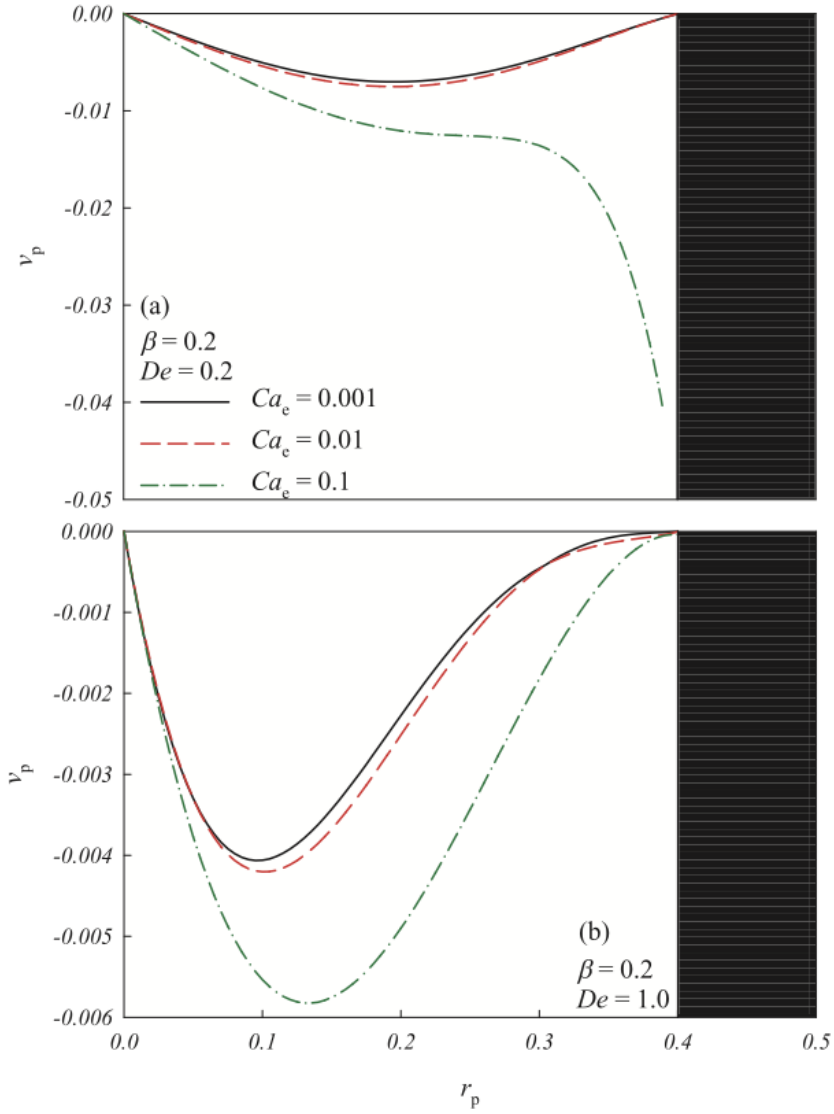

Figure 3. 9: *Migration velocity v_p of a neo-Hookean particle, suspended in a Olroyd-B fluid, as function of its radial position r_p for De=0.2 (a) and De=1 (b). By increasing De the migration toward the tube axis is slower.*[13]

Furthermore, in Figure 3.10, reported for *De*=5, an area appears where the particles do migrate to the wall. Then, the tube axis is not the only particle attractor. In fact, based on the initial radial position, a particle can move toward the wall or the axis, and the neutral height r_N defines an unstable equilibrium position. By decreasing Ca_e, the equilibrium

position moves to the centre and the area involved in particle migration towards the wall increases.

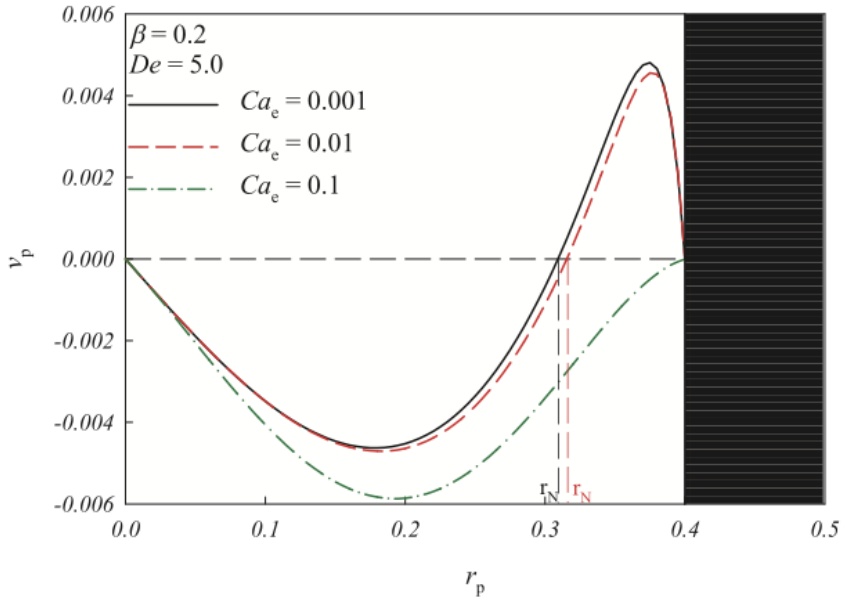

Figure 3. 10: *Migration velocity v_p of a neo-Hookean particle, suspended in a Olroyd-B fluid, as function of its radial position r_p. It appears a zone, defined by an instable equilibrium position r_N, in which particles migrates toward the wall. For stiffer particles (lower Ca_e) the area involved in lateral migration toward the wall is greater.*[13]

Finally, considering as suspending media a shear-thinning fluid (Giesekus liquid), they found that particles have less tendency to move towards the centre. Figure 3.11 shows that by increasing the elastic capillary number or increasing De, the r_N shifts towards the tube axis, then the area involved in the lateral migration toward the wall is greater.

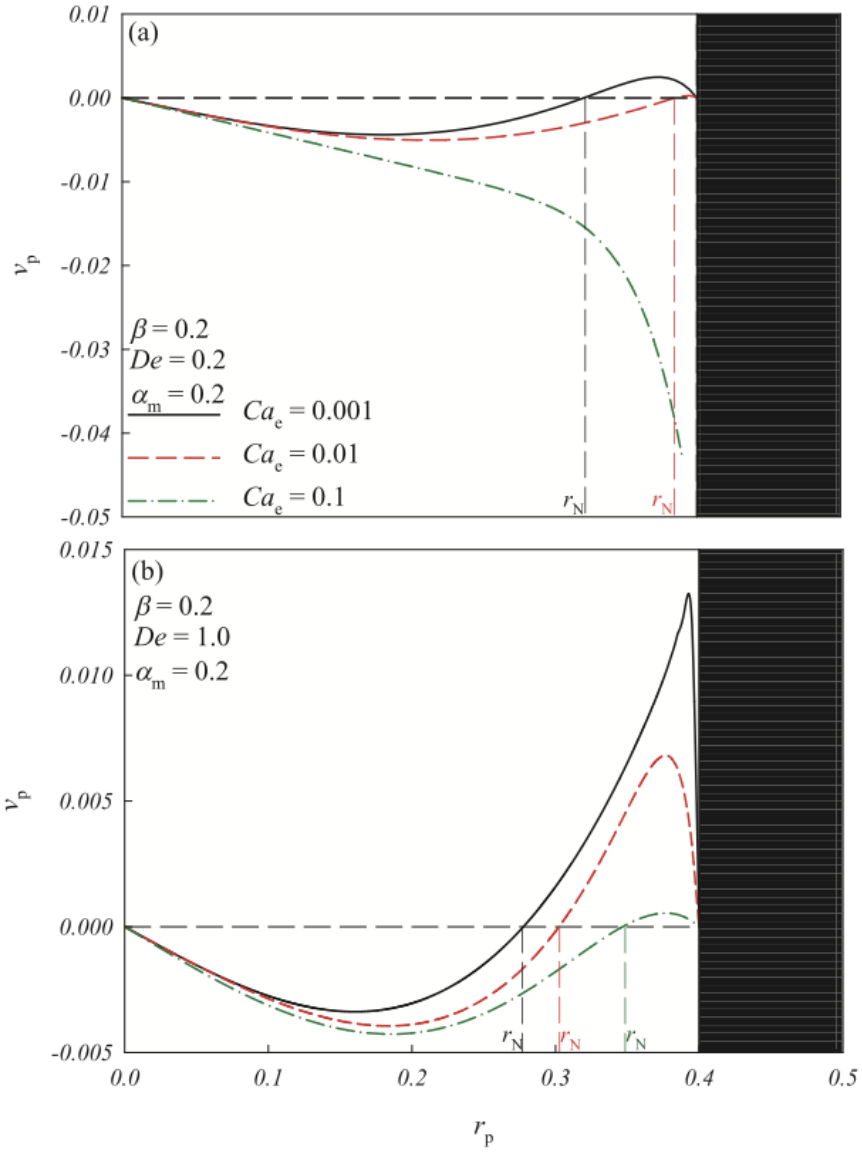

Figure 3. 11: *Migration velocity v_p of a neo-Hookean particle suspended in a Gsk fluid, as function of its radial position r_p. There is a zone, defined by the instable equilibrium position r_N, in which particles migrates toward the wall. This area becomes greater by decreasing Ca_e or by increasing De. The migration toward the centre of the tube is slower for particles suspended in shear-thinning fluids.*[13]

This brief introduction to the theory of lateral migration of deformable particles in pressure-driven tube flow is mentioned because it will be taken up again later to try to explain an unexpected result, for which particles migration toward the surface can be an explanation.

4 Injection Molding

Injection molding was born in the second half of the 1980s, when John Wesley Hyatt and his brother created the first machine that by the injection of molten plastic into a mold, through the action of a piston, allowed the production of small everyday objects, such as combs and buttons. However, it was only after World War II that mass production of injection-molded objects took off and James Hendry created the first screw-injection molding machine, which rapidly became popular due to the better control and precision [14]. Today, injection molding is one of the most important processes to produce plastic articles, thanks to the possibility of producing large as well as small objects, but especially with complicated geometries, maintaining a good productivity. In Figure 4.1 a general scheme of an injection-molding machine is reported. Basically, it is composed by an injection unit, which has the task of melting the solid material and, through the action of a screw, bringing the melt to the injection nozzle, and of a clamping unit in which the object is formed in the desired shape.

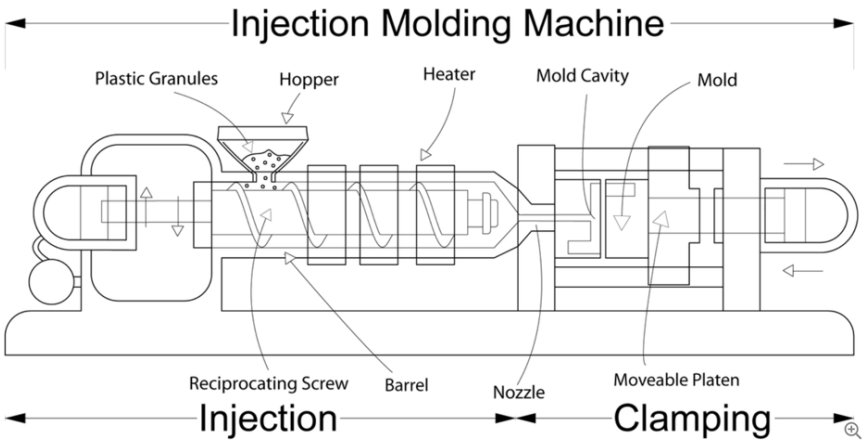

Figure 4. 1: *Scheme of an injection-molding machine*.[15]

4.1 The filling stage

During the injection molding, polymer granules are melted in the screw, thanks to the heating system, and forced through an orifice (gate).[16] The melt is injected into a closed cold mold cavity, where it solidifies under pressure in the desired shape. Injection molding involves two distinct processes. The first comprises the elementary steps of solid transport, melt generation, mixing and the flow pressurizing before the injection unit. The second comprises the product shaping and structuring, which takes place in the mold cavity. The time needed to complete the injection molding cycle is largely related to the time required for cooling, while the filling time takes up only a small part. Figure 4.2 schematically shows the injection molding cycle. First the heating system and the rotation of the screw allow the melting and the mixing of the polymer pellets as well as the advancement of the melt at the head of the screw, creating the dosing volume. At this point, the screw, acting like a piston with a determined velocity, injects the melt into the mold cavity. When the mold is almost filled, the switch-over point occurs, and the screw moves to maintain the pressure avoiding back flows.

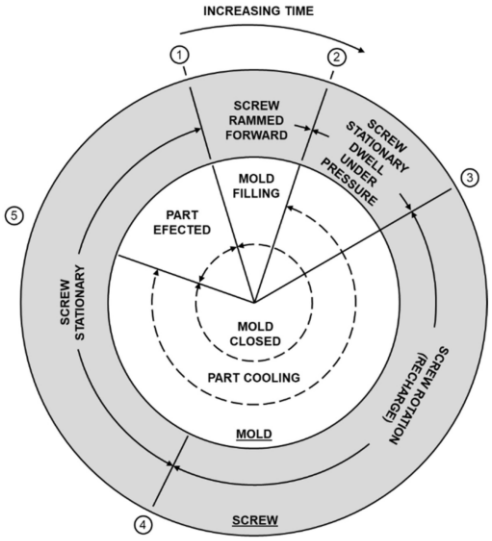

Figure 4. 2: *Injection molding cycle.*[16]

The mold is kept at constant temperature below T_g (for amorphous polymers) or T_m (for semi-crystalline polymers). The gate controls the flow of the polymer into the mold. After

the cavity has been filled, the packing pressure is applied to introduce a small amount of additional melt into the cavity to compensate the thermal contraction of the polymer during the cooling stage. When the polymer has been completely solidified, the mold is opened, and the item is removed. Since the solidification time can be comparable to the polymer relaxation time (De≃1), molded articles solidify under strained conditions, so they contain frozen-in strains and stresses. Figure 4.3 shows the moldability area in a graph of temperature versus pressure. Below the bottom curve the polymer is solid or too much viscous to flow, while above the top curve the polymer thermally degrades. The left curve represents the short shot because the pressure is not enough to fill completely the cavity and the right curve represents the formation of flash, due to a too high polymer flowability or too high applied pressure.

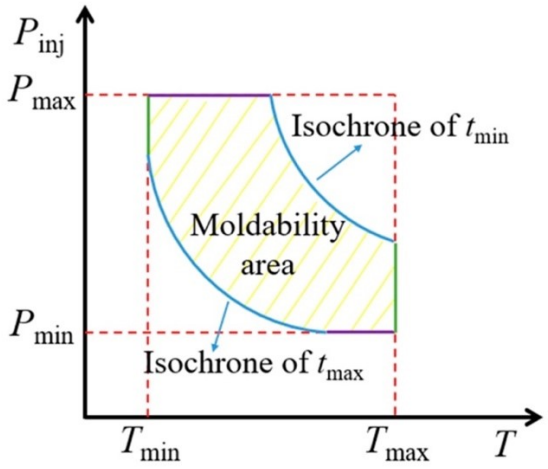

Figure 4. 3: *Moldability area. There is a pressure and temperature range defining the process parameters.*[17]

During the early stages of filling, the flow front near the gate is circular but, as the melt advances away from it, the flow front becomes flat (for an isothermal filling) as shown in Figure 4.4. In the front region, the melt at the centre of thickness direction, which moves with the maximum velocity of the parabolic-like velocity profile, spills out or fountains out, to the mold wall, forming the surface of the molded object. The melt decelerates from the maximum velocity to the mean velocity at which the front advances and as it decelerates in flow direction, it acquires a velocity component in the thickness one.

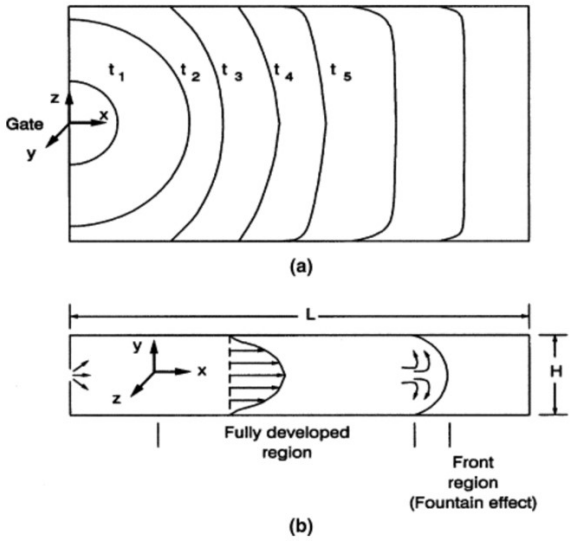

Figure 4. 4: *Flow front during the filling of the mold. a) In the region near the gate the flow front is circular but as the melt advance the flow front becomes flat. b) Thickness direction: in the fully developed region the maximum velocity profile is parabolic and when the melt approaches the front region it spills out towards the wall (fountain flow effect).*[16]

Injection molding, as well as other processes, such as extrusion, causes a high anisotropy in products, because the preferential orientation of macromolecules along the flow direction. As will be explained in §4.2, two causes of molecular orientation occur during the injection molding process: the shear flow and the elongational flow due to the presence of the fountain flow effect.

4.2 Molecular orientation in injection molding

The complex state of orientation induced by the injection-molded process can be investigated through two experimental techniques: birefringence and shrinkage at high temperature of microtomed sample cut from the product.[18] Menges and Wubken studied the orientation of amorphous polystyrene by measuring the shrinkage of microtomed samples, heated above the glass transition temperature.[19] Figure 4.5 shows the trend of shrinkage at different distances from the surface. The basic hypothesis is that shrinkage is connected to the molecular orientation, which is related to the flow during the filling stage. In the direction of flow, shrinkage assumes the maximum value at the surface and decreases approaching the centre, passing through a secondary maximum. In the crossflow

direction the shrinkage trend is similar but there is no secondary maximum between the surface and the centre.

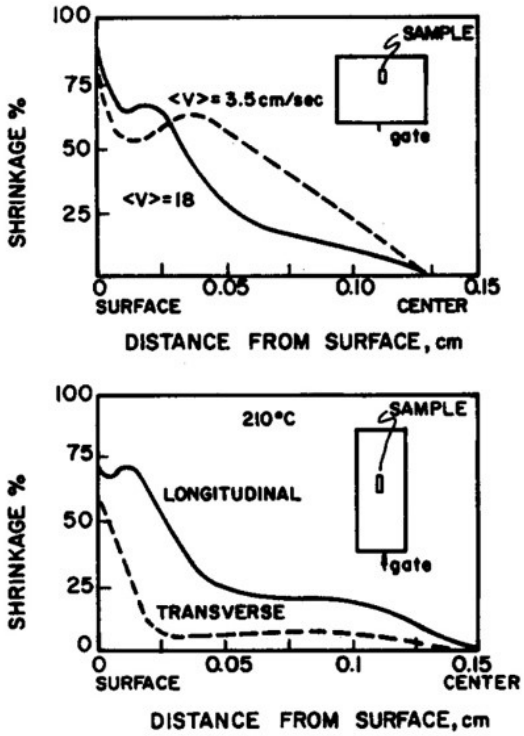

Fig. 1. Shrinkage distribution of injection-molded amorphous polystyrene, measured by Menges and Wubken.[6]

Figure 4. 5: *Shrinkage distribution of injection-molded amorphous polystyrene, measured on microtomed samples heated above the glass-transition temperature.*[19]

The process parameters influence the orientation. In fact, by increasing the melt temperature and reducing the injection speed, shrinkage on the surface will be reduced, because the polymer has more time to relax the stresses, which are lower for low injection speeds, induced during the filling stage. As will soon be shown, the secondary maximum relates to the maximum shear rate developed between the solidified layer and the centre. To try to understand the maximum value on the surface, not explainable with shear-flow induced orientation, another source of orientation needs to be considered.[19] The advancing front is represented in Figure 4.6. A fluid element, while approaching the flow front, reduces its velocity in the flow direction, and is stretched in the thickness direction, as it spills toward the wall region. When the stretched elements hit the cold wall, they

instantaneously solidify, freezing the orientation induced by the elongational flow, present in the flow front region.

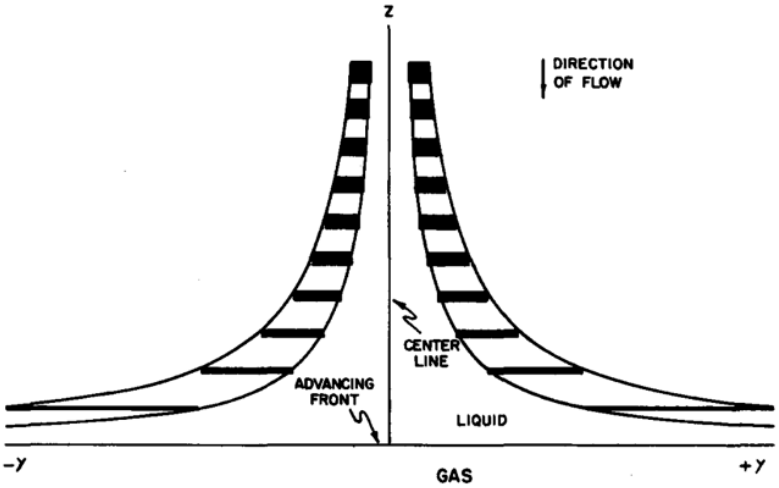

Fig. 2. Schematic representation of the flow pattern in the central portion of the advancing front between two parallel plates. The coordinate system moves in the z-direction with the front velocity. Shaded areas denote the stretching deformation the fluid particles experience.

Figure 4. 6: *Schematic representation of the flow pattern in the central portion of the advancing front. The z-axis represents the direction of flow, the y-axis the thickness. The fluid elements moving toward the front get stretched in the thickness direction while reducing their velocity in flow direction.*[19]

The two-dimensional flow in the front region is important in determining the quality and morphology of the surface. The velocity profile is given by:

$$v_x = 0 \tag{4. 1}$$

$$v_y = \bar{k}y \tag{4. 2}$$

$$v_x = -\bar{k}z \tag{4. 3}$$

k is the elongational strain rate. In the fully developed shear flow, the rate of elongation is given by:

$$-\bar{k} = \frac{v_{max} - \langle v \rangle}{2B} \tag{4. 4}$$

Where v_{max} is the maximum velocity of the fully developed flow and $\langle v \rangle$ the mean velocity. Assuming a power law fluid and an isothermal flow, the maximum velocity is given by:

$$v_{max} = \frac{2n+1}{n+1}\langle v \rangle \tag{4. 5}$$

With n the power law exponent. Therefore, the elongational strain rate become:

$$-\bar{k} = \frac{n}{2B(n+1)}\langle v \rangle \tag{4. 6}$$

The proposed flow pattern implies an orientation in the orthogonal direction of flow, whereas the experimental observation reveals an orientation in the flow direction. This could be explained by the geometry of the advancing front, which is approximated as semi-circular, which spills the fluid particles in a curved path toward the wall, as shown in Figure 4.7. This type of flow pattern is called *fountain effect* or *fountain flow* by Rose. Tadmor was the first to postulate fountain flow as being responsible of the highly oriented surface layer and giving a semi-quantitative model for predicting the elongational strain rate. As already mentioned, the shear flow explains the orientation between the two solidified layers. At the solid interface the shear rate is zero, passes through a maximum and then goes to zero at the centre. Although the exact solution is complex, in literature some works treat this problem, like the one proposed by Gogos. The velocity profile calculated by Gogos indicate a nearly instantaneous build-up of the solidified layer and a maximum shear rate at a certain distance between the interface and the centre. The shear rate distribution is given by the following equation:

$$k = -\frac{(J+1)(J+2)(J+3)}{2}\frac{\langle v \rangle}{B^*}\frac{y}{B^*}\left(1-\frac{y}{B^*}\right)^J \tag{4. 7}$$

where J is an adjustable parameter and B^* is the distance between the centreline and the solidified layer. The shear rate is zero at the centre ($y = 0$) and at the interface ($y = B^*$), while the maximum shear rate is developed at:

$$y = \frac{B^*}{1+J} \tag{4. 8}$$

Since the thickness of the solidified layer increases very slowly, it can be approximated as uniform. Therefore, the velocity profile, and so the shear rate distribution, for a given position, varies little over time.

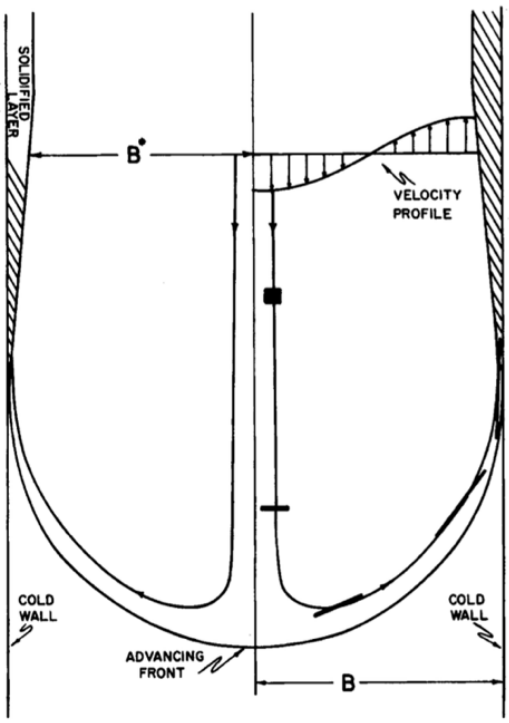

Fig. 3. Schematic representation of the flow pattern in the advancing front between two parallel plates. The shaded areas denote the stretching and orientation of a fluid particle. Due to the curved nature of the advancing front, the orientation of the particle arriving to the cold walls will be parallel to the wall. The velocity profile is relative to a moving coordinate system.

Figure 4. 7: *Schematic representation of the flow pattern in the advancing front. A fluid element, while approaching the flow front, decreases its velocity in the flow direction and accelerates in the thickness one, getting stretched while spilling towards cold walls.*[19]

Figure 4.8 shows the complex state of orientation induced by the fountain flow upon cessation of flow. In the skin layer there is a high orientation due to the elongational flow in centre region and no time to relax, while the orientation between the skin layer and the centre is contribute of shear flow. The orientation distribution, as function of time, is shown in Figure 4.9. In the skin layer there is a high orientation because the polymer instantaneously solidifies, and no relaxation phenomenon occurs.

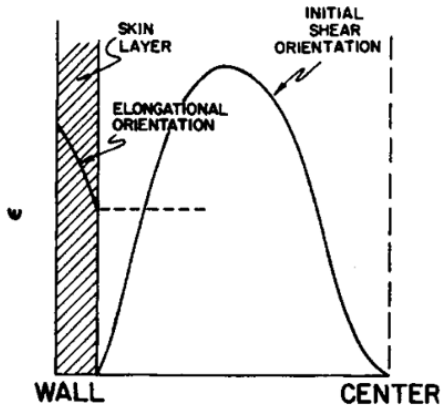

Fig. 6. Schematic representation of elongational and shear orientation upon cessation of flow.

Figure 4. 8: *Schematic representation of elongational and shear orientation at the end of flow. In the skin layer there is a high orientation due to the elongational flow in the flow front. Between the skin layer and the centre, the orientation is due to shear flow.*[19]

Initially, the deeper layers have a higher orientation which is reduced over time because the more available time to relax. Therefore, the complex molecular orientation distribution is due to the flow-induced deformation during mold filling, and the incomplete relaxation during cooling.

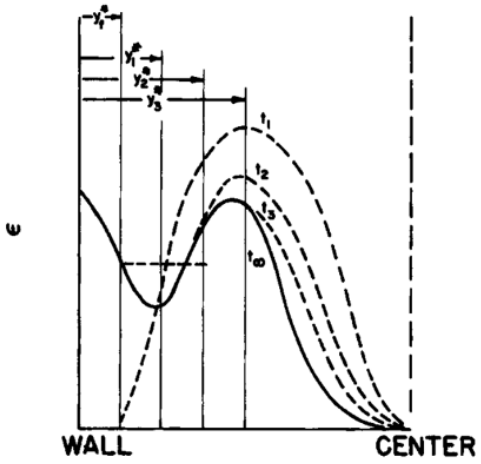

Fig. 7. Schematic representation of orientation distribution at various times: y_f* is the thickness of solidified layer upon cessation of flow; y_1* is the thickness after time t_1, etc. Solid curve indicates final frozen orientation.

Figure 4. 9: *Schematic representation of orientation distribution at various times. Initially the orientation induced by the flow is high but thanks to molecular relaxation it is reduced over time, obtaining the final distribution for* t_∞.[19]

In Schmidt's experiment color tracers, introduced at the centreline, were found on the surface, deformed into V shapes, highly stretched and oriented in flow direction.[16] This experiment supports the hypothesis that fountain flow plays an important role in producing molecular orientation.

5 Aesthetic appearance

5.1 What is gloss?

Gloss is associated with the visual perception of the appearance of a surface observation. It is defined as the ability of a surface to reflect in a specular way the incident light. A perfect specular reflection, with incidence angle equal to the angle of reflection, occurs on mirror-polished surfaces. Rough surfaces reflect the light not only in the principal direction, but even in the others. More uniform is the light diffusion, and more matt the surface will be, due to a smaller specular reflection. Figure 5.1 shows the several type of reflections for different types of surfaces.

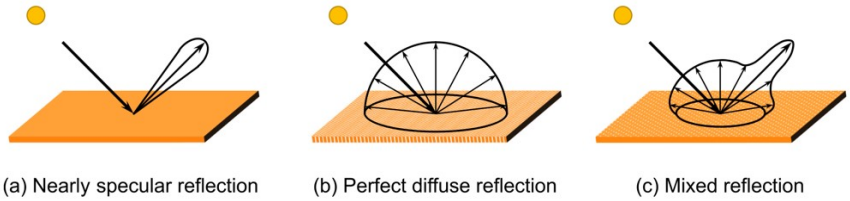

Figure 5. 1: *Types of reflection for different types of surfaces. The nearly specular reflection occurs for a smooth surface, the perfect diffuse reflection occurs for a matt surface and the mixed one for a semi-*gloss *surface.*[20]

Gloss, which is expressed in Gloss Units [GU], is obtained by the ratio between the intensity of the reflected light from the sample and the intensity of the reflected light from a standard (usually a black glass). The intensity of the reflected light depends on the material bulk and surface properties and on the angle of incidence, especially in materials like polymers. For this reason, precise comparisons of gloss values are meaningful only when they refer to the same measurement procedure and same general type of material. A glossmeter is an instrument that measures the specular reflection. Gloss can be evaluated at various angle of light incidence, as shown in Figure 5.2, based on the type of material.

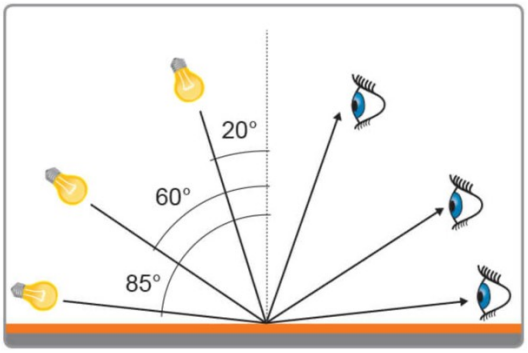

Figure 5. 2: *Specular reflection. A glossmeter measures the gloss value at various specular angles. The principals are 20°,60° and 85°.*[21]

As it will be shown, the 20° geometry is suggested for high-gloss surfaces.

5.2 Dependence of gloss on particle size

In 1985 Lednicky and Pelzbauer investigated the relationship between gloss and the inner morphology of ABS. [22] The purpose of their work was to try to find a new method to analyse the morphology of the dispersed phase. Since the technique typically used was labor-consuming and expensive (ultrathin material sections, contrasted with OsO_4 analysed with a *Transmission Electron Microscope*), they tried to find a correlation with a quick and easy property to measure: the gloss. By studying a series of ABS samples processed in the same way, they derived the following relationship:

$$G = G_M exp\left(-\frac{D}{D_0}\right) \tag{5. 1}$$

which describes the dependence of the gloss value on the particle size. The expression also describes the two limiting cases: $G = G_M$ for $D \to 0$ and $G = 0$ for $D \to \infty$. The value $G = 1$ expresses the 100% of gloss (standard). By considering the logarithm, it is possible to obtain the linear relation reported in the following equation:

$$ln\, G = ln\, G_M - {}^{D}/_{D_0} \tag{5. 2}$$

Then, gloss, depending on G_M and D_0, should not vary as long as the other sample parameters, except D, remain the same.

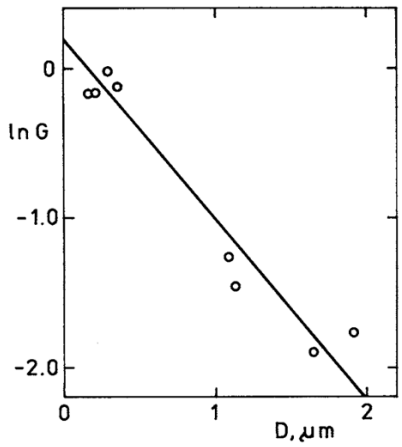

Fig. 1. Verification of the validity of Eq. (3) — linear dependence of values of the gloss logarithm G on the size of rubber particles D.

Figure 5. 3: *Linear dependence of the gloss values on rubber particle size. The points are experimental data. The line represents the relationship found by Lednicky and Pelzbauer.*[22]

Figure 5.3 shows that the experimental data are well described by equation (5.2) and the values of the parameters G_M and D_0 were found to be 1.5 and 0.75 μm, respectively.

5.3 Generation mechanism of gloss

It is well known that for the same material, the gloss is not uniquely determined but depends strongly on the molding conditions. This dependency is intrinsically explained in the definition of the replication factor.

5.3.1 The replication factor

To obtain a high-gloss surface a high replication of the mold is necessary. Jinsu Gim and Byungohk Rhee, studying the generation mechanism of gloss defects, defined a dimensionless parameter R, called "r*eplication factor"*, which is strongly correlated with the gloss.[23] It is expressed as the ratio between the pressure, at which the melt is subjected during the mold filling, and the increasing surface stiffness during the cooling process.

The melt pressure acts like a driving factor for the replication because it allows to press the polymer onto the mold surface. The surface stiffness, on the other side, acts like a resisting factor, because the sooner the polymer recovers the stiffness, the less the time available for the replication. These two parameters depend on the molding conditions, like flow injection speed and mold temperature and on the the melt properties, like polymer viscosity and storage modulus. An increase of the mold temperature and the flow injection speed leads to an increase of *R* and thereby of gloss, for the reasons explained above. Surely the replication factor plays an important role in determining the gloss value but it cannot explain the differences measured for the three samples investigated in this thesis. In fact, as will be shown later, they have the same *R* value, the only significant difference being the swelling index. Nevertheless, some works in literature prove to be helpful for a better understanding of the mechanisms of gloss generation and surface defects of injection-molded items. For this reason, some of them are reported and briefly summarized below.

5.3.2 Gloss transition defect

Jinsu Gim and Byungohk Rhee studied the generation mechanism of gloss defects in high-glossy injection molded objects [20],[23],[24]. The gloss transition defect is characterized by a gloss difference perpendicular to the direction of the flow front, as shown in Figure 5.4. They suggest that the gloss difference is caused by the different replicating capability of the shrinking surface. During the solidification the polymer shrinks and, if the melt pressure is not sufficiently high to compensate, it poorly replicates the mold.

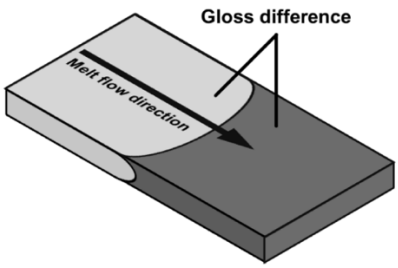

Figure 5. 4: *Gloss transition defect represented as a difference in gloss perpendicularly to the flow direction.*[23]

As shown in Figure 5.5, the fountain flow at the flow front brings the melt towards the mold wall, where a thin layer of polymer instantaneously reaches the contact temperature T_c defined as:

$$T_c = \frac{b_p T_{melt} + b_m T_{mold}}{b_p + b_m} \tag{5. 3}$$

b_p and b_m are thermal diffusivity of the polymer and of the mold, respectively, defined as:

$$b_p = \sqrt{\rho_p C_p k_p} \tag{5. 4}$$

$$b_m = \sqrt{\rho_m C_m k_m} \tag{5. 5}$$

where ρ_p, C_p, k_p and ρ_m, C_m, k_m are the density, the specific heat, and the thermal conductivity of the polymer and of the mold material, respectively. Generally, the contact temperature is a few degrees higher than the mold temperature due to the higher thermal diffusivity and density of steel, material of which the mold is generally made. So, the polymer contacting the mold, instantaneously solidifies, generating the so-called frozen layer.

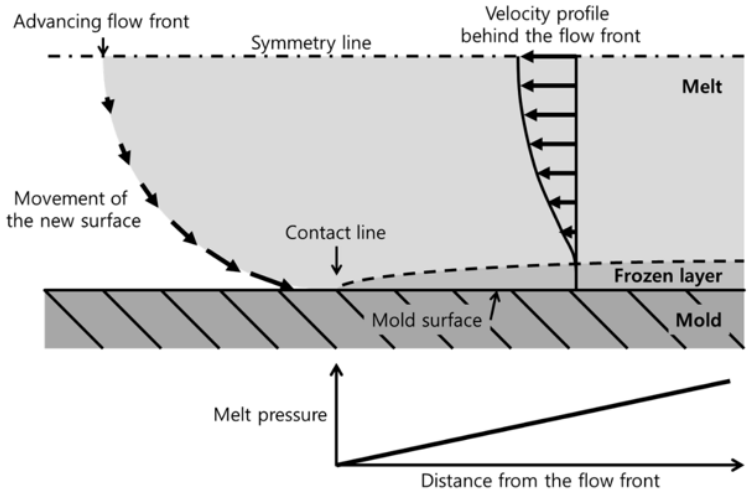

Figure 10. Fountain flow and melt pressure development at the flow front.

Figure 5. 5: *Fountain flow during the mold filling and melt pressure development. Increasing the distance from the flow front the pressure increases.*[24]

As already said, during the cooling, the polymer tends to shrink and if it has inhomogeneous morphology, such as ABS, it results in superficial asperity because the locally differential shrinkage. At a certain position behind the flow front the pressure increases because the contact length increases, and so the shrinking surface is pushed toward the mold wall. If the pressure is sufficiently high, the roughness of the surface approaches that of the mold giving a better replication.

The surface stiffness is mainly influenced by the mold temperature. If this is maintained as high as possible, the stiffness recovers slowly, and the softer polymer surface has more time to replicate the mold. Therefore, the shrinking surface and the difference in the mold replication seem to be the cause of the gloss transition defect. It is important to say that the filling stage is the most important one for gloss formation. Gloss defects generated during this stage are hardly removed during the packing stage. To eliminate the gloss transition defect, it is important to obtain a uniform and high flow front speed, a uniform and high mold temperature. The melt temperature has a lower impact on surface gloss due to the cancellation of effects. In fact, a higher melt temperature decreases both the surface stiffness and the melt pressure. What has been mentioned up to now explains the reason of an increase of gloss by increasing the flow injection speed and the mold temperature, as it will be presented in some of the experimental results of this work. Furthermore, Hirano *et al.* [25] studying the generation of tiger stripes on Polypropylene/Ethylene-Propylene rubber talc blends, suggested the high melt elasticity as responsible of the highest replication of the mold, because it allows to press the melt polymer onto the mold surface. Even though they analyzed a phenomenon that does not occur in this case, they provided the cue for the evaluation of the die swell of the samples. So, the higher elasticity should make a further contribution to the increase in replication factor and then in gloss value.

5.4 Estimation of gloss from rough surface parameters

As already mentioned, gloss strongly depends on the surface topography and/or inhomogeneities in the material's bulk, because a fraction of the incident light is scattered into directions other than the specular one. For this reason, rough surfaces have low gloss values. A correlation between gloss value and surface roughness is a complex task to be

modelled. The first studies were attributed to Alexander-Katz and Barrera [26], which found analytical for gloss for exponential and Gaussian correlation functions, stressing that it is important to consider the incoherent contribution, especially for reasonably glossy surfaces. Simonsen *et al.* (2005) [27] derived an analytical solution for the estimation of gloss from the surface roughness parameter R_q values reported in the following expression:

$$Gloss = exp\left[-16\left(\frac{\pi\sigma}{\lambda}\right)^2 cos^2\theta\left\{1 - 2\left(\frac{G(a)}{\lambda}\right) sin\,\Delta\, cos\,\theta\right\}\right] \tag{5. 6}$$

where σ is the root-mean square roughness (R_q or RMS), λ is the incident light wavelength of the glossmeter, Δ is the collection angle of the glossmeter and θ is the incident light angle of the glossmeter with respect to the vertical line. $G(a)$ is a function depending on the correlation length (a) defined as follows:

$$G(a) = \left(\frac{2}{\Delta}\right) atan(\Delta \cdot a) \tag{5. 7}$$

Figure 5.6 shows the trend of gloss values predicted by equation (5.6) at 20° as a function of R_q, considering three values of λ: the two extremes of the visible range and a mean value of 550 nm.

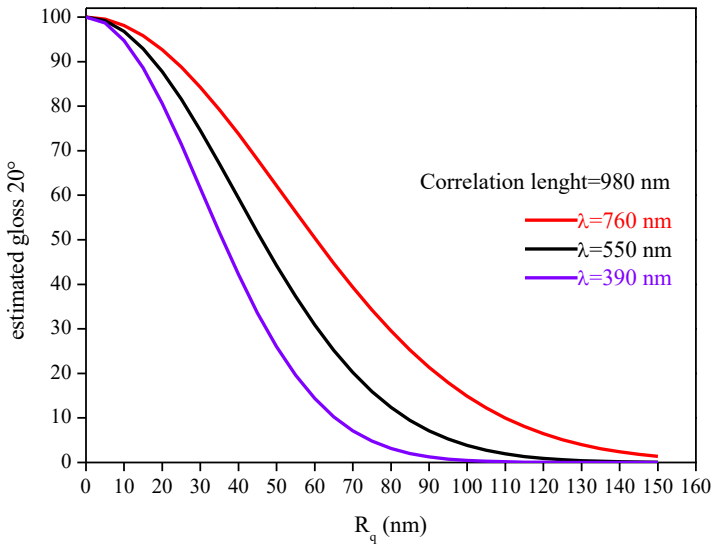

Figure 5. 6: *Estimated gloss at 20° as function of root-mean square roughness (R_q). There are three different curves for different values of incident light wavelength (for the same R_q the gloss is higher for higher λ.*

The correlation length is a measure of the range in which fluctuations in one region are found to be influenced by (correlated with) those in another region. This parameter influences the estimated gloss and consequently the position of the curves. Imagine having a sinusoidal profile, defined in a certain interval on the x-axis. If this were to be "stretched" along the x-axis, one would still get a sinusoidal profile but with a longer wavelength and consequently a smaller amplitude. What would then be seen is a flatter profile. This is a rough explanation of the reason why by increasing the correlation length the gloss becomes greater even if the roughness is the same.

5.5 The formation of surface roughness

Nowadays, surface instabilities on polymers are exploited to produce a wide variety of surface patterns for many applications such as substrates for cell growth, microchips, or for controlling the interfacial adhesion, friction and lubrication. Basically, there are two ways to obtain surface instabilities: spontaneously or applying external stimuli. Burrell demonstrated that by pairing a rigid top layer and an elastic substrate, creating a bilayered system, wrinkle formation can be achieved.[28] By using a mechanical stress force, the elastic substrate is stretched, and the rigid layer is deposited. Through the release of the applied stress, the substrate tends to return to a relaxed state of equilibrium, but this leads to the generation on the surface of a wavy structure, due to the buckling of the rigid material. In literature the minimum force needed to produce wrinkles on the surface of bilayer systems is reported as follows:

$$F = E_s \left[\left(\frac{\pi}{\lambda}\right)^2 \frac{wh^3}{3(1-\nu_s^2)} + \frac{\lambda}{4\pi} \frac{E_f w}{(1-\nu_f^2)E_s} \right] \tag{5. 8}$$

where h is the thickness, w is the width of the skin layer, E_s, ν_s and E_f, ν_f are the elastic moduli and the Poisson coefficients of the skin layer and of the substrate, respectively, and λ is the sinusoidal deflection profile. When F exceeds a critical value buckling occurs and the wavelength of the wrinkled profile can be calculated with equation (5.9), supposing that $dF/d\lambda = 0$:

$$\lambda_c = 2\pi h \left[\frac{(1-\nu_f^2)E_s}{3(1-\nu_s^2)E_f}\right]^{1/3} \tag{5. 9}$$

Considering Figure 5.5 and by analogy with the present case, it is possible to imagine the molten bulk hot polymer as the elastic substrate and the frozen layer as the rigid material. It is known that the frozen layer is immediately created when the melt contacts the mold surface, and it increases in time due to the cooling process of the entire object. As it is explained in §4.2, the frozen layer contains the high orientation due to the elongational flow because the presence of the fountain flow effect. The increase in flow injection speed leads to both higher shear rates and higher elongational stresses, and then higher orientation. As mentioned, the innermost layers of molten polymer have more time to relax the induced orientation compared to the superficial ones, which are progressively more and more rigid. This differential relaxation can be hypothesized to wrinkle and to form a roughness surface depending on the degree of orientation induced by the injection process. Furthermore, since ABS is a two-phase material, the surface morphology is correlated with the rheological behavior of the dispersed phase. The fact that on the surface there are both oriented matrix macromolecules and rubber particles, can lead to a more or less wrinkled morphology related due to the differential relaxation of the two phases. Then, the roughness may be thought as due to two contributions: the differential relaxation between the frozen layer and the bulk, and the differential relaxation between the matrix and the deformed particles.

6 Materials and instruments

6.1 Samples

The samples are ABS obtained via mass production technology, with a salami-like rubber morphology, produced by *Versalis S.p.a*. Since production batches are characterized by average properties derived from continuous sampling during production, it was decided to repeat some analysis to measure more precisely some of the nominal properties. The results show that they substantially differ only for the swelling index values, which are slightly different from those indicate as average values of the standard production batches. For this reason, a nominal swelling index value was used in the label of the samples while the real value was considered in data elaboration.

Table 6. 1: *Characterization of samples.*

Property	*Measure Units*	IR16	IR25	IR34
Nominal Swelling index (IR)	-	16	25	34
Real Swelling index (IR)	-	18	28.5	32.5
GPC M_n (SAN matrix)	*Dalton*	47830	50794	48197
GPC M_w (SAN matrix)	*Dalton*	131718	139252	132983
M_w/M_n	-	2.75	2.74	2.76
% thermally treated gel phase	-	20.6	20.1	21.4
D [4;3]	*µm*	0.662	0.594	0.778
D [3;2]	*µm*	0.604	0.538	0.725
D_v (10)	*µm*	0.419	0.368	0.525
D_v (50)	*µm*	0.642	0.575	0.762
D_v (90)	*µm*	0.939	0.849	1.07
Span	-	0.808	0.837	0.709

Gel Permeation Chromatography (GPC) is an analytical technique that separates dissolved macromolecules by size, based on their elution, from columns filled with porous gel. It permits to obtain the various molecular weight of the matrix. The measure of the amount of rubber provides the dissolution of the sample, previously heat-treated, in an appropriate solvent (*tetrahydrofuran)*, the separation of gel by centrifugation and its

precipitation with *ethanol*. The rubbery phase fraction is then obtained by gravimetric analysis. It is clearly possible to assume that samples have the same amount of dispersed phase, which is nearly 20%. Figure 6.1 shows the preliminary result obtained for the gloss by the Quality Control laboratory during production sampling, as well as the starting point of the present work. QC found that gloss strongly depends on the sweeling index. These data were obtained by measuring gloss on specimens molded with the QC standard condition for gloss evaluation, as referred to in to §7.6.2.

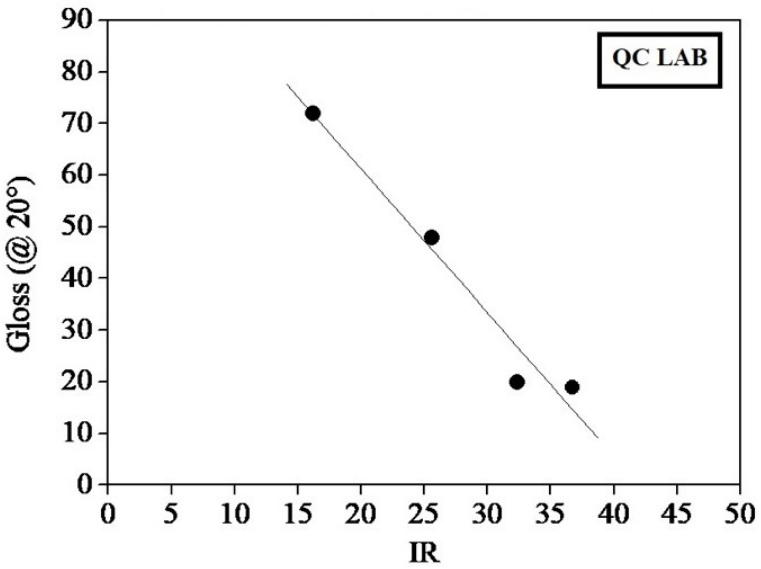

Figure 6. 1*: Gloss at 20° as function of swelling index (IR) obtained by the QC lab during production sampling. Gloss significantly varies with the sweeling index.*

As mentioned in §5.2, rubber particle size affects gloss and for this reason a measure of the particles size distribution is mandatory, to be sure that the differences in gloss cannot be ascribed to a different rubber particle size. Figure 6.2 shows the particle size distribution for the three samples. Considering the maximum particle diameter for each sample, the predicted gloss has been obtained considering equation (5.2).

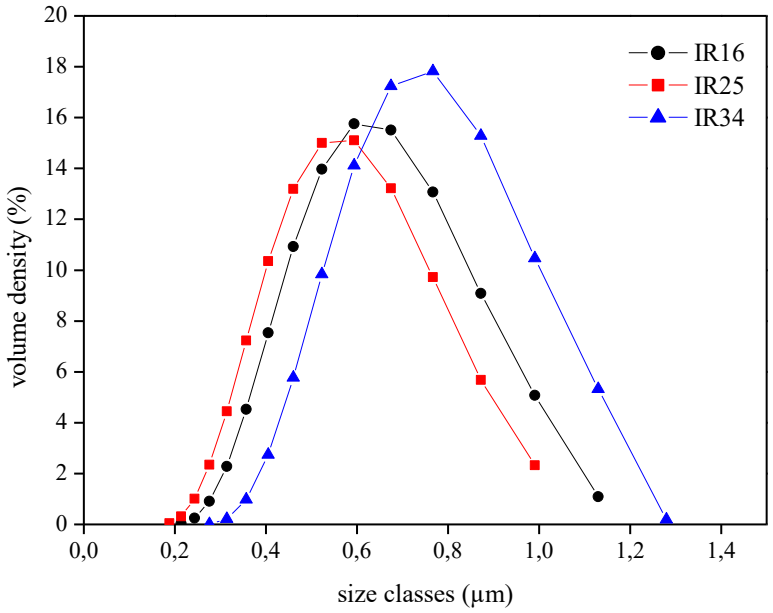

Figure 6. 2: *Size particles distribution.*

Table 6.2 summarizes results and variation (%) of gloss, considering as reference sample IR25. In this way, gloss values of 8% and 21% lower compared to IR25 for sample IR16 and IR34 are respectively expected.

Table 6. 2: *Predicted gloss of samples depending on particle size. Since IR25 shows the lowest particle diameter it is predicted a higher gloss and it has been chosen as reference.*

Sample	D [4;3] (μm)	Predicted gloss Lednicky (%)	% variation
IR16	0.662	62	-8.67%
IR25	0.594	67	-Reference-
IR34	0.778	53	-21.76%

It is possible to conclude that the different gloss values are not due to differences in particle size. If that were the case, to name an example, IR16 should show a lower gloss compared to IR25.

6.2 Injection molding machines

The injection molding machines that have been used in this work are *Engel ES150/50* and *Wittmann Battenfeld Ecopower 55/130*, shown in Figure 6.3.

Figure 6. 3: *Injection molding machines. On the left Engel ES150/50, present in R&D lab, on the right Wittman Battenfeld Ecopower 55/130, present in QC lab.*

Engel ES150/50 is a hydraulic injection molding machine of the Research and Development laboratory (R&D), whereas *Wittmann Battenfeld Ecopower 55/130,* is an electric machine of the Quality Control lab (QC). They use a different cavity mold, which characteristics are reported in Table 6.3.

Table 6. 3: *Cavity mold characteristics.*

Injection molding machine	Thickness of the plaque (mm)	Length of the plaque (mm)	Width of the plaque (mm)	Number of plaque
Engel ES150/50	2.9	60	60	1
Wittmann Battenfeld Ecopower 55/130	3	87	80	1

Both the molds are made of chromium steel because its high corrosion resistance, high workability, and high polishing. The mold temperature is controlled by a water circuit. The main difference between the two injection molding machines is that the electric one allows to obtain a better control of the molding parameters. However, the hydraulic one has a more powerful engine that permits the injection molding of polymers with high viscosities. As it will be shown later, the differences between the two, even if set up with the same molding conditions, will lead to different results.

6.3 Micro-Tri-Gloss BYK

As already mentioned, a glossmeter measures the fraction of incident light which is reflected in the specular direction. Results are not related to the amount of incident light, but they are related to the amount of light reflected by a standard black glass specimen, which has a predefined refractive index. For this standard generally the value of 100 Gloss Units [GU] is assigned. The incidence angle is extremely important to obtain a clear differentiation between surfaces with different glossiness.

Figure 6. 4: *Micro-TRI-gloss BYK. It allows a measure of the gloss value at 20°, 60° and 85° simultaneously.*

Usually three different geometries related to different gloss values are used: the 60° geometry is used to compare most specimens; the 20° geometry is advantageous to

compare specimens having 60° gloss values higher than 70 GU and finally, the 85° geometry is used to compare specimens having 60° gloss values lower than 10 GU. The *Micro-Tri*-Gloss *BYK,* shown in Figure 6.4*,* uses a LED as a source of illumination, and permits quick measurements because simultaneously provides gloss at each evaluation angles.[29] The CIE *(Commission Internationale de l'Eclairage)* has established standard rules to produce illuminant for the reproducibility.[30] The LED used by the glossmeter is a standardized CIE-C, which is intended to simulate the daily light at a temperature of 6774K. This type of light radiation has the mean wavelength positioned at 550 nm. As will be seen later, the wavelength of the incident radiation is a significant parameter for the estimation of gloss from roughness values. The collection angle describes the solid angle of the emerging radiation from the detector source. In the present case the angle is equal to 2.5°.

6.4 Rheometry

Rheometry is the part of rheology that aims to determine the material functions of a fluid through the application and the measurement of macroscopic quantities, using appropriate instruments called rheometers. There are three main flow types: shear flow, elongational flow and complex flows, which are a mix of the two. It is possible to define as viscometric flow as a flow which is locally indistinguishable from simple shear flow. In general, a viscometric flow is generated by instruments that apply shear deformations. Analysable non-viscometric flows also exist, such as that generated by uniaxial elongational flow. Rheometers can operate both applying a stress field and measuring the strain (stress-controlled mode) or vice-versa, applying a strain field and measuring the stress (strain-controlled mode). DMA (Dynamic Mechanical Analysis) is a kind of thermal analysis technique used to characterize viscoelastic properties, as function of temperature or frequency. It can investigate physical properties such as glass transition, damping, relaxation and decomposition under specific environmental conditions, or phase changes such as melt, curing or crystallisation. A typical Dynamic Mechanical Analysis (DMA) plot against temperature for an amorphous polymer is shown in Figure 6.5.

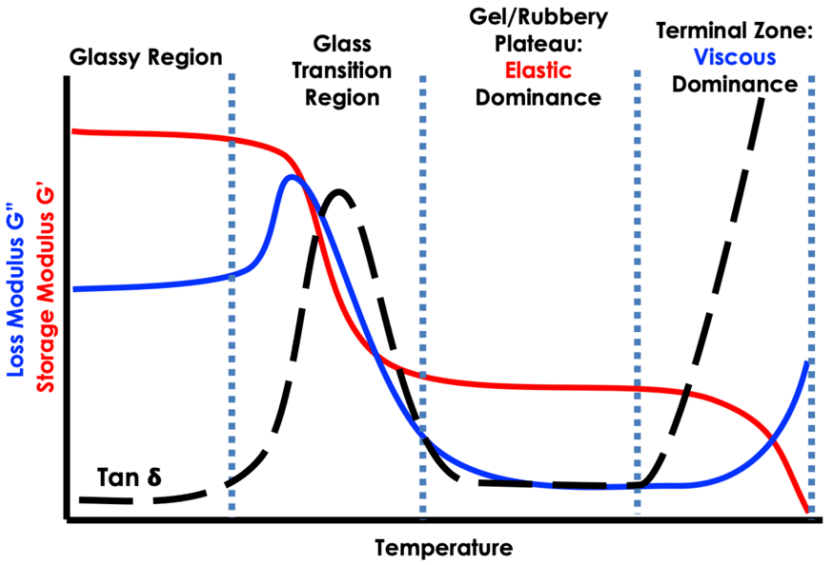

Figure 6. 5: *Typical DMA plot against temperature for an amorphous polymer. The loss modulus, the storage modulus and the loss factor are reported as function of temperature.*[31]

At low temperatures the material is in the glassy state. As the temperature increases the material softens because it approaches the glass transition temperature (T_g). This is marked by a drop in the storage modulus, an increase of the loss modulus and an increase of the loss factor ($tan\delta$). The glass transition temperature is identified by the temperature at which the peak of $tan\delta$ occurs. In the rubbery plateau the material can largely deform with low stresses and the elastic behavior is dominant. With a further increase in temperature, the material starts to behave like a viscous liquid, maybe reaching the phase transition or melting. Geometries used in DMA depend on the type of material at study and are summarized as follows:

- torsion rectangular
- three-point bending
- parallel plates
- cone-plate
- coaxial cylinders

Generally, for solid materials with particularly high modulus, the commonly used geometries are rectangular torsion and three-point bending. In case of polymers with modulus lower than 10^6 Pa rotational rheometers with parallel plate or cone-plate

geometries are used. Coaxial cylinders are used for polymer solutions with low viscosities. A capillary rheometer is a particular type of rheometer that operates in stationary regime and it is useful for measuring the shear viscosity. After this brief introduction on rheometry, all the instruments used and the rheology analysis performed will be presented.

6.4.1 RSA G2

RSA G2 Solid Analyzer, shown in Figure 6.6, is an instrument developed by TA Instruments for mechanical analysis of solids. Motor and transducer are separated to ensure pure mechanical data through independent control of deformation and measurement of stress.

Figure 6. 6: *RSA G2 rheometer, developed by TA Instruments.*[32]

It works in strain-controlled mode, imposing a mechanical deformation on the specimen and measuring the stress response. The environment is controlled by a forced convection oven, designed to perform extremely rapid heating and cooling in a temperature range from -150°C to 600°C. Five thermocouples continuously measure the temperature. It allows to perform many types of analyses with many types of geometries. *RSA G2* has been used to measure the elastic modulus of the ABS considered in this thesis with the three-point bending geometry, represented in Figure 6.7.

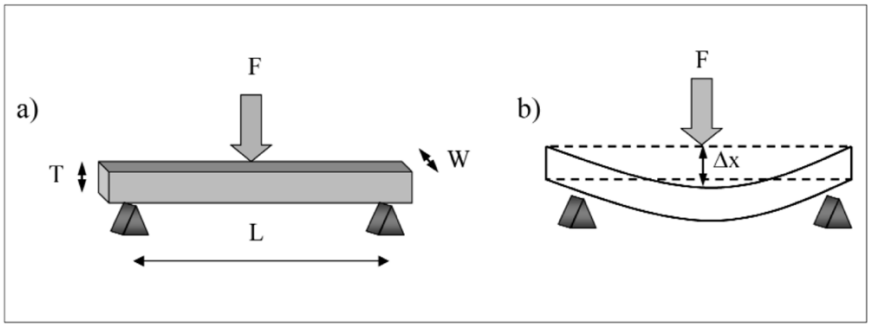

Figure 6. 7: *Three-point bending configuration. The sample is simply placed on two supports and loaded on the centre.*[33]

The specimen has a rectangular shape with known thickness and width. It is placed on two supports, distant L from each other's. The bar is subjected to a linear deflection Δx, thanks to the application of a sinusoidal deformation. A linear voltage displacement transducer registers the force. For this geometry it is important to additionally impose a static load because during the deformation cycle the knife would lose contact with the deformed specimen. To calculate the elastic modulus, stress and strain are required, and equation (6.1) expresses the ratio between the rheological parameters and the imposed and measured quantities:

$$\frac{\tau}{\varepsilon} = K\frac{F}{\Delta x}v \tag{6. 1}$$

K is a geometrical factor equal to $(4WT^3)/L^3$.

6.4.2 RMS800

Rheometric Mechanical Spectrometer Model 800 (RMS800) is another instrument able to measure viscoelastic properties of materials. It has been used to detect the glass transition temperature, with the torsion rectangular geometry, shown in Figure 6.8. The specimen has a rectangular shape, with known dimensions, fixed by two metal clamps. The motor applies an angular deflection θ and the output is the torque M registered. Shear strain is proportional to the angular deflection, while the shear stress is proportional to the torque M.

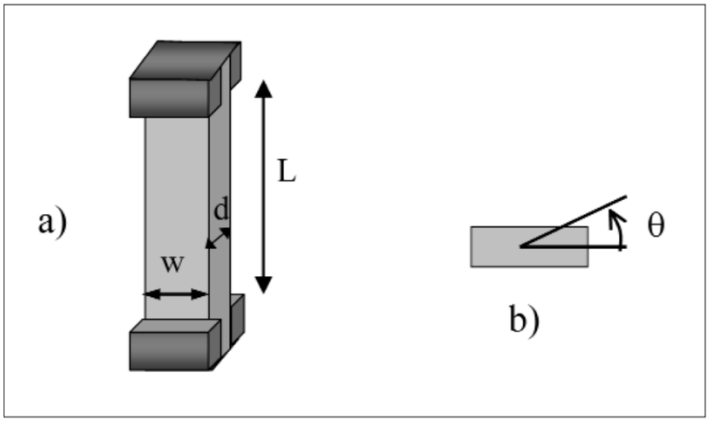

Figure 6. 8: *Torsion rectangular geometry.*[33]

To calculate the viscoelastic functions, such as G', G'' and $tan\delta$ the software uses the following equation:

$$\frac{\sigma}{\gamma} = K\frac{M}{\theta} \tag{6. 2}$$

In this case K is given by:

$$K = \frac{16L}{wd^3 f(\frac{w}{d})} \tag{6. 3}$$

With $f(w/d)$ a numerical factor between 2.249 and 5.333.

6.4.3 RG20

The capillary viscometer tests were performed using a *Göttfert* rheometer (model *RG20)*, shown in Figure 6.9. Capillary rheometers analyse shear flow in the range of high shear rates, typically $1 \div 10^4$ s^{-1}. They are substantially composed by a circular cross-section tube, in which the solid material is melted and forced to pass through by the action of a piston, and a pressure transducer that measure the pressure drop.

Figure 6. 9: *Göttfert RG20 capillary rheometer.*[34]

The viscosity is determined measuring the volumetric flow rate and the pressure drop, according to the equation of Hagen-Poiseuille, which is valid in case of isothermal, stationary and laminar flow [7]:

$$\eta = \frac{\pi r^4 t \Delta p}{8V} \tag{6. 4}$$

where Δp is the pressure-drop, V the volume of fluid that flows through the capillary during a time t, and r the capillary radius. On the market there are capillaries of various length-diameter ratio values and different geometries. However, two types of circular cross-section capillary have been used: a L/D=30/1 and a L/D=0/1/90°. Defining the geometry in cylindrical coordinates (r, z, ϑ) and making a force balance it is possible to obtain the expression of the shear stress:

$$\tau(r, z) = \frac{r}{2}\frac{\partial P}{\partial z} \tag{6. 5}$$

If the gradient of pressure is constant, τ increases with the radius and it doesn't depend on z. At the wall ($r = R$) the shear stress is:

$$\tau_w = \frac{RP}{2L} \tag{6. 6}$$

The shear rate varies with the radius, and it is maximum at the wall:

$$\dot{\gamma}_w = \frac{RP}{2L\eta} \tag{6. 7}$$

For a Newtonian fluid the velocity profile is parabolic and, in case of a constant pressure gradient equal to P/L, it is possible to correlate the shear rate to the volumetric flow rate, obtaining the following expression of viscosity:

$$\eta = \frac{\pi R^4 P}{8LQ} \tag{6. 8}$$

In case of power-law fluids the velocity profile assumes different configurations, according to the value of the flow index *n*, as shown in Figure 6.10.

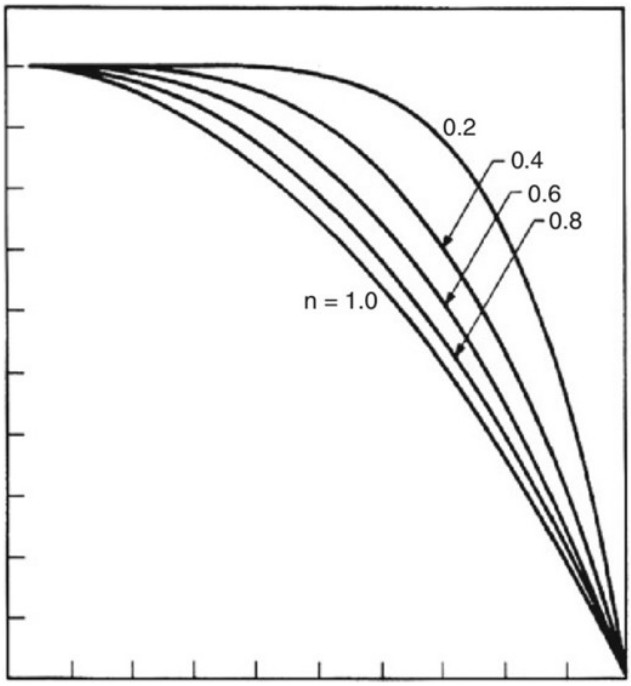

Figure 6. 10: *Velocity profiles for Newtonian fluids (n=1) and power-law fluids. Decreasing the value of the flow index n, the velocity profile becomes flat and the shear rate at the wall is greater.*

For n<1 the velocity profile is more or less flat (plug-flow), and the shear rate at the wall is higher compared to the Newtonian case. The Rabinovitch correction allows to calculate the real shear rate for non-Newtonian fluids:

$$\dot{\gamma}_w = \left(\frac{3n+1}{4n}\right)\dot{\gamma}_{app} \tag{6. 9}$$

$\dot{\gamma}_{app}$ is the "apparent shear rate" relevant to the Newtonian fluid case. A feature to be considered when dealing with viscoelastic fluids, such as polymers, is the elasticity of the melt, which leads to the occurrence of normal stresses in shear flows. The rod climbing or "Weissenberg effect", is a consequence of fluid elasticity, whereby immersing a rotating rod in a polymeric melt, this tends to raise the rod, whereas in case of a Newtonian fluid, this experience a depression of the free surface. Capillary rheometers allow to measure the die swell which is related to the melt elasticity. In fact, at the exit of the tube, the diameter of the extruded material is higher than that of the capillary. For the same material the die swell depends on the shear rate and on temperature. The Tanner's empirical rule allows to calculate the normal stress N_1, knowing the die swell B and τ_w:

$$N_1 = 2\tau_w(2B^6 - 2)^2 \tag{6. 10}$$

Another measure connected with the fluid elasticity is the entrance pressure representing the effect of viscoelastic vortices developed at the entrance of the capillary, especially at high shear rates. Furthermore, the recoverable shear, which is the ratio between the normal stress and the shear stress, is often evaluated.

6.4.3.1 Cogswell's model

The Cogswell's model allows to predict the elongational viscosity if the entrance pressure and the flow index are known. Cogswell calculated for the elongational stress the following expression:

$$\tau_{el} = \frac{3}{8}(n+1)P_{ent} \tag{6. 11}$$

The elongational strain is also calculated and results in this equation:

$$\dot{\varepsilon}_{el} = \frac{4}{3}\frac{\dot{\gamma}_{app}\eta_{app}}{(n+1)P_{ent}} \tag{6. 12}$$

The elongational viscosity immediately follows using equations (6.11) and (6.12):

$$\eta_{el} = \frac{9}{32}\frac{(n+1)^2 P_{ent}^2}{\eta_{app}\dot{\gamma}_{app}} \tag{6. 13}$$

This model is particularly useful when a direct measure of the elongational viscosity with classical elongational rheology tests (EVF) is not possible, for the reasons exposed in §6.4.4.1.

6.4.4 ARES

The *Advanced Rheometric Expansion System (ARES)* is a mechanical spectrometer developed by TA Instruments, shown in Figure 6.11.

Figure 6. 11: *ARES rheometer.*

It can impose on a sample either a dynamic (sinusoidal) or steady shear deformation while measuring the resultant torque which relates to the sample response. Shear strain is applied by the motor, and the torque is measured by the transducer.[35] In dynamic mode the motion is oscillatory, with a certain imposed frequency and the instrument measures the strain and the torque. In steady mode, the motor rotates at a specific rotational shear rate and the transducer measures the torque and, eventually, even the normal force. The control of the environment is kept by a forced air convection oven. It can perform a range of temperatures from ambient to 600°C, with a temperature ramp rate from 0.1 to 50°C/min. If temperatures below room temperature are required, it is possible to use the optional LN_2 controller, which employs liquid nitrogen to reach temperatures until -150°C. *ARES* has been used for many DMA analyses such as frequency sweep, strain sweep, time sweep and temperature ramp tests. Furthermore, it has been used for elongational viscosity tests equipped with a special tool, the "Elongational Viscosity Fixture" (EVF). This is a particular analysis which allows to measure the extensional viscosity of highly viscous materials. The strain sweep test is used to determine the linear viscoelastic response (LVR), within the other oscillatory tests will be then performed. Strain sweeps are also suggested for the characterization of samples that exhibit extreme non-linear behavior, such as filled thermoplastics. Time sweep provides information on time-dependent behavior of a material, such as thermal degradation, curing and built-up o breakdown of network structure. Frequency sweeps are used to analyse frequency and time dependent behavior. Generally high frequencies correspond to short times and low frequencies to long time scales. Temperature ramp tests are used for analysing the temperature sensitivity of a sample. The geometry used for DMA measures is the parallel plate, represented in Figure 6.12. Parallel plates are generally used to measure the three linear viscoelastic functions (G', $G''$and $tan\delta$) in the low-medium frequency range, typically 10^{-3} and 10^{2} rad/s. The specimen requires a circular shape, with known radius and thickness, and it is placed between the two plates. The motor applies an angular deflection with a certain angular frequency and the output is the torque, measured by the transducer.

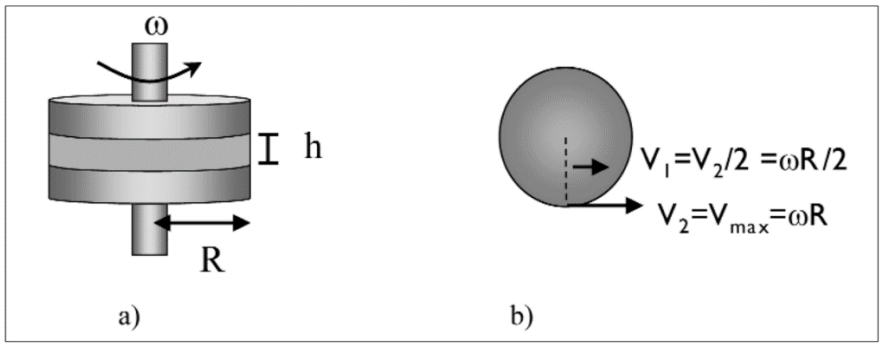

Figure 6. 12: *Parallel plates geometry, generating a non-uniform viscometric flow.* [33]

It is important to note that this geometry produces a non-uniform viscometric flow and shear rate increases linearly with the radius. Then, some corrections are needed in case of non-Newtonian behavior.

6.4.4.1 Extensional Viscosity Fixture (EVF)

Tensile tests can provide important information on the rheological behavior of materials. This method allows to measure the elongational viscosity of viscoelastic materials subjected to a uniaxial tensile state of stress. A rectangular specimen is fixed between two clamps positioned onto two drums. The EVF geometry is reported in Figure 6.13. One clamp is fixed while the other rotates so to stretch the specimen. The fixed drum is coupled with the motor while the other rotates and is fixed to the transducer, which measures the torque. Specimen dimensions, like width and thickness are required for the calculation of the rectangular cross-section area. The instantaneous value of strain is given by the Hencky strain, defined as follows:

$$\varepsilon_H = ln\left(\frac{L}{L_0}\right) = \dot{\varepsilon}_H \cdot t \tag{6. 14}$$

Where L_0 is the initial free length of the sample, L is the length measured during the test, $\dot{\varepsilon}_H$ is the extensional strain rate and t is the time. The exponential form considers that the specimen during the test reduces its cross-section because of the lateral contraction.

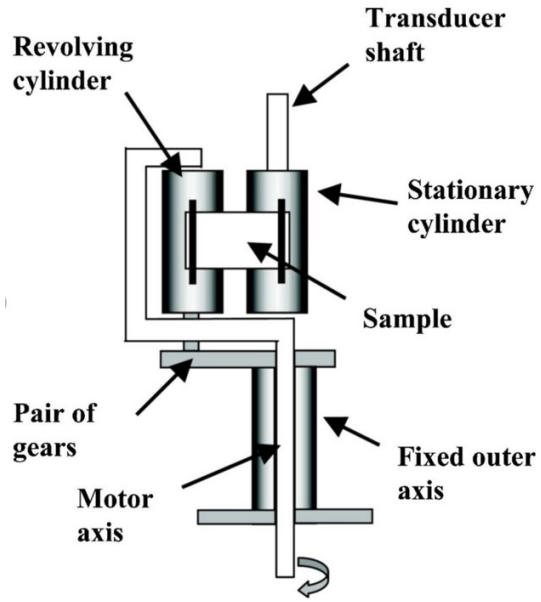

Figure 6. 13: *Scheme of Elongation Viscosity Fixture (EVF) test. The specimen is fixed between two clamps, and it is stretched by the rotational movement of a cylinder connected with the motor. The fixed drum is connected with the transducer and measures the torque.*[36]

The elongational viscosity is defined as the ratio between the elongational stress and the elongational strain rate as follows:

$$\eta_{el} = \frac{\sigma}{\dot{\varepsilon}_H} \tag{6. 15}$$

In Figure 6.14 both the strain hardening and the strain softening phenomena are represented. The black curve represents the trend of the transient shear viscosity or of the elongational viscosity in the linear regime, which is equal to three-times the zero-shear viscosity as stated by the Trouton rule. Strain hardening occurs when the extensional viscosity deviates upward from the transient shear viscosity. Strain softening is a downward deviation from the transient shear viscosity. In case of rigid dispersed phase, the flow, near the particle, has shear as well as elongational components and this leads to a smaller increase in elongational viscosity. In case of deformable particles, the strain hardening phenomenon is emphasised, as explained in §3.3. In fact, the particle, by deforming, contributes to increase the elongational viscosity. Furthermore, once deformed, the particle possesses a greater aspect ratio, which further increases η_{el}.

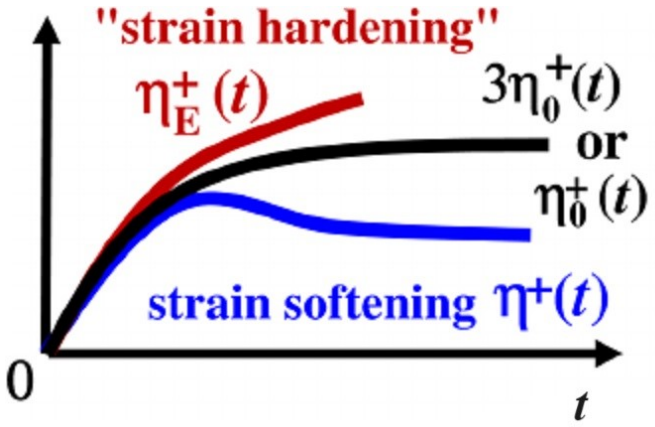

Figure 6. 14: *Schematic trend of viscosity over time. The black curve is the transient shear viscosity (or the three-fold the elongational viscosity in linear regime, for the Trouton rule). The red curve represents the strain hardening, which occurs during uniaxial stretching. The blue curve represents the strain softening which occurs when the sample is subjected to shear stress.*[37]

The strain hardening index is defined as the ratio between the non-linear elongational viscosity (strain rate-dependent) and the linear elongational viscosity (independent on strain rate).

$$SHI = \frac{\eta_{el}(t)}{3\eta_{shear}(t)} = \frac{\eta_{non-linear}}{\eta_{linear}} \tag{6. 16}$$

For practical reasons, such as the clamping and the collapse of the sample at high temperature, this type of analysis can be performed at relatively low temperatures. For example, in case of ABS, the maximum temperature is around 150°C, after which the above-mentioned problems occur, especially at low elongational strain rates.

6.5 Roughness tester

Materials surfaces can be ideally described as a superposition of tri-dimensional waves with different amplitude (A) and wavelength (λ) in the 3-D space. The norm DIN 4760 defines the shape of a surface as a first-order deviation from flatness, the ripple as a second-order deviation and the roughness as a third- and fourth-order deviations.[38] The surface profile is measured along a straight line and the roughness is then calculated by applying selection filters implemented in the tool. Initially, the instrument acquires the

total profile and with the application of a cut-off wavelength λ_s, which deletes the shortest wavelengths (background noise), derives the primary profile. Successively, the roughness tester, with a least-squares linear regression, derives the medium line, which corrects the slope of the primary profile with respect to a horizontal reference line. At this point, the instrument applies a cut-off value λ_c to suppress the long wavelengths (ripple profile) to obtain the roughness profile on the medium line with $z=0$. Figure 6.15 can help in understanding the concepts.

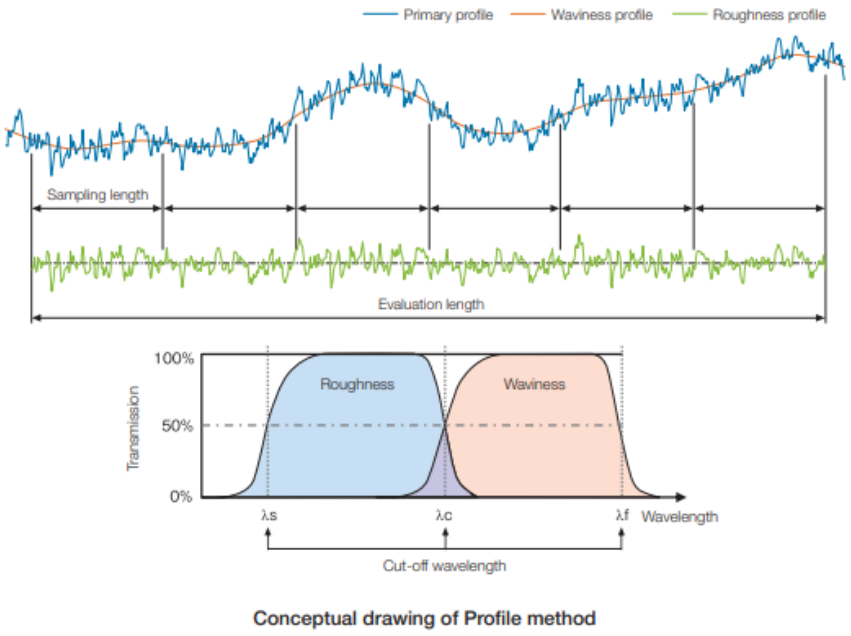

Figure 6. 15: *Surface profiles and selection filters applied by the roughness tester. λ_s derives the primary profile, deleting the shortest wavelengths (background noise). λ_c suppress the long wavelengths (ripple profile) to obtain the roughness profile.*[39]

The following equations are implemented by the roughness tester for the calculation of the amplitudes after the application of cut-off wavelengths:

$$\frac{a_1}{a_0} = e^{-\pi\left(\frac{\alpha \cdot \lambda_s}{\lambda}\right)^2} \tag{6. 17}$$

$$\frac{a_2}{a_0} = 1 - e^{-\pi\left(\frac{\alpha \cdot \lambda_c}{\lambda}\right)^2} \tag{6. 18}$$

with a_1 and a_2 are the amplitudes after filters application, a_0 is the original amplitude of the profile, λ the applicable wavelength and α is a constant equal to 0,4697. Based on the roughness profile measured, the roughness tester had been used two values of λ_c:

- 0,25 mm for R_a= 0,02÷0,1 µm
- 0,8 mm for R_a =0,1÷2 µm

The roughness is measured on an evaluation length equal to five times the sampling length (λ_c), from which the arithmetic mean value is calculated. These operations are automatically performed by the roughness tester.

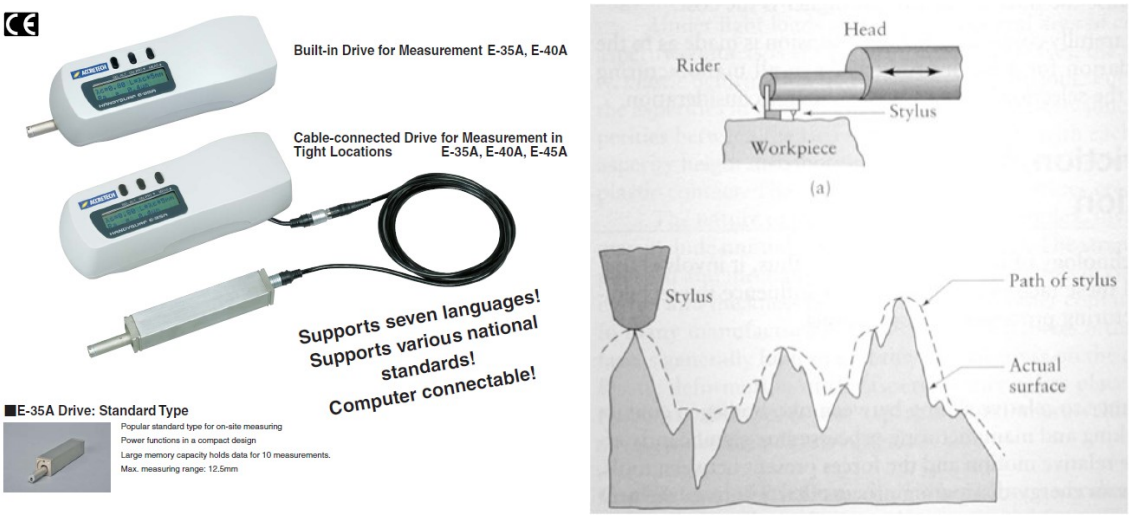

Figure 6. 16: *Zeiss Handysurf E-35A roughness tester.*

The roughness was measured with a portable roughness tester Zeiss Handysurf E-35A shown in Figure 6.16.

6.6 Scanning Electron Microscope (SEM)

The working principle of the Scanning Electron Microscope (SEM), reported in Figure 6.17, is based on the surface sample scanning with a point beam of high-power electrons (5-40 keV). Electrons are generated through the heating of a filament, generally made of tungsten, and they are focused on the surface sample. SEM requires vacuum chamber to avoid the interference of the dust and air with the primary beam.

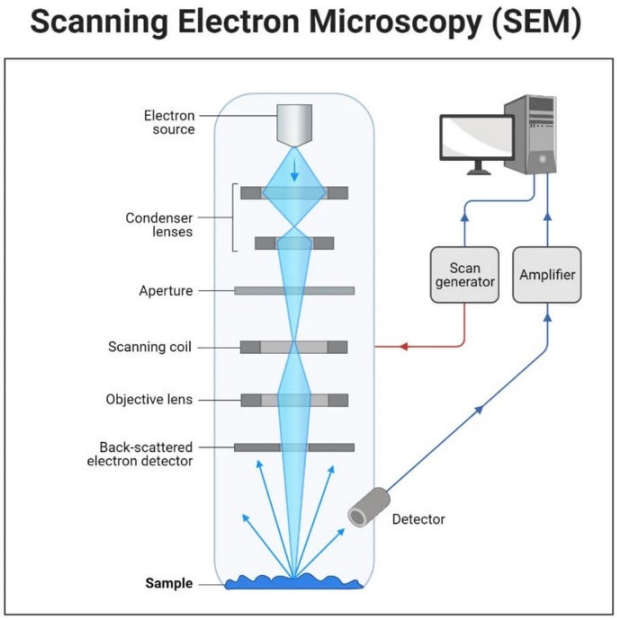

Figure 6. 17: *Scanning Electron Microscope (SEM). The electro gun generates the electrons that are accelerated by an anode. The magnetic lenses focus the electrons onto the sample, and a detector detects the different types of signals.*[40]

When the electrons encounter the sample surface, they interact with it through elastic and anelastic collisions, which generate different types of signals. These emitted particles or radiations are detected by appropriate detectors, and they can be subdivided according to their energy and interaction as follows:

- Backscattered Electrons (BSE): they come from an elastic interaction between the incident electrons and the nuclei of the atoms constituting the sample. So, they have the same energy as the incident ones and give information, quantified by a greyscale, about the sample composition and morphology. Based on the energy of the incident beam it is possible to modify the penetration thickness, and then obtaining different information.
- Secondary Electrons (SE): they derived from the interactions of primary electrons with the outermost electrons of sample surface atoms, which received enough energy to set free. Since it is an anelastic interaction, the SE have lower energy compared to BSE. In this way they allow to obtain only information on sample surface morphology.

- Auger Electrons: when a primary electron has sufficient energy to ionize an atom, the innermost electrons are shunted out, leaving an unoccupied orbital. So, to reduce its energy, the atom needs to move an electron to the innermost vacant position, with the consequent production of a x-photon, which interacting with an outermost electron provides the necessary energy to set free. This type of electron has characteristic energy of atoms, so it permits to recognize the atomic species. Since it comes from thin superficial layers (1-3 nm) it is mandatory that the surface is free from any contamination. Furthermore, an ultra-high vacuum is required.
- X rays: they have a characteristic energy, so they allow to identify the elements both qualitatively and semi-quantitatively.

SEM has been used to analyze the surface morphology of molded samples as well as the possible particle migration on surface, using the BSE.

6.7 Transmission Electron Microscope (TEM)

Transmission Electron Microscope (TEM) is an instrument that allows to obtain high resolution images and provides information on morphology and micro-structure of samples.

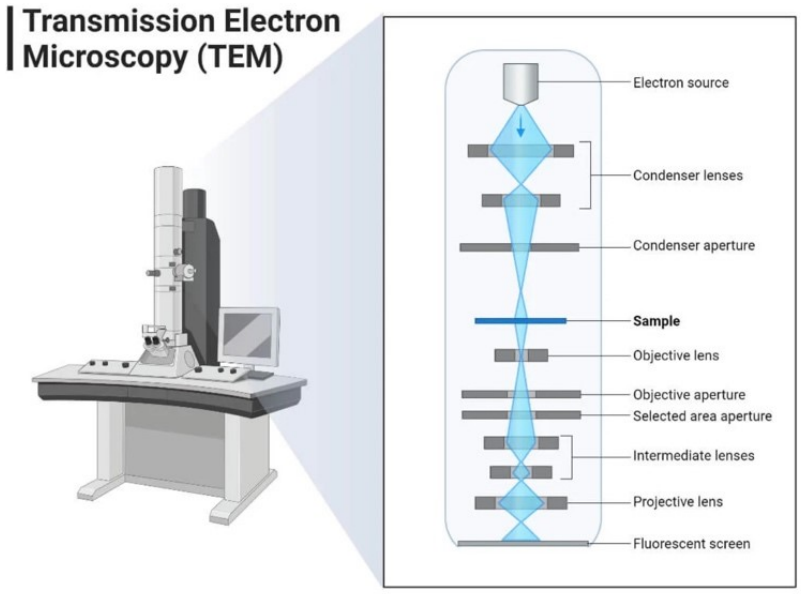

Figure 6. 18: *Transmission Electron Microscope (TEM). A source of electrons and some lenses focus the beam on the sample. In this case, depending on the constituting elements, electrons can pass through the sample, or can be absorbed, creating a black and white image.*[41]

It uses a beam of highly focused electrons directed towards an ultra-thin specimen, with thickness of 50-500 nm (microtome). The electron beam is generated by the heating of a tungsten filament. It releases electrons which are accelerated through a magnetic field. The image obtained with TEM shows different colored areas according to the ability of the sample components to absorb or transmit the electrons. Indeed, areas of the sample that can absorb or scatter electrons will appear darker than those that are able to transmit electrons, whose color will be brighter. Sample preparation requires to cut, in case of solid specimen, very thin slices using an ultramicrotome. Before the cutting, specimens are placed in a 4% aqueous solution of *osmium tetroxide* (OsO_4) for 2 days to stain the polybutadiene phase. This passage is required because osmium atoms react with the unsaturated rubber of the sample making it more electron-absorbent. This will provide a strong contrast between the dark rubbery phase and the lighter matrix phase when images are generated.

7 Experimental work and results

7.1 Measure of the swelling index

The swelling index or IR represents an indirect measure of the rubber cross-linking degree inside ABS. The swelling of a polymeric lattice is a phenomenon which consists in an increase in volume by dissolving the polymer in a solvent. The basic idea of the measure of the swelling index is that the more cross-linked the particles are, the less space is available for the solvent to enter and swell. In fact, IR is obtained by gravimetric analysis, through the ratio between the weight of gel swollen in a solvent and the weight of the dry gel. First, the polymer is mixed with *acetone* (C_3H_6O), which is a matrix solvent. After the complete dissolution, the sample is centrifugated and the liquid matrix is separated from the gel. Then, *tetrahydrofuran* (THF) is added to gel. A crucible filter is weighted (W_1) and placed in a container with THF solvent. After some time, when the septum has absorbed the maximum amount of solvent, it is re-weighted (W_2). The gel is put on the porous septum, and it is left some time to permit the swelling of the rubber, after that the crucible is re-weighted (W_3). At this point, the gel is precipitated with *ethanol* (C_2H_6O), filtered and dried. Finally, the crucible filter with the dry gel is weighted (W_4). The swelling index is so calculated with the following equation:

$$IR = \frac{W_3 - W_2}{W_4 - W_1} \tag{7. 1}$$

Then, high values of IR indicate low cross-linking degrees of rubber.

7.2 Measure of the Elastic Modulus

To test the surface stiffness, parameter needed to determine the replication factor, it was decided to measure the elastic Young modulus E. This is expected to be very similar for the three ABS samples because they possess the same gel content. Polymer granules, previously dried in an oven at 60°C under vacuum for at least 4 hours, were compression

molded with a manual heat press at 190°C for a few minutes. For the three-point bending configuration a rectangular specimen is required, with known thickness and width, as shown in Figure 7.1.

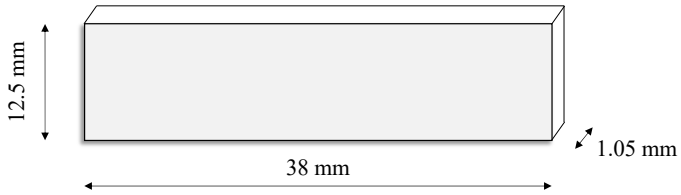

Figure 7. 1: *Rectangular specimen for three-point bending and rectangular torsion tests.*

The elastic modulus has been obtained during a temperature ramp test, performed with *RSA-G2*, starting from 80°C to 150°C (1°C/min).

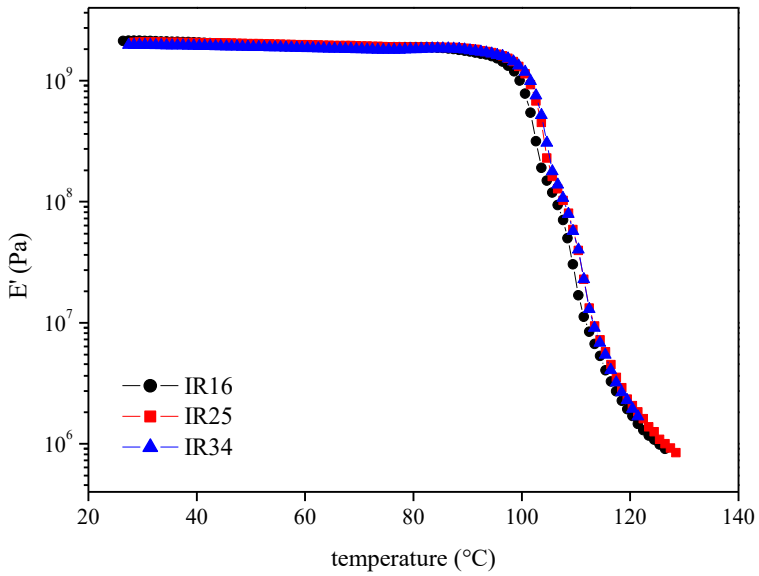

Figure 7. 2: *Elastic modulus E′ as function of temperature.*

Figure 7.2 shows the results obtained. It is possible to note that the elastic modulus is equal for the three samples.

7.3 Measure of the glass transition temperature

Polymer granules, previously dried in an oven at 60°C under vacuum for at least 4 hours, were compression molded with a manual heat press at 190°C for few minutes. The analysis has been performed by *RMS800* with the rectangular torsion configuration. The rectangular specimen, shown in Figure 7.1, has been fixed between two metallic clamps. The dynamic temperature ramp started from 80°C to 120°C by increasing 1°C/min. The imposed strain was 0.1%.

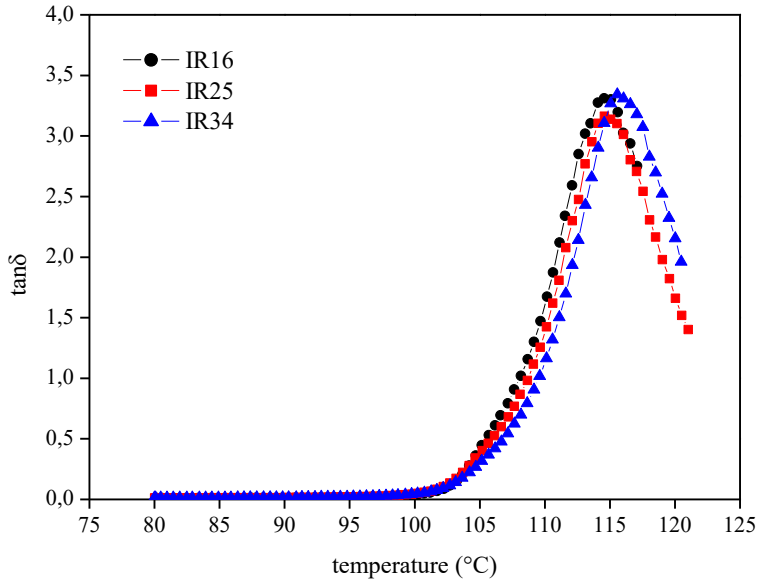

Figure 7. 3: *Loss factor tanδ as function of temperature, measured with the rectangular torsion geometry. The glass transition temperature is identified by the peak of the curve.*

Figure 7.3 shows the trend of the loss factor over a range of temperature. The position of the peak identifies the glass transition temperature, which is about 114°C for samples IR16 and IR25 and 115°C sample IR34. These values are so close that the glass transition temperatures of the three ABS at study can be considered the same.

7.4 Capillary rheometry with RG20

To investigate the different behavior of samples at high shear rates in stationary regime, the capillary viscometer *Göttfert RG20* has been used. Each test was performed both at 200°C and 220°C, with a round hole capillary. It should be stressed that these conditions, between all those realized in the rheometers, are the most similar to those encountered during the injection molding process.

7.4.1 Entrance pressure

The pressure at the entrance of the capillary has been measured with a zero-length capillary (L/D=0/1/90°), to calculate the elongational viscosity with the Cogswell's model. The obtained results are reported in Figure 7.4.

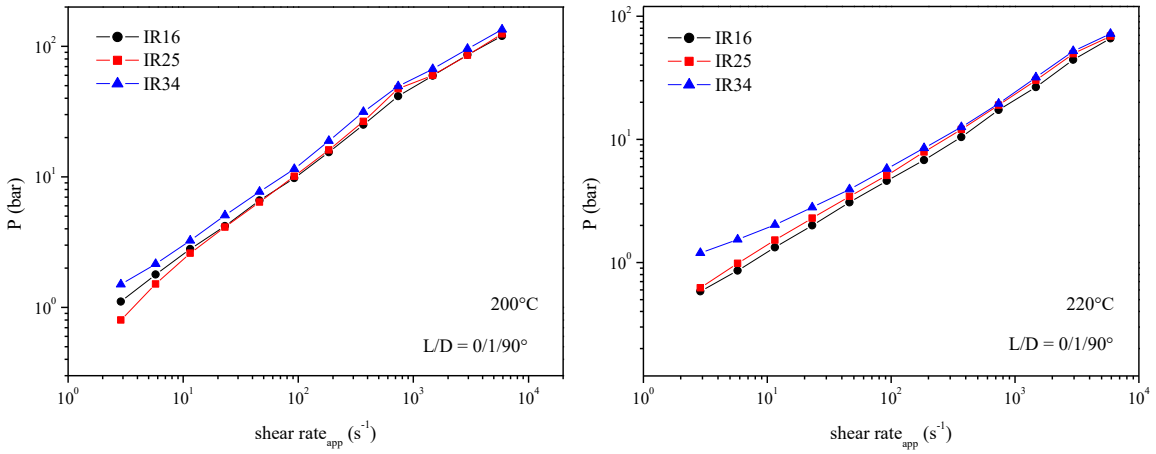

Figure 7. 4: *Pressure at the entrance of the capillary as function of shear rate at 200°C and 220°C.*

7.4.2 Shear stress

To calculate the normal stress developed by the melt with the Tanner's rule (6.10), the wall shear stress has been measured at 200°C and 220°C. Figure 7.5 shows that τ is very similar for all samples.

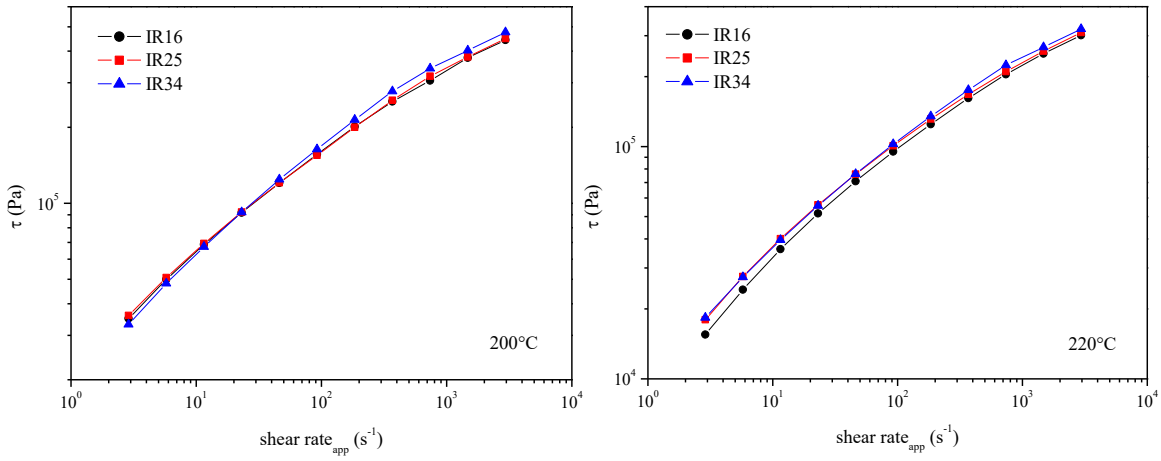

Figure 7. 5: *Shear stress at the wall versus shear rate at 200°C and 220°C.*

Since for a power law fluid equation (7.2) holds, the flow index n is represented by the tangent to the curve obtained with the equation (7.3).

$$\tau = K\dot{\gamma}^n \tag{7. 2}$$

$$log\tau = logK + nlog\dot{\gamma} \tag{7. 3}$$

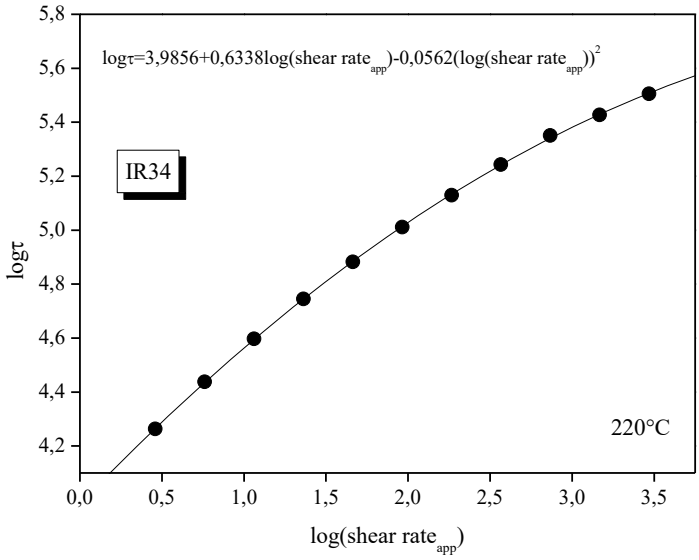

Figure 7. 6: *Logarithm of shear stress versus logarithm of shear rate for sample IR34 at 220°C. The second-degree polynomial function interpolates the experimental points. The flow index n is given by the first derivative of the curve.*

Then, by plotting the equation (7.3) for each sample and temperature and fitting the data with a second-degree polynomial, it is possible to obtain the flow indices by taking the first derivative of the interpolating function. Figure 7.6 shows an example of the interpolating function for the sample IR34 and T=220°C.

7.4.3 Shear viscosity

To analyse the samples behavior when subjected to stationary shear flow, like the one developed during the filling stage, the shear viscosity has been calculated.

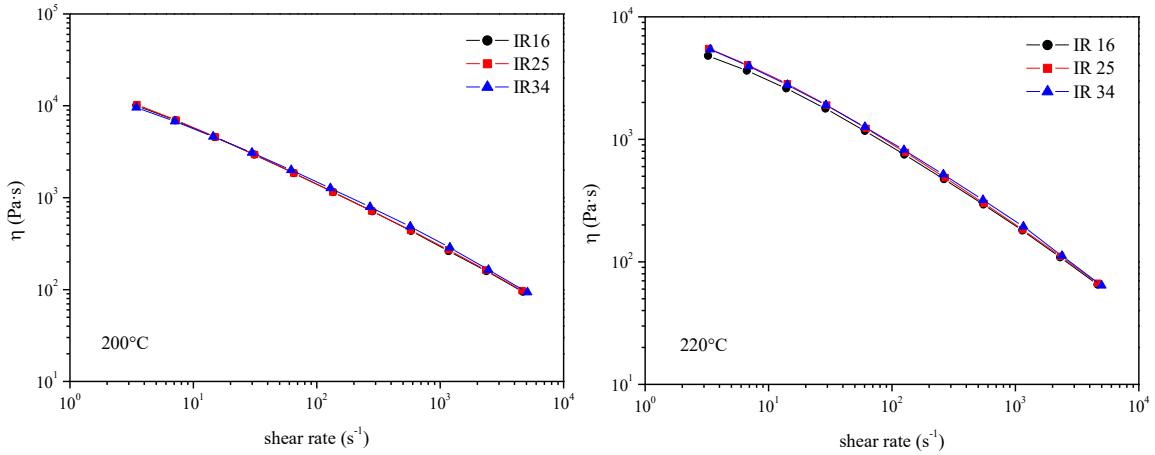

Figure 7. 7: *Shear viscosity versus shear rate at 200°C and 220°C.*

Figure 7.7 shows that the shear viscosity is identical for the three samples and then the melt pressure, one of the two parameters involved in the replication factor, is the same. On the x-axis the corrected shear rate is reported, obtained applying the Rabinovitch correction accounting for non-Newtonian effects.

7.4.4 Calculation of the elongational viscosity

To calculate the elongational viscosity, the Cogswell's model was used which requires the following parameters: the pressure at the entrance of the capillary, the shear stress, the apparent shear rate, and the flow index. To calculate the elongational stress the

(6.11) has been used. Then, (6.12) allows to calculate the elongational strain rate and finally with the ratio between the stress and the strain rate it is possible to obtain the predicted elongational viscosity. Figure 7.8 reports the results obtained for both temperatures for which the data was derived.

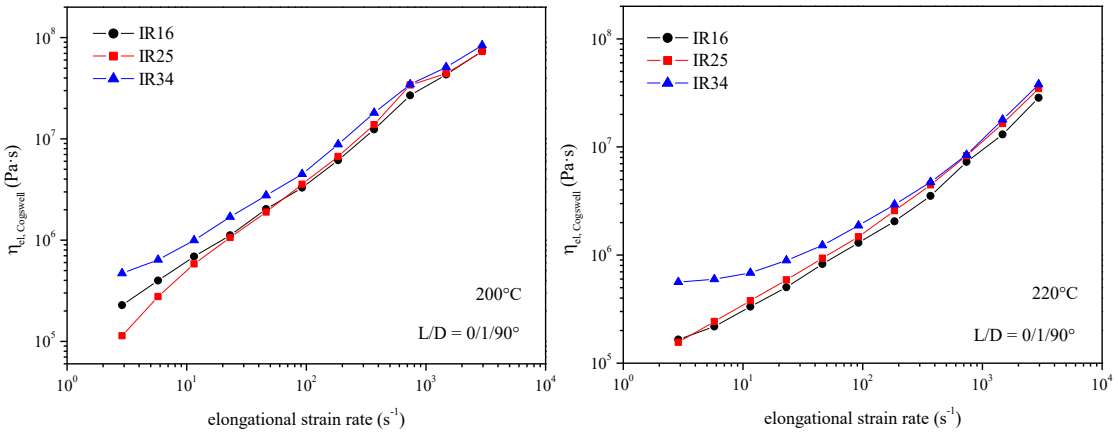

Figure 7. 8: *Predicted elongational viscosity at 200°C and 220°C.*

According to Cogswell the three samples clearly seem to exhibit different rheological behavior in case of elongational flow. Recalling the estimation of the elongational strain rate made by Tadmor in equation (4.6), it is possible to calculate for the present case the range of elongational shear rates developed during the injection molding process. *B* is the semi-thickness of the mold cavity, which is equal to 1.5 mm, *n* is the flow index, which for simplicity will be assumed constant and equal to 0.3. The mean velocity is the variable parameter because of the three chosen flow injection speeds. Table 7.1 reports the estimated elongational strain rate values.

Table 7. 1: *Estimated elongational strain rates for the three flow injection speeds chosen.*

Flow injection speed (mm/s)	**Elongational strain rate $\dot{\varepsilon}$ (s^{-1})**
100	7.69
200	15.39
300	23.08

Considering the estimated elongational strain rate range and the data reported in Figure 7.8, it is clear that samples don't behave in the same way.

7.4.5 Die swell

As previously mentioned, die swell is the phenomenon that can occur when a material is extruded due to the relaxation of the normal stress, developed during the extrusion, at the exit of the capillary. It can have a strong influence on the dimensional stability of the extrudate. Die swell is higher when the material has high elasticity. Being a manifestation of elasticity, it increases by increasing shear rate and decreasing melt temperature. Figure 7.9 show the die swell B as a function of shear rate for both temperatures. These data confirm that sample IR34 exhibits the highest elasticity.

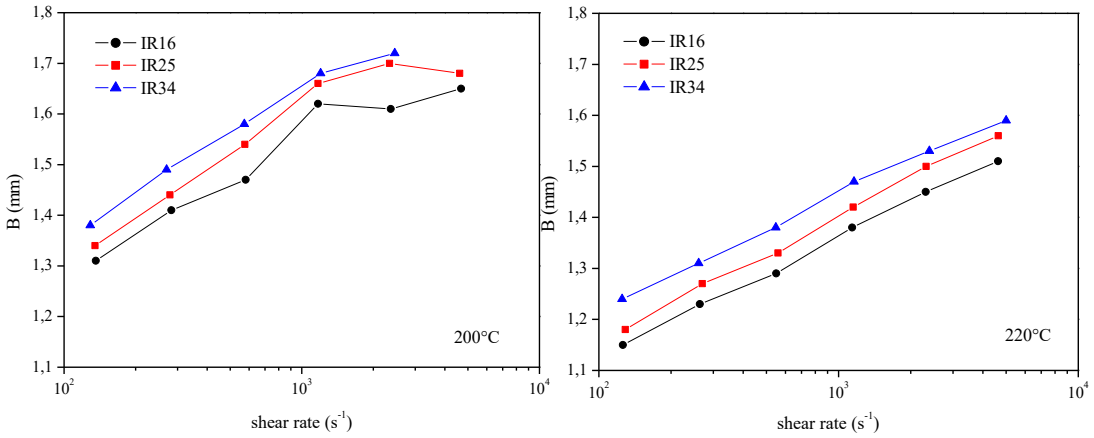

Figure 7. 9: *Die swell B versus shear rate at 200°C. The higher the IR, the higher the die swell, and consequently the elasticity of the sample.*

This measure will be also used for the calculation of the normal stress developed by the shear flow during the extrusion.

7.4.6 Calculation of the normal stress N1

A non-Newtonian fluid when subjected to shear flow develops normal stresses, more or less elevated, according to the elasticity of the material. In case of stationary shear flow, the stress tensor is given by:

$$\bar{\bar{\sigma}} = \begin{pmatrix} \sigma_{xx} & \sigma_{xy} & 0 \\ \sigma_{yx} & \sigma_{yy} & 0 \\ 0 & 0 & \sigma_{zz} \end{pmatrix} \tag{7. 4}$$

where $\sigma_{xy} = \sigma_{yx}$ is the tangential stress, and σ_{xx}, σ_{yy} and σ_{zz} are the normal stress components. Dynamic quantities of rheological interests are σ_{xy}, $N_1 = \sigma_{xx} - \sigma_{yy}$ and $N_2 = \sigma_{yy} - \sigma_{zz}$. The presence of normal stresses must be taken into consideration, especially in the extrusion process, because it leads to undesirable phenomena, such as sharkskin, gross melt fracture, viscoelastic vortices and die swelling. For what was said in §5.3.2, it has been decided to evaluate the normal stress N_1 because it can contribute to increase the pressure with which the melt polymer is pressed onto the mold surface, and then it could increase the replication factor. N_1 has been calculated with the Tanner's law and Figure 7.10 shows its trend as a function of shear rate for 200°C and 220°C.

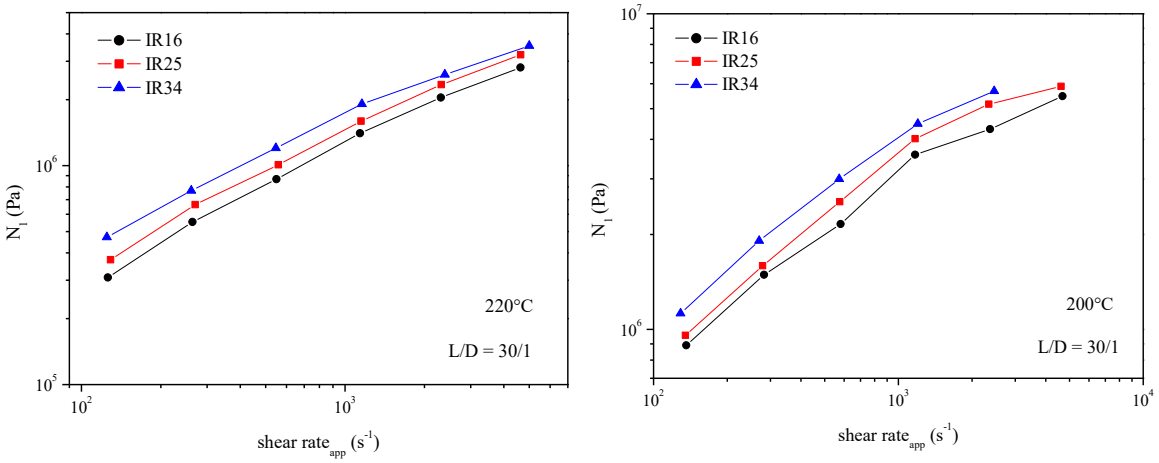

Figure 7. 10: *Normal stress N_1 calculated with Tanner's rule versus shear rate at 200°C and 220°C. Sample IR34 shows a higher normal stress.*

The normal stress for sample IR34 is higher and may result a higher pressure pressing the molten polymer onto the mold surface. Sample IR34 should consequently show the

highest pressure contribution to the replication factor and thus a higher gloss. This is another aspect that leads to think that the replication factor *R* is not the major key for understanding the differences in the samples under study.

7.4.7 Recoverable shear

The recoverable shear was also measured to further evaluate the elastic contribution of the samples when subjected to shear flow. The recoverable strain is related to the elastic recovery and since samples practically differ only in the swelling index it can be related to the elastic capillary number. Figure 7.11 shows the results for both temperatures. As expected, sample IR34 which has the more deformable particles and has shown also higher elasticity in terms of die swell, shows a higher recoverable shear.

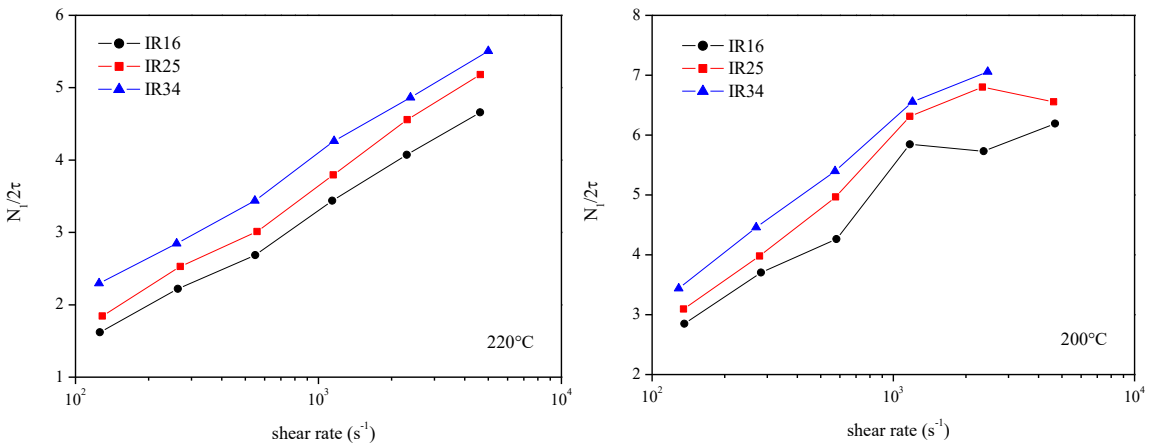

Figure 7. 11: *Recoverable shear vs shear rate at 200°C and 220°C. Sample IR34 shows the highest recoverable shear and then the highest elastic recovery.*

Reconsidering what was explained in §5.5, where the frozen layer is assumed to be the rigid surface and the bulk material underneath it, the elastic substrate where the shear flow acts. It could be possible to assume that a higher recoverable shear leads to a higher elastic recovery, thus generating on the rigid surface layer a higher state of compression which forms a higher roughness when the equilibrium state tends to be recovered. Then, sample

IR34, which shows the highest recoverable shear should show also highest roughness values.

7.5 Rheological measurements with ARES

As mentioned previously strain sweeps, frequency sweeps and time sweeps have been conducted with ARES with the parallel-plate geometry. The specimens, in form of disks as shown in Figure 7.12, have been prepared by compression molding at 190°C the polymer granules, previously heated in an oven at 60°C under vacuum for at least 4 hours.

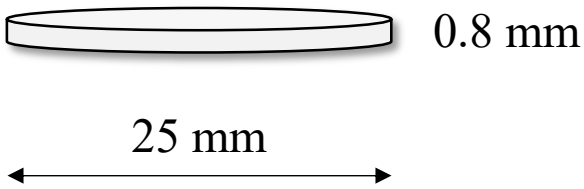

Figure 7. 12: *Specimen dimensions for parallel-plate geometry.*

Strain sweep, frequency sweep and time sweep tests have been performed in a nitrogen atmosphere to guarantee inert environment. The temperature ramp of the rubber has been done in air to investigate the possibility of rubber cross-linking during the injection molding.

7.5.1 Strain sweep

As mentioned, a strain sweep is used for determining the linear viscoelastic regime. In this test temperature and frequency are kept constants, and viscoelastic functions are measured by varying the amplitude of oscillation. The LVR vary by varying the frequency at which the test is performed. Particularly, by increasing the frequency the linear viscoelastic range is reduced. Samples have been subjected to strain sweep test at 200°C. The imposed angular frequency was 1 rad/s and a 5% of strain increment has been set.

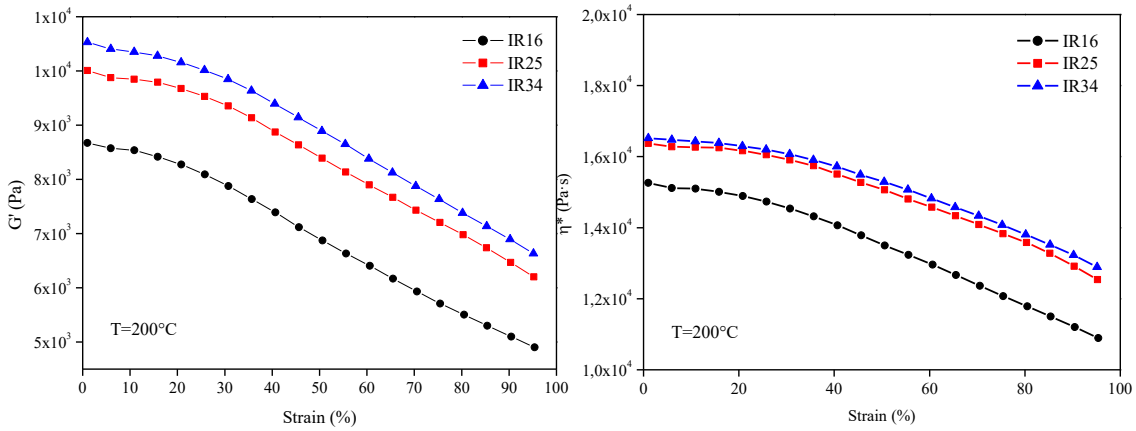

Figure 7. 13: *Strain sweep test at 200°C. Strain dependence of the storage modulus G' and of the complex viscosity η^*. The LVR extends up to absolute strain values of 0.2.*

Figure 7.13 shows the strain dependence of the storage modulus and of the complex viscosity η^*. It is possible to see that up to strain values of 20%, G' and η^* are constant and the LVR is then determined.

7.5.2 Frequency sweep

A frequency sweep test is an oscillatory analysis conducted, in the LVR range, varying the frequency of the applied stimulus. Temperature and amplitude of oscillation are kept constant. The time needed for the analysis strongly depends on the lower frequency chosen. Furthermore, this test allows the collection of curves to which the TTS principle can be then applied, with which the temperature dependency of viscoelastic functions can be explored. Four temperatures have been investigated. Figure 7.14 shows the comparison of complex viscosity values obtained for each sample and temperature. The imposed strain was 2% for 200°C and 220°C, 5% for 240 and 10% for 260°C.

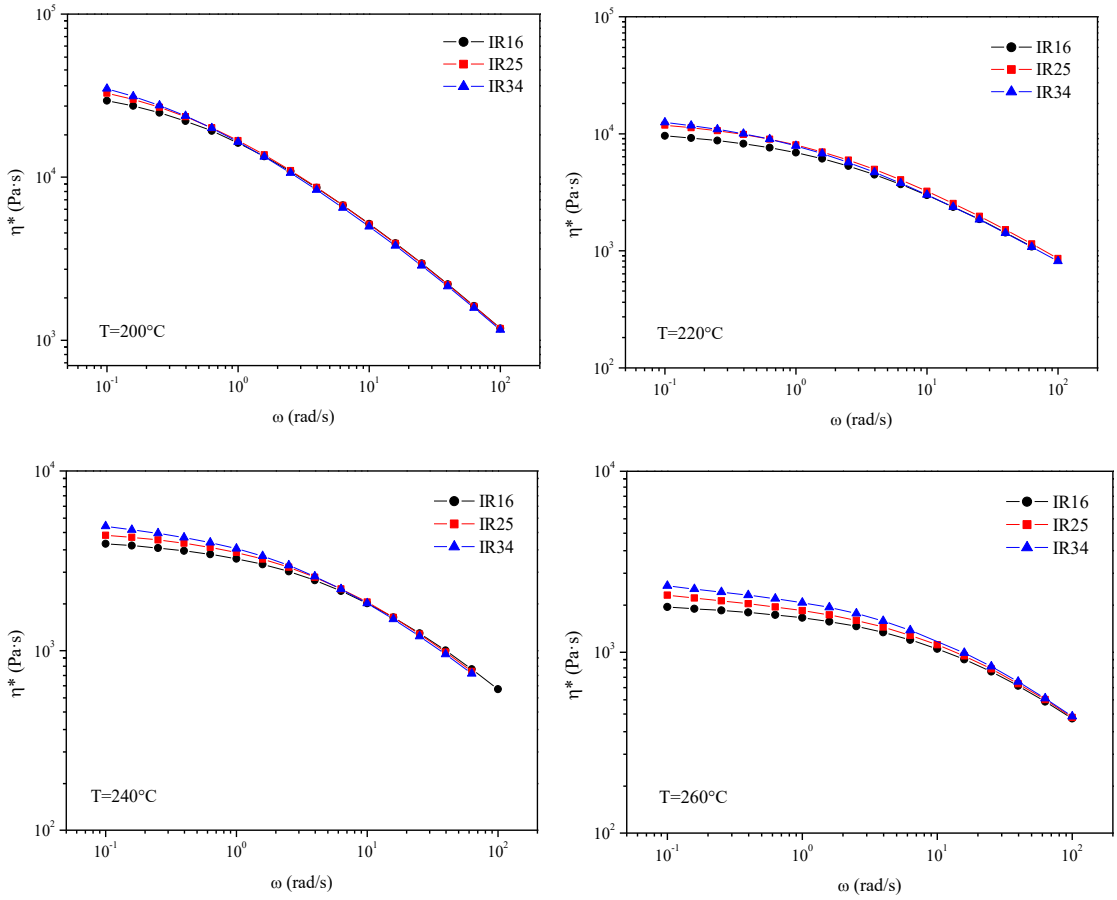

Figure 7. 14: *Complex viscosity vs angular frequency obtained for each sample and temperature investigated.*

Then, also in case of oscillatory solicitations, sample show approximately the same shear behavior, as previously seen in capillary rheometry. Since the melt injection temperature will be set at 220°C, the graphs of G' and G'' at this temperature are reported in Figure 7.15. These will then be referred to in §7.12 for the identification of the polymer relaxation time, defined by the inverse of the frequency at which the cross-over of the moduli occurs.

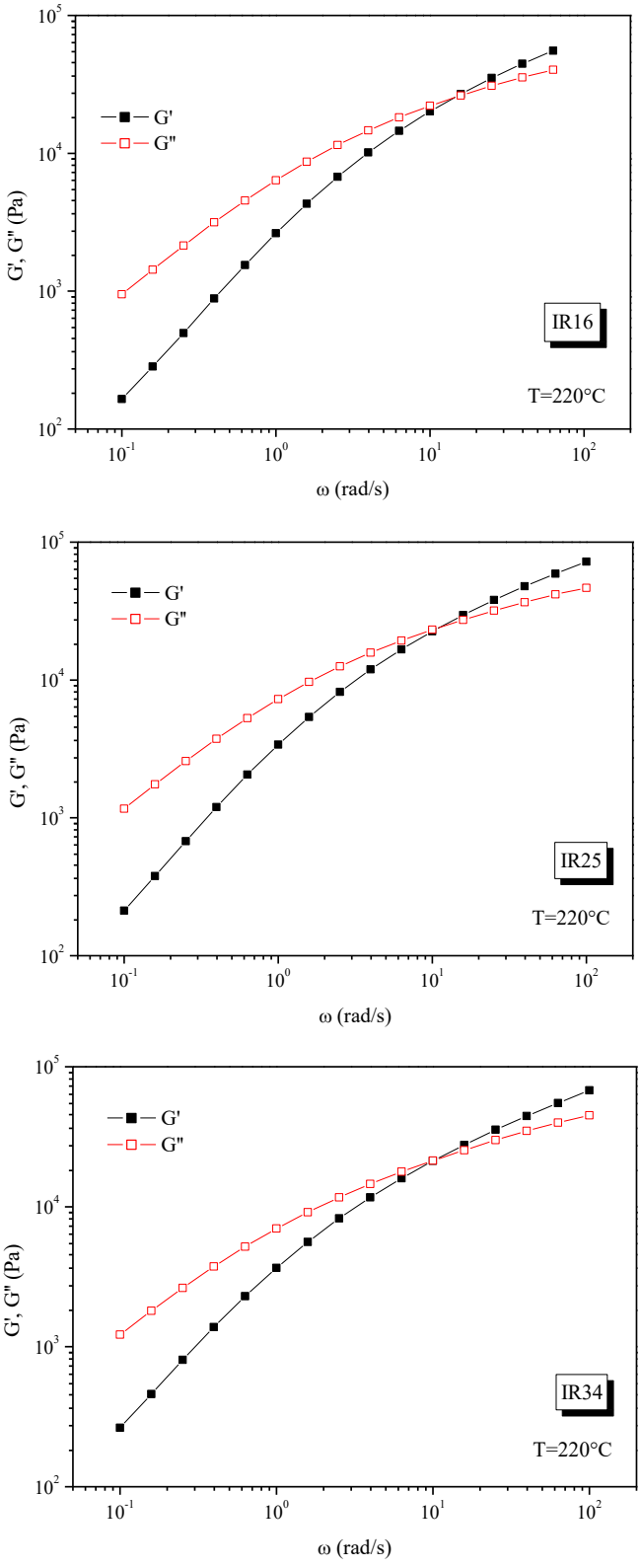

Figure 7. 15: *Storage modulus G' and loss modulus G'' as function of angular frequency at 220°C, for all samples. The inverse of the frequency at which the cross-over of the moduli occurs defines the relaxation time of the polymer.*

7.5.3 Time sweep

In this test the temperature, the frequency and the amplitude of oscillation are kept constants, and the measure is conducted monitoring the viscoelastic functions versus time. A time sweep gives information on kinetic phenomena, such as degradation, curing or network structuring. To verify the stability of samples at high temperatures, time sweep tests at 220°C have been done. The frequency chosen was 1 rad/s, the strain value 2% and the test has been run for 1 hour.

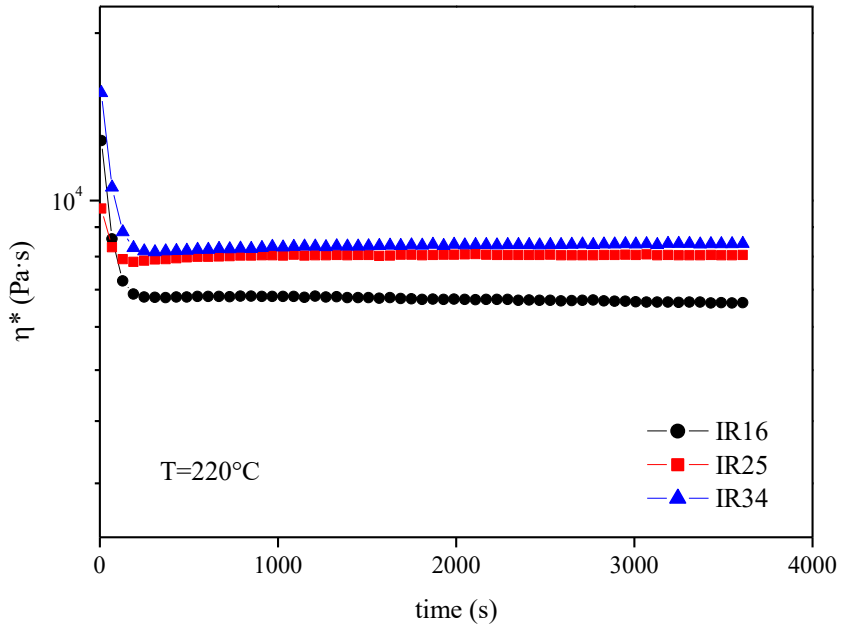

Figure 7. 16: *Time sweep test at 220°C. The constant viscosity over time implies that samples are stable.*

Figure 7.16 shows the time dependence of viscosity. After the first few minutes affected by thermal equilibration of the samples, the curves clearly show that the three ABS at study are stable. This information is important because rubber particles agglomeration phenomena may occur in ABS, due to poor grafting and thus compatibilization, altering the gloss of the surface of injection molded items. In conclusion, time sweeps do exclude these undesired phenomena.

7.5.4 Temperature sweep of the rubber

A temperature sweep test has the aim of investigating the rheological behavior and phase transitions by varying the temperature. In this case the amplitude and the angular frequency of the oscillation are kept constant and a temperature ramp, ascending or descending, is performed. It is important to choose an adequate heating (or cooling) rate to ensure thermal equilibration of the specimen. This test has been performed to verify the stability of the rubber at high temperature. A temperature ramp test (in air) has been performed starting from 100°C until 250°C (scanning rate: 1°C/min). The specimen has been prepared by compression molding at 90°C.

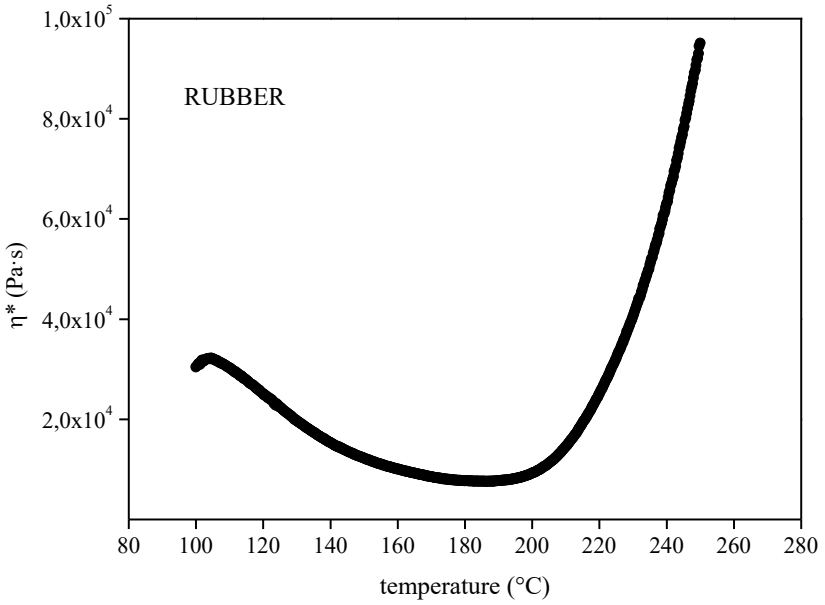

Figure 7. 17: *Complex viscosity η^* versus temperature for the rubber. It is possible to see that at around 220°C the viscosity rapidly increases, and this is due to the cross-linking process.*

The curve in Figure 7.17 shows an increase of viscosity at about 220°C. This means that at this temperature the rubber starts to cross-link. As a consequence, it was decided to investigate the possibility of rubber modification during the injection molding process. This aspect will be discussed in §7.10.

7.5.5 Extensional Viscosity Fixture (EVF)

According to what was explained in §3.3, a different elongational behavior of the three samples is to be expected. To investigate how much the different IR values and thus crosslinking of the rubber could influence to the elongational viscosity, it was decided to perform EVF tests. Rectangular specimens, shown in Figure 7.18, have been prepared by compression molding at 190°C of polymer granules, previously heated in an oven at 60°C under vacuum for at least 4 hours.

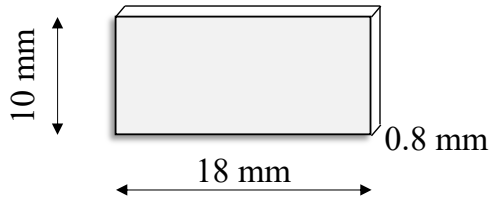

Figure 7. 18: *Rectangular specimen for EVF test.*

It was decided to perform the tests for two values of temperatures: 140°C and 150°C. Curves were measured at three extensional strain rate values $\dot{\varepsilon}_H$ equal to 1 s^{-1}, 0.1 s^{-1} and 0.01 s^{-1} up to Hencky strain ε_H of 3.4. A delay time of 150 s for thermal equilibration of the samples was observed. The required parameters are the dimensions of the specimen, the densities, both of the solid material and of the melt, which were set as 1.0 g/cm^3 and 1.05 g/cm^3, respectively. Figures 7.19 and 7.20 show the elongational viscosities and strain hardening index for 140°C and 150°C, respectively. It is possible to see that, as expected from the theory, samples with higher swelling index IR, and then higher deformability of particles, lead to higher elongational viscosity and strain hardening index. Furthermore, by increasing temperature, the elongational viscosity decreases and the strain hardening increases. The strain hardening has been obtained by calculating the deviation of curves at 0.1 s^{-1} and 1 s^{-1}, considering the curve at 0.01 s^{-1} as the linear envelope (reasonable since the strain rate is low), as defined in equation (6.16).

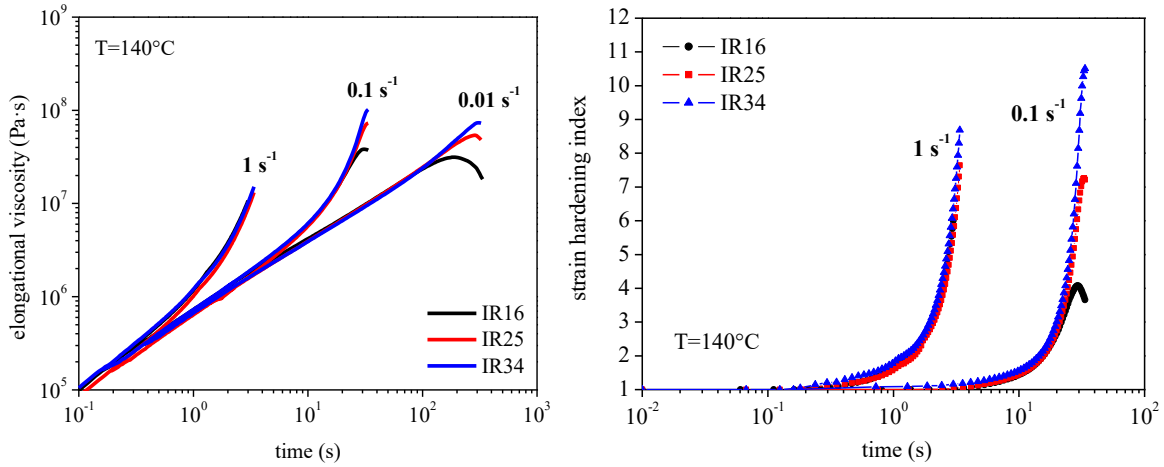

Figure 7. 19: *Elongational viscosity and strain hardening index at 140°C. Elongational strain rates of 1, 0.1 and 0.01 s^{-1}. Sample IR34 shows, as expected from the theory, the highest elongational viscosity, then the sample IR25 follows and last comes IR16.*

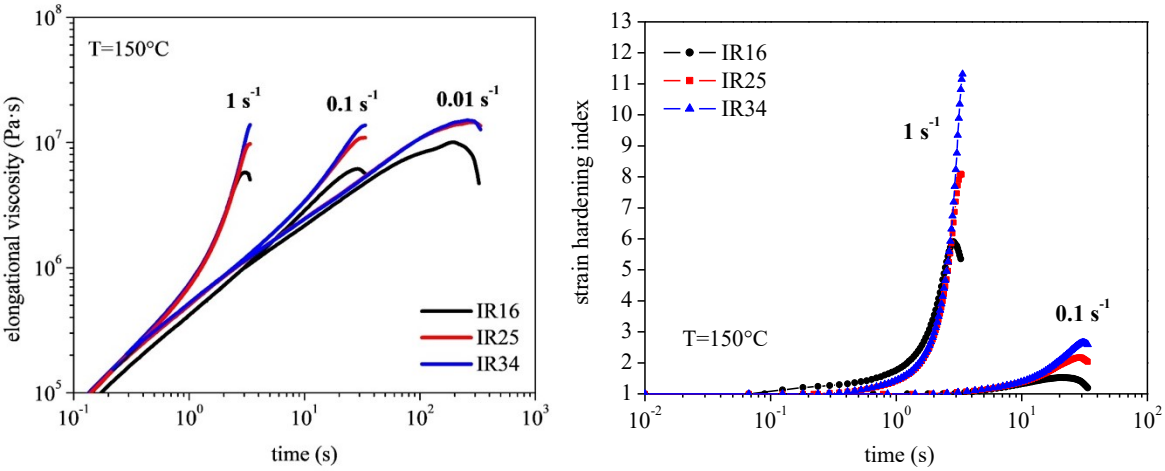

Figure 7. 20: *Elongational viscosity and strain hardening index at 150°C. Elongational strain rates of 1, 0.1 and 0.01 s^{-1}. Sample IR34 shows, as expected from the theory, the highest elongational viscosity, then the sample IR25 follows and last comes IR16.*

7.6 Injection molding conditions

To investigate the variation of gloss with molding conditions, as well as the dependence of gloss with the swelling index, a set of nine conditions to create the so-called gloss curves was investigated. Initially in the Research and Development (R&D)

laboratory it was possible to carry out this work. Since slightly unexpected results in this lab were obtained, the collaboration with the Quality Control (QC) laboratory became helpful. In this chapter both the R&D and the QC conditions will be presented. Although equipped with completely different molding machines and even if gloss is highly sensible to molding conditions, this comparison has proven to be useful to understand many aspects that were still unknown in the company at that time.

7.6.1 R&D conditions

As mentioned, it was decided to inject the three ABS at study in various conditions to investigate not only how gloss varies with the swelling index IR, but also how gloss is affected by these ones. The melt temperature was set at 220°C. For each sample, the flow front speed and the mold temperature have been varied. The flow front speed represents the melt speed in the cross-section of the mold cavity, hypothetically considering that the melt proceeds with a flat front. Three nominal values for the flow front speed were chosen: 100 mm/s, 200 mm/s and 300 mm/s. The mold temperature was set at 30°C, 45°C and 60°C. In this way, nine different conditions were investigated for gloss evaluation. In Table 7.2 the filling conditions are summarized. The imposed velocity is the value that is set on the screw of the extruder of the molding machine to obtain the desired nominal flow front speed. The apparent value of the shear rate was calculated as the ratio between the filling flow rate Q and the filling section wt^2, as defined in equation (7.5).

$$\dot{\gamma} = \frac{6Q}{wt^2} \tag{7.5}$$

Table 7. 2: *R&D set of molding conditions. Each filling condition has been done for the three mold temperatures.*

Imposed velocity (mm/s)	Width (mm)	Thickness (mm)	Filling section (mm^2)	Flow front velocity (mm/s)	Filling flow rate Q (ccm/s)	Shear rate (s^{-1})
34	60	2.9	180	95.9	16.7	198
74	60	2.9	180	208.8	36.3	432
110	60	2.9	180	310.3	54.0	642

Figure 7.21 is a picture of a R&D molded specimen.

Figure 7. 21: *R&D molded specimen.*

The first ten specimens have been rejected, while the subsequent five have been held for gloss evaluation.

7.6.2 QC conditions

The QC lab, for the standard gloss evaluation, adopts particular and specific molding conditions: an increasing volumetric flow rate over time, a mold temperature of 35°C and a melt temperature of 220°C. In particular, the volumetric flow rate varies from 30 cm^3/s to 50 cm^3/s. In Table 7.3 the QC standard molding parameters are summarized. The first ten specimens have been rejected, while the subsequent ten have been held for gloss evaluation.

Table 7. 3: *QC standard molding conditions for gloss evaluation.*

Imp.vol. flow rate (cm^3/s)		Width (mm)	Thickness (mm)	Flow front vel. (mm/s)	Filling section (mm^2)	Shear rate (s^{-1})
Min	30	80	3	125	240	250.0
Max	50	80	3	208.3	240	416.7
Average	40	80	3	166.7	240	333.3

It is possible to see from Table 7.3 that the strain rate is increased over time. Afterwards, to try to make a reasonable and reliable comparison, although the two labs operate with a different equipment, it was decided to reproduce, only for T_{mold}=30°C, the same filling conditions, in terms of shear rate, of the R&D lab. So, starting from the shear rates values involved in the R&D lab tests, by means of equation (7.5), the volumetric flow rates to be imposed were calculated. Table 7.4 reports the new conditions adopted in the QC lab.

Table 7. 4: *Conditions used at QC lab to replicate filling condition, in terms of shear rates, of the R&D lab.*

T_{mold}	Imp.vol. flow rate (cm^3/s)	Filling section (mm^2)	Flow front vel. (mm/s)	Shear rate (s^{-1})
30°C	24	240	100.0	200.0
	52	240	216.7	433.3
	77	240	320.8	641.7

It should be stressed here also that it is not easy to convince a QC lab to explore different conditions for fundamental investigations like the one here taken into account. This is the reason why the first set of tests were done in the R&D lab.

Figure 7. 22: *QC molded specimen.*

Figure 7.22 is a picture of a QC molded specimen. Ten specimens have been rejected while the subsequent eight were used for gloss evaluation.

7.7 Gloss evaluation

The standard *ASTM D523-14 – Standard Test Methods for Specular* Gloss suggests to use the 20° geometry for materials with high gloss, the 60° for values more than 70.[42] Gloss has been measured at the centre of the specimen for each sample and each condition, then the mean was taken into account to obtain average values. The value at 20° was considered because the type of ABS at study is a high gloss polymer. The following tables show the results obtained for R&D specimens. The expected trend of an increase in gloss by increasing the mold temperature and flow front speed is confirmed by the values obtained as shown in Figures 7.23, 7.24 and 7.25.

Table 7. 5: *Values of gloss at 20° for sample IR16 measured on R&D specimens.*

R&D – IR16 – Values of Gloss 20°								
		Specimen						
T_{mold} (°C)	Flow speed (mm/s)	1	2	3	4	5	Av. Value [GU]	S.d.
30	100	41.4	47.8	47.4	47.1	47.9	46.3	2.77
	200	65.4	67.0	67.3	66.9	66.1	66.5	0.78
	300	69.4	73.4	72.3	73.1	72.0	72.0	1.58
45	100	61.2	62.3	60.5	62.1	63.1	61.8	1.01
	200	80.2	80.4	79.9	82.3	81.5	80.9	1.01
	300	84.4	86.2	85.0	85.3	85.2	85.2	0.65
60	100	78.5	81.4	80.9	81.1	80.5	80.5	1.15
	200	91.7	93.5	93.4	93.5	92.6	92.9	0.79
	300	95.3	94.5	95.0	948	94.5	94.8	0.34

Table 7. 6: *Values of gloss at 20° for sample IR25 measured on R&D specimens.*

R&D – IR25 – Values of Gloss 20°								
		Specimen						
T_{mold} (°C)	Flow speed (mm/s)	1	2	3	4	5	Av. value [GU]	S.d.
30	100	53.3	54.8	55.2	55.3	55.1	54.7	0.83
	200	65.8	71.9	71.2	72.6	71.5	70.6	2.73
	300	73.6	75.7	74.9	76.3	76.1	75.3	1.10
45	100	67.7	67.6	62.7	60.9	68.9	65.6	3.53
	200	82.9	84.0	84.6	84.7	84.6	84.2	0.76
	300	95.5	96.3	96.4	95.7	95.9	96.0	0.38
60	100	86.5	85.0	86.2	86.5	84.8	85.8	0.83
	200	92.4	92.9	92.7	92.3	94.1	92.9	0.72
	300	95.5	96.3	96.4	95.7	95.9	96.0	0.38

Table 7. 7: *Values of gloss at 20° for sample IR34 measured on R&D specimens.*

R&D – IR34 – Values of Gloss 20°								
		Specimen						
T_{mold} (°C)	Flow speed (mm/s)	1	2	3	4	5	Av. value [GU]	S.d.
30	100	28.4	28.1	28.8	27.1	29.9	28.5	1.02
	200	48.0	49.4	49.5	50.9	49.3	49.4	1.03
	300	55.5	55.1	56.2	56.1	57.7	56.1	0.99
45	100	43.9	46.0	43.8	42.3	43.6	43.9	1.33
	200	65.9	66.6	67.0	67.0	65.8	66.5	0.58
	300	67.9	73.5	73.3	72.0	71.2	71.6	2.26
60	100	57.2	67.2	66.2	67.3	68.3	65.2	4.56
	200	88.4	87.5	88.1	88.7	85.6	87.7	1.23
	300	86.7	88.0	89.0	87.9	87.6	87.8	0.83

However, an unexpected result was obtained and confirmed in each condition: sample IR25 has a similar or higher gloss value than sample IR16. Figure 7.26 shows the gloss value as function of shear rate, for the three samples, for the 30°C mold temperature. The slightly counter-trend result obtained at R&D lab is not attributable to the lower particle dimensions of sample IR25 compared to IR16 because the molding at QC always showed a lowered gloss value with increasing the swelling index.

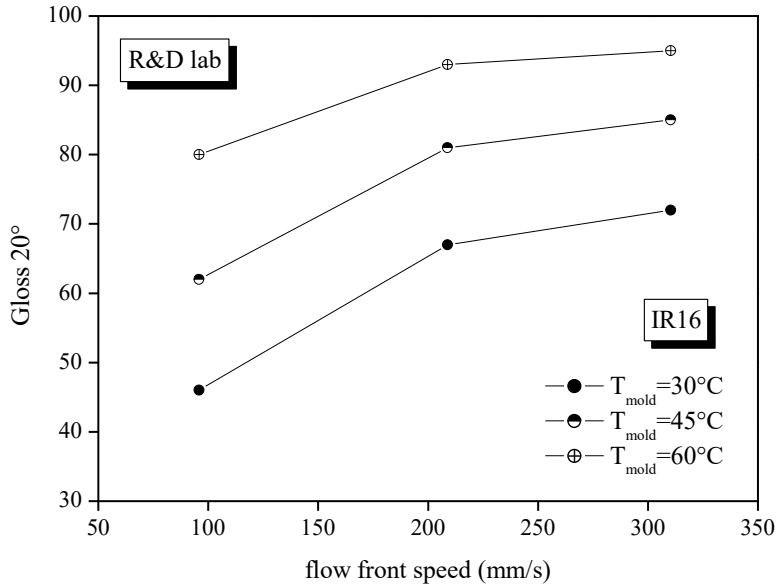

Figure 7. 23: *Gloss at 20° for sample IR16 vs. flow front speed, parametric in the mold temperature.*

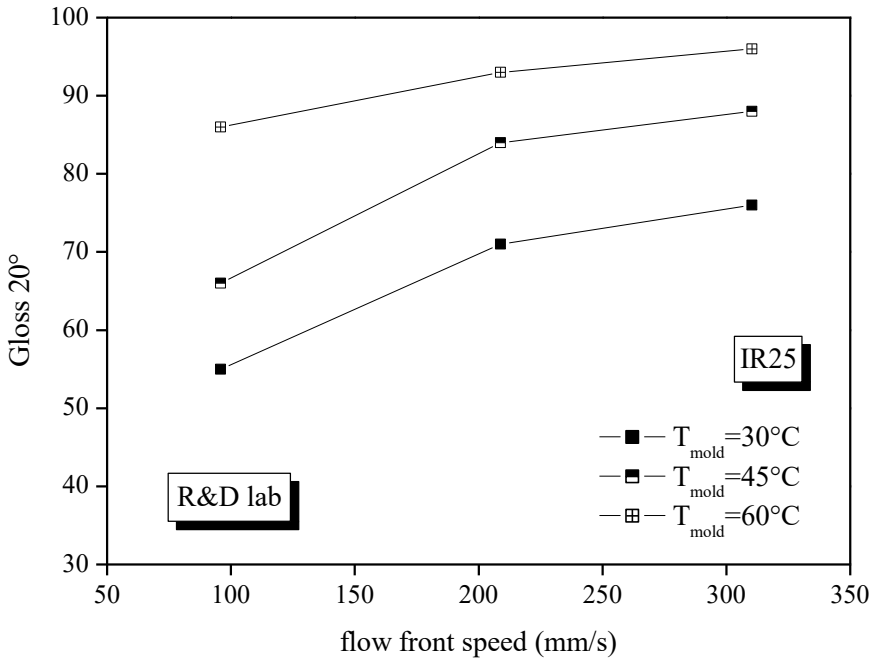

Figure 7. 24: *Gloss at 20° for sample IR25 vs flow front speed, parametric in the mold temperature.*

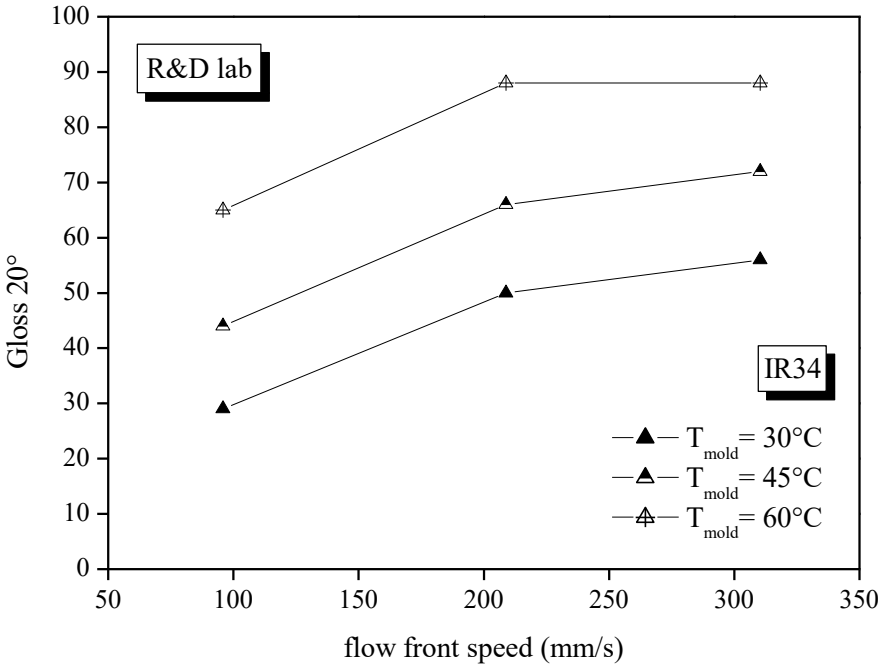

Figure 7. 25: *Gloss at 20° for sample IR34 vs flow front speed, parametric in the mold temperature.*

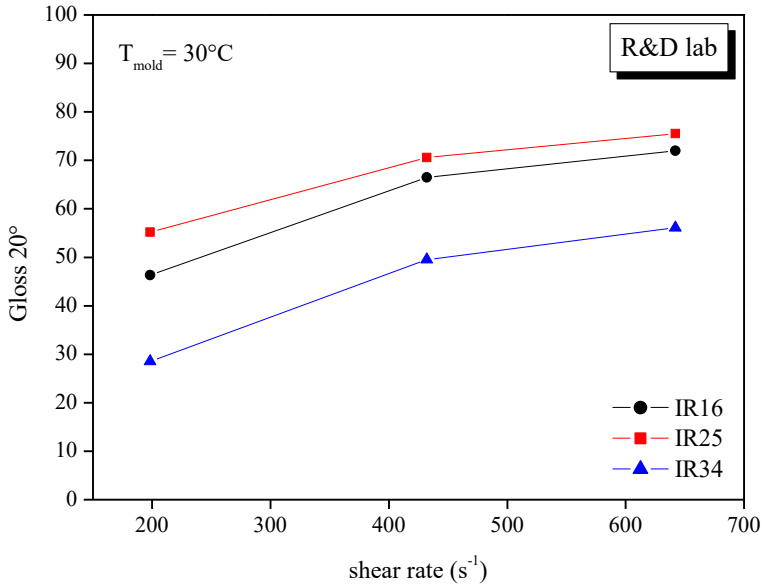

Figure 7. 26: *Gloss at 20° vs shear rate for T_{mold}=30°C. The expected trend of increasing* gloss *by decreasing the sweeling index is partially confirmed. Sample IR25 has a higher gloss than IR16.*

In the following tables gloss values obtained on specimens molded with QC standard conditions are presented.

Table 7. 8: *Values of gloss at 20° for sample IR16 measured on QC standard specimens.*

QC standard conditions – IR16 – Values of Gloss 20°											
Specimen											
1	2	3	4	5	6	7	8	9	10	Av. value [GU]	S.d.
47.4	30.8	47.6	47.1	47.9	47.6	45.0	47.8	48.0	46.8	45.6	5.27

Table 7. 9: *Values of gloss at 20° for sample IR25 measured on QC standard specimens.*

QC standard conditions – IR25 – Values of Gloss 20°											
Specimen											
1	2	3	4	5	6	7	8	9	10	Av. value [GU]	S.d.
36.0	32.3	33.4	25.3	21.7	30.1	31.9	33.3	34.5	34.8	31.3	4.52

Table 7. 10: *Values of gloss at 20° for sample IR34 measured on QC standard specimens.*

QC standard conditions – IR25 – Values of Gloss 20°											
Specimen											
1	2	3	4	5	6	7	8	9	10	Av. value [GU]	S.d.
13.5	11.7	12.2	10.2	10.2	10.2	9.6	9.6	10.6	9.8	10.8	1.29

As obtained in the preliminary result during the production sampling, QC has confirmed again that gloss decreases by increasing the swelling index, as shown in Figure 7.27. Furthermore, gloss measured on QC specimens is, for each sample, much lower than on R&D specimen.

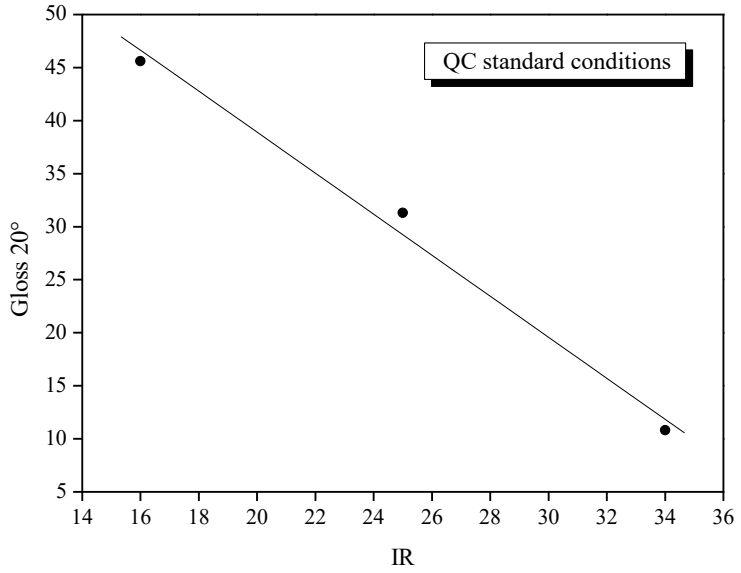

Figure 7. 27: *Gloss at 20° vs IR for QC standard conditions.*

The following tables show the results of QC molding with filling conditions that reproduce the same shear rates developed by R&D conditions.

Table 7. 11: *Values of gloss at 20° for sample IR16 measured on QC specimens.*

QC – IR16 – Values of Gloss 20°										
T_{mold}=30°C	**Specimen**									
Imp.vol. flow rate (cm^3/s)	**1**	**2**	**3**	**4**	**5**	**6**	**7**	**8**	**Av. value [GU]**	**S.d.**
24	26.5	34.5	35.0	34.9	34.6	33.7	34.9	35.4	33.7	2.76
52	50.7	52.6	53.3	54.8	51.6	52.8	53.0	51.4	52.5	1.20
77	63.6	62.3	62.2	62.5	62.1	59.7	58.8	59.9	61.4	1.58

Table 7. 12: *Values of gloss at 20° for sample IR25 measured on QC specimens.*

QC – IR25 – Values of Gloss 20°										
T_{mold}=30°C	Specimen									
Imp.vol. flow rate (cm^3/s)	1	2	3	4	5	6	7	8	Av. Value [GU]	S.d.
24	25.4	25.1	26.0	26.8	28.6	29.0	30.0	31.2	27.8	2.11
52	31.0	28.7	26.6	30.7	33.9	30.2	25.2	33.3	30.0	2.83
77	39.0	43.0	39.1	39.9	40.1	47.9	47.7	43.8	42.6	3.44

Table 7. 13: *Values of gloss at 20° for sample IR34 measured on QC specimens.*

QC – IR34 – Values of Gloss 20°										
T_{mold}=30°C	Specimen									
Imp.vol. flow rate (cm^3/s)	1	2	3	4	5	6	7	8	Av. value [GU]	S.d.
24	7.6	8.2	7.8	7.7	8.4	8.1	8.1	8.3	8.0	0.27
52	8.9	9.1	9.2	10.2	10.5	14.8	12.4	**	10.7	2.0
77	10.7	10.0	9.5	11.6	10.3	10.6	10.2	10.1	10.4	0.58
** specimen excluded because not evaluable										

Figure 7.28 shows the trend of gloss as function of shear rate for samples molded at the QC lab.

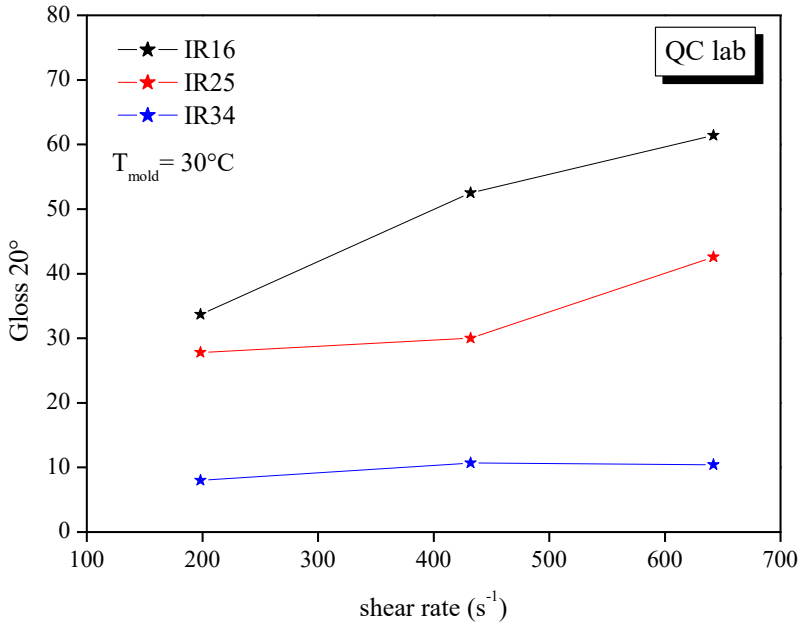

Figure 7. 28: *Gloss at 20° vs shear rate for samples molded in the QC lab.*

It is possible to note that even replicating the R&D conditions, QC always obtained a trend of increasing gloss by decreasing the swelling index value. Another consideration is that the sensibility of gloss to the increase in shear rate is different for the two laboratories. In fact, R&D produces more or less the same growing trend of gloss by increasing the the shear rate for all samples, while for QC lab the trend is different. In fact, considering sample IR16 molded at QC lab, the gloss value is significantly increased with the shear rate. Sample IR25 improves the gloss value of around 10/15 [GU] both in R&D and QC labs, while the increase in shear rate seems to have only a very small effect, if there is any, for sample IR34. A possible explanation of this fact will be presented in §7.9. Gloss values at 60° and 85° for QC specimens are reported below for the sake of completeness.

Table 7. 14: *Values of gloss at 60° for sample IR16 measured on QC specimens.*

QC – IR16 – Values of Gloss 60°										
T_{mold}=30°C	**Specimen**									
Imp.vol. flow rate (cm^3/s)	**1**	**2**	**3**	**4**	**5**	**6**	**7**	**8**	**Av. value [GU]**	**S.d.**
24	58.7	72.8	73.9	72.6	73.0	72.7	71.9	73.3	71.1	5.05
52	81.7	81.8	82.8	83.8	81.0	82.6	82.5	81.3	82.2	0.91
77	86.6	86.9	86.4	86.0	88.1	86.8	86.5	85.8	86.6	0.70

Table 7. 15: *Values of gloss at 60° for sample IR25 measured on QC specimens.*

QC – IR25 – Values of Gloss 60°										
T_{mold}=30°C	**Specimen**									
Imp.vol. flow rate (cm^3/s)	**1**	**2**	**3**	**4**	**5**	**6**	**7**	**8**	**Av. value [GU]**	**S.d.**
24	62.8	61.4	63.0	63.8	64.3	67.0	67.5	67.8	64.7	2.42
52	59.0	66.4	64.0	65.8	66.3	66.7	63.1	68.6	65.0	2.95
77	69.0	74.8	72.5	74.0	71.8	79.0	75.4	71.5	73.5	3.02

Table 7. 16: *Values of gloss at 60° for sample IR34 measured on QC specimens.*

QC – IR34 – Values of Gloss 60°										
T_{mold}=30°C	**Specimen**									
Imp.vol. flow rate (cm^3/s)	**1**	**2**	**3**	**4**	**5**	**6**	**7**	**8**	**Av. value [GU]**	**S.d.**
24	27.3	26.2	24.5	31.3	31.7	28.2	34.1	30.6	29.2	3.21
52	30.7	31.8	33.2	34.5	35.8	42.7	42.4	**	35.9	4.86
77	32.4	33.1	35.2	36.3	33.6	31.1	31.6	31.4	33.1	1.87
** specimen excluded because not evaluable										

Table 7. 17: *Values of gloss at 85° for sample IR16 measured on QC specimens.*

QC – IR16 – Values of Gloss 85°										
T_{mold}=30°C	Specimen									
Imp.vol. flow rate (cm^3/s)	1	2	3	4	5	6	7	8	Av. Value [GU]	S.d.
24	93.6	95.6	96.9	96.9	96.9	94.5	96.2	96.9	95.9	1.28
52	98.4	98.1	97.7	93.3	97.8	98.5	98.5	98.4	97.6	1.76
77	98.3	98.6	97.7	98.8	98.9	98.7	98.7	98.8	98.6	0.39

Table 7. 18: *Values of gloss at 85° for sample IR25 measured on QC specimens.*

QC – IR25 – Values of Gloss 85°										
T_{mold}=30°C	Specimen									
Imp.vol. flow rate (cm^3/s)	1	2	3	4	5	6	7	8	Av. Value [GU]	S.d.
24	95.1	94.9	95.4	95.4	95.7	96.3	96.2	96.2	95.7	0.54
52	92.5	95.8	96.3	96.1	95.7	96.4	95.7	97.0	95.7	1.36
77	95.5	97.9	97.6	97.9	96.7	97.8	98.0	97.8	97.4	0.87

Table 7. 19: *Values of gloss at 85° for sample IR34 measured on QC specimens.*

QC – IR34 – Values of Gloss 85°										
T_{mold}=30°C	Specimen									
Imp.vol. flow rate (cm^3/s)	1	2	3	4	5	6	7	8	Av. value [GU]	S.d.
24	87.2	86.0	84.5	89.2	88.9	87.9	90.5	88.9	87.9	1.93
52	90.7	90.1	91.0	89.6	92.3	92.7	93.3	**	91.4	1.40
77	87.7	90.3	91.5	91.6	91.4	89.4	90.4	91.0	90.4	1.33
** specimen excluded because not evaluable										

This data will be considered in §7.9 for the gloss-roughness correlation study, in which the different gloss evaluation angles will be included.

7.8 Surface roughness evaluation

The roughness had been measured on the five samples molded at R&D, and on the eight samples, for both QC standard conditions and QC conditions reproducing R&D shear rates. The parameters considered were R_a, R_q and RS_m defined as follows:

- R_a is the arithmetic mean of the profile deviation from the mean line z=0:

$$R_a = \frac{1}{l}\int_0^l |z(x)|dx \tag{7. 6}$$

- R_q is the root mean square profile deviation from the mean line z=0:

$$R_q = \sqrt{\frac{1}{l}\int_0^l z(x)^2 dx} \tag{7. 7}$$

- RS_m is the mean spacing between the asperities, calculated as follows:

$$RS_m = \frac{L}{RP_c} \tag{7. 8}$$

with L=sampling length and RP_c peaks count.

It has been decided to evaluate the roughness to investigate, qualitatively and quantitatively, how is it correlated with gloss. Since both R&D and QC specimens showed the gloss transition at the end of the plaque, the first target of roughness measures had been measuring R_a and RS_m, both in middle and at the end of the specimens. The following figures have been obtained photographing QC specimens, for the condition of maximum shear rate, under an optical microscope to highlight the difference of gloss at the end of the plaque. It is possible to see that the area involved in gloss transition is higher for sample IR34, and this is valid in each condition. The hypothesis is that since particles of IR34 are subjected to higher deformation and orientation, the result is that, for all conditions the same, IR34 retains more the induced orientation state, in comparison to IR16 and IR25. Furthermore, gloss transition decreases by increasing the mold temperature, because the polymer has more time to relax the induced orientation and to replicate the mold.

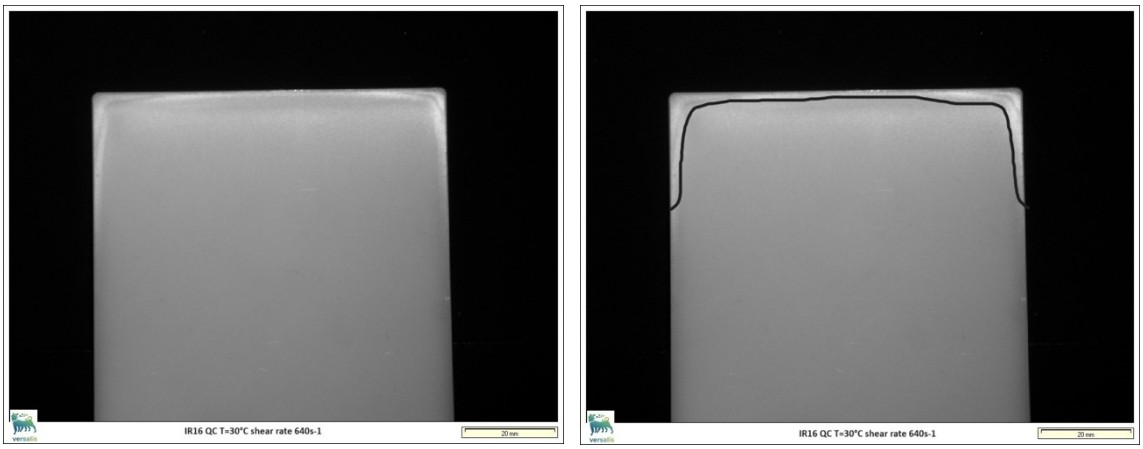

Figure 7. 29: *Gloss transition at the end of the QC specimen IR16.*

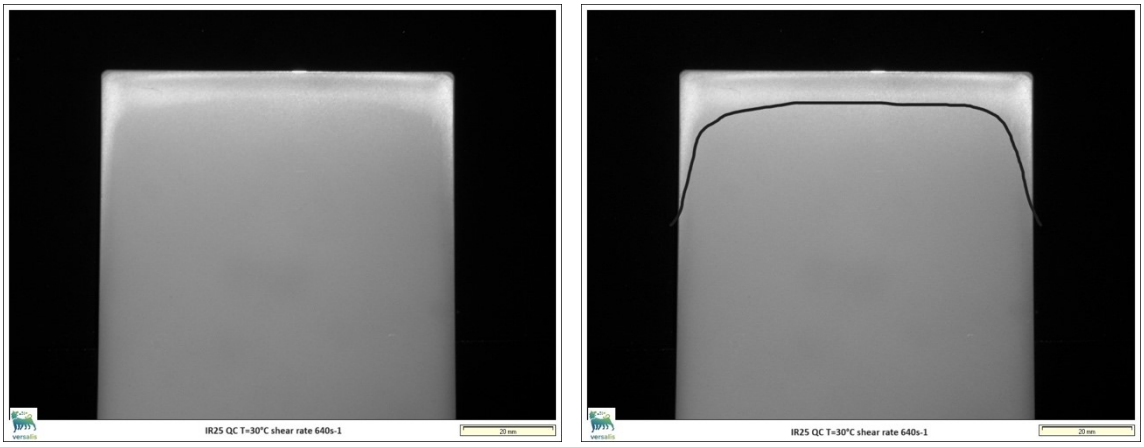

Figure 7. 30: *Gloss transition at the end of the QC specimen IR25.*

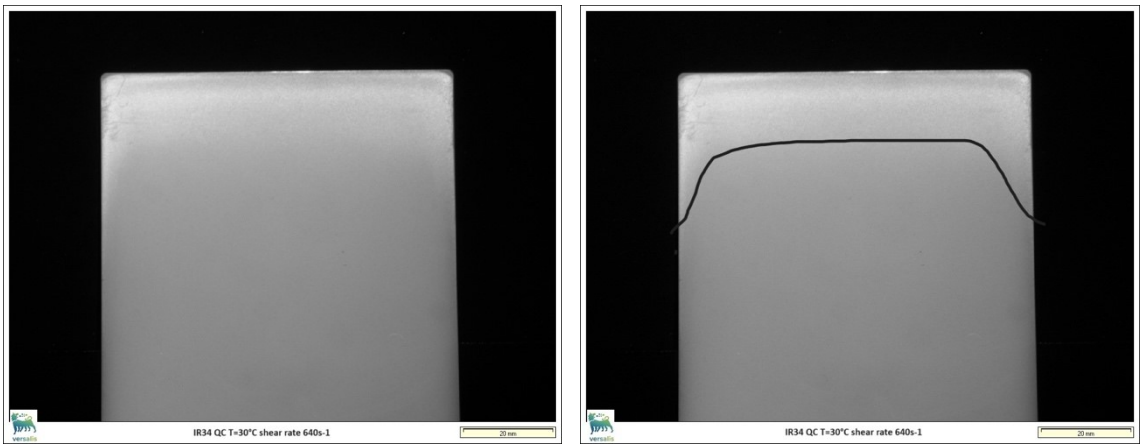

Figure 7. 31: *Gloss transition at the end of the QC specimen IR34.*

The following tables show the results of roughness measures for R&D specimens. As it will be shown in §7.13, simulations of the mold filling at QC and R&D labs, have been performed, although with some approximations. These showed a lower pressure at the end of the plaque, as also expected from the theory, for which the melt pressure increases by increasing the contact length, as shown in Figure 5.5. Then the gloss transition at the end of the plaque is due to the decreasing pressure profile in the flow direction.

Table 7. 20: *Average values of R_a and RS_m at the centre and the end of R&D specimens IR16.*

R&D conditions – IR16 – Average values of R_a and RS_m at the centre and at the edge of the plaque									
T_{mold} (°C)	**Flow front speed (mm/s)**	**Average value R_a [µm]**				**Average value RS_m [µm]**			
		centre	**S.d.**	**edge**	**S.d**	**centre**	**S.d**	**edge**	**S.d**
30	100	0.048	0.004	0.070	0.014	42.86	5.345	43.90	8.234
	200	0.034	0.005	0.044	0.005	54.84	14.23	37.08	4.227
	300	0.030	0.000	0.044	0.005	45.34	6.794	31.94	5.871
45	100	0.036	0.005	0.054	0.009	55.62	9.817	46.18	12.345
	200	0.030	0.000	0.044	0.009	68.62	17.52	33.16	5.137
	300	0.032	0.004	0.044	0.005	76.04	40.99	33.02	5.175
60	100	0.032	0.004	0.044	0.005	59.96	14.69	31.70	4.024
	200	0.034	0.009	0.036	0.005	69.80	7.879	42.54	17.47
	300	0.030	0.000	0.038	0.004	74.28	15.24	40.88	12.12

Table 7. 21: *Average values of R_a and RS_m at the centre and the end of R&D specimens IR25.*

R&D conditions – IR25 – Average values of R_a and RS_m at the centre and at the edge of the plaque									
T_{mold} (°C)	**Flow front speed (mm/s)**	**Average value R_a [µm]**				**Average value RS_m [µm]**			
		centre	**S.d.**	**edge**	**S.d.**	**centre**	**S.d.**	**edge**	**S.d.**
30	100	0.042	0.004	0.052	0.004	62.20	12.15	43.32	9.881
	200	0.030	0.000	0.046	0.009	67.28	13.47	36.56	8.652
	300	0.030	0.000	0.048	0.004	70.26	8.806	37.42	13.55
45	100	0.032	0.004	0.048	0.008	68.30	11.01	43.82	4.194
	200	0.028	0.004	0.040	0.000	77.80	16.16	35.64	5.064
	300	0.028	0.004	0.038	0.004	71.26	15.38	35.18	4.033
60	100	0.030	0.007	0.038	0.004	70.06	20.49	35.58	4.746
	200	0.030	0.007	0.040	0.000	81.96	40.80	35.28	4.493
	300	0.024	0.005	0.042	0.004	71.06	18.36	28.78	4.765

Table 7. 22: *Average values of R_a and RS_m at the centre and the end of R&D specimens IR34.*

R&D conditions – IR34 – Average values of R_a and RS_m at the centre and at the edge of the plaque									
T_{mold} (°C)	**Flow front speed (mm/s)**	**Average value R_a [µm]**				**Average value RS_m [µm]**			
		centre	**S.d.**	**edge**	**S.d.**	**centre**	**S.d.**	**edge**	**S.d.**
30	100	0.054	0.005	0.072	0.011	36.74	4.175	33.84	3.694
	200	0.040	0.000	0.060	0.007	32.96	3.329	26.04	2.388
	300	0.040	0.000	0.060	0.000	33.94	4.863	22.12	1.052
45	100	0.048	0.008	0.060	0.000	45.40	9.056	29.72	2.801
	200	0.032	0.004	0.058	0.004	47.94	8.908	21.22	1.291
	300	0.030	0.000	0.056	0.005	52.98	13.24	21.02	2.190
60	100	0.034	0.005	0.054	0.009	45.82	8.801	34.52	5.943
	200	0.034	0.009	0.054	0.005	57.98	11.01	24.54	4.658
	300	0.030	0.000	0.058	0.004	62.30	18.07	21.54	0.907

As it is possible to see, both R_a and RS_m vary from the centre to the edge, in particular R_a increases and RS_m decreases. This is a first clue that what it is seen with the naked eye, reflects the nature of the surface at microscopic level. In fact, at the edge, the opaque area is justified with a more wrinkled surface (higher and closer peaks). The same measures have been done on QC standard specimens. The following tables shows the results.

Table 7. 23: *Average values of R_a and RS_m at the centre and the end of the standard QC specimens IR16.*

QC standard conditions – IR16 – Average values of R_a and RS_m							
Average value R_a [µm]				**Average value RS_m [µm]**			
centre	**S.d.**	**edge**	**S.d.**	**centre**	**S.d.**	**edge**	**S.d.**
0.040	0.007	0.050	0.007	38.50	5.663	36.20	3.89

Table 7. 24: *Average values of R_a and RS_m at the centre and the end of the standard QC specimens IR25.*

QC standard conditions – IR25 – Average values of R_a and RS_m							
Average value R_a [µm]				**Average value RS_m [µm]**			
centre	**S.d.**	**edge**	**S.d.**	**centre**	**S.d.**	**edge**	**S.d.**
0.060	0.007	0.060	0.007	30.20	2,045	29.00	4.391

Table 7. 25: *Average values of R_a and RS_m at the centre and the end of the standard QC specimens IR34.*

QC standard conditions – IR34 – Average values of R_a and RS_m							
Average value R_a [µm]				**Average value RS_m [µm]**			
centre	**S.d.**	**edge**	**S.d.**	**centre**	**S.d.**	**edge**	**S.d.**
0.090	0.007	0.100	0.005	24.70	2.518	24.20	4.489

In QC specimens, R_a and RS_m vary less than R&D, this is probably because QC standard conditions are not favorable for gloss enhancement and so the gloss transition is less evident. However, QC specimens are rougher, in terms of higher R_a and lower RS_m, also justifying the lower gloss. Successively, it was decided to study, in more detail, the correlation between gloss and roughness. Specimens molded at R&D lab at 30°C and specimens, reproducing the same conditions, molded at QC lab, have been used to evaluate these parameters. Since the Simonsen's model suggest that the root-mean square roughness is correlated with gloss, it was considered the R_q values at the centre of the plaque, where is measured also gloss. The following tables reports the results obtained. The measuring unit is µm.

Table 7. 26: *Values of R_q of sample IR16 molded at R&D lab.*

R&D – IR16 – Values of R_q								
T_{mold} (°C)	**Flow front speed (mm/s)**	**Specimen**					**Av. value [µm]**	**S.d.**
		1	**2**	**3**	**4**	**5**		
30	100	0.06	0.05	0.07	0.06	0.06	0.06	0.007
	200	0.04	0.05	0.04	0.06	0.04	0.05	0.009
	300	0.04	0.04	0.04	0.05	0.04	0.04	0.004

Table 7. 27: *Values of R_q of sample IR25 molded at R&D lab.*

R&D – IR25 – Values of R_q								
T_{mold} (°C)	**Flow front speed (mm/s)**	**Specimen**					**Av. value [µm]**	**S.d.**
		1	**2**	**3**	**4**	**5**		
30	100	0.04	0.05	0.05	0.07	0.05	0.05	0.011
	200	0.04	0.04	0.04	0.04	0.05	0.04	0.004
	300	0.04	0.03	0.04	0.04	0.03	0.04	0.005

Table 7. 28: *Values of R_q of sample IR34 molded at R&D lab.*

R&D – IR34 – Values of R_q								
T_{mold} (°C)	**Flow front speed (mm/s)**	**Specimen**					**Av. value [µm]]**	**S.d.**
		1	**2**	**3**	**4**	**5**		
30	100	0.07	0.07	0.05	0.08	0.07	0.07	0.011
	200	0.03	0.05	0.05	0.06	0.05	0.05	0.011
	300	0.04	0.05	0.05	0.05	0.03	0.04	0.009

Table 7. 29: *Values of R_q of sample IR16 molded at QC lab.*

QC – IR16 – Values of R_q										
T_{mold}=30°C	Specimen									
Imp.vol. flow rate (ccm/s)	1	2	3	4	5	6	7	8	Av. value [µm]	S.d.
24	0.14	0.05	0.08	0.12	0.07	0.07	0.07	0.07	0.08	0.030
52	0.05	0.05	0.05	0.05	0.05	0.06	0.05	0.05	0.05	0.004
77	0.05	0.05	0.05	0.05	0.05	0.04	0.05	0.05	0.05	0.004

Table 7. 30: *Values of R_q of sample IR25 molded at R&D lab.*

QC – IR25 – Values of R_q										
T_{mold}=30°C	Specimen									
Imp.vol. flow rate (ccm/s)	1	2	3	4	5	6	7	8	Av. value [µm]	S.d.
24	0.08	0.09	0.10	0.59	0.09	0.08	0.08	0.08	0.15	0.178
52	0.10	0.07	0.07	0.07	0.07	0.07	0.08	0.07	0.08	0.011
77	0.07	0.06	0.07	0.06	0.06	0.06	0.06	0.06	0.06	0.005

Table 7. 31: *Values of R_q of sample IR34 molded at R&D lab.*

QC – IR34 – Values of R_q										
T_{mold}=30°C	Specimen									
Imp.vol. flow rate (ccm/s)	1	2	3	4	5	6	7	8	Av. value [µm]	S.d.
24	0.16	0.57	0.17	0.18	0.15	0.17	0.16	0.16	0.22	0.144
52	0.13	0.12	0.22	0.12	0.12	0.09	0.11	**	0.13	0.042
77	0.15	0.14	0.12	0.12	0.12	0.15	0.15	0.11	0.13	0.017
** specimen excluded because not evaluable										

Data shows higher values of R_q for QC specimens. Furthermore, QC lab produces a wider range of roughness.

7.9 Correlation between gloss and roughness

As mentioned before, the R_q value is correlated to surface gloss. To obtain the fitting functions, the Simonsen's model has been used. As glossmeter wavelength the value of 550 nm was considered, because this is the middle value of the visible wavelengths. The

detector collection angle was 2.5°. In this way each parameter, except the correlation length, required for the model was available. The correlation length was used left as free parameter for fitting the experimental data. Figure 7.32 reports the gloss values versus roughness for QC specimens. The three continuous curves have been obtained by fitting experimental points and they represent the three angles of evaluating gloss (20°,60° and 85°). A correlation length equal to 1600 nm proved effective in fitting each set of points. Three observations are worth mentioning:

- sample IR16 shows higher values of gloss justified by lower roughness, as well as a lower span in R_q values;
- considering a single curve, sample IR34 produces a wider range of roughness, maintaining an almost unchanged gloss for different molding conditions;
- the plot shows the reason why glossy materials are evaluated at 20° rather than 60° or 85°. In fact, increasing the evaluating angle gloss rapidly increases and it is no longer possible to appreciate the differences in high gloss samples.

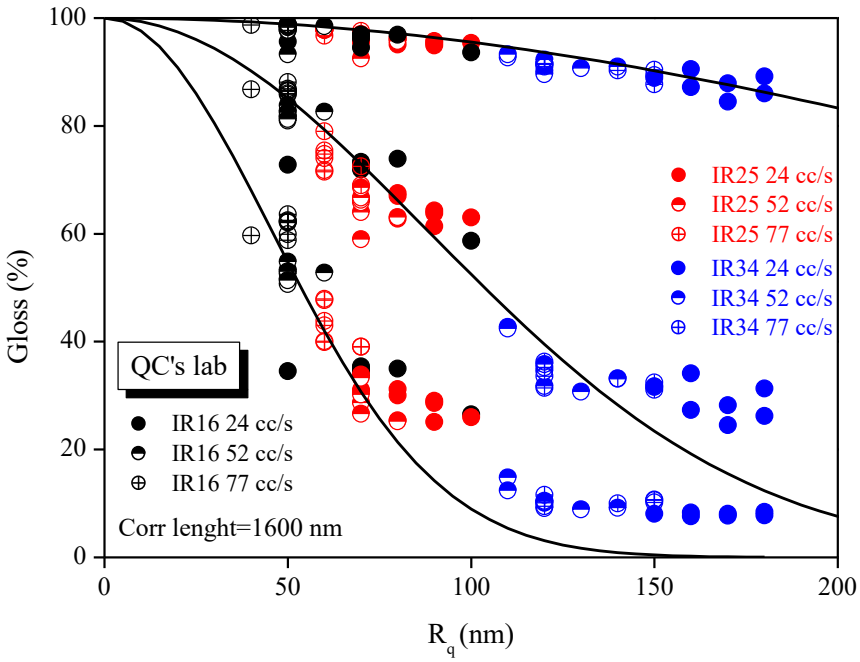

Figure 7. 32: *Gloss vs. roughness correlation. R_q is the root-mean-square roughness. Each point represents the gloss and the R_q evaluated for each sample. The three curves represent the three evaluating gloss angles (20°, 60° and 85°). The correlation length has been used as fitting parameter for the experimental points.*

Considering Figure 7.28, representing the trend of gloss with increasing volumetric flow rate and the Figure 7.32, the following considerations can be made. The flow injection speed acts in opposite ways: on the one hand by increasing this speed, the pressure, and then the replication factor, increases, on the other hand it leads to a higher orientation on the surface. Probably a balance between the two contribution that could explain the differences, under the same molding conditions, between the samples. Looking at the roughness values of sample IR34, it is possible to say that points of intermediate flow rate (52 cm^3/s), are on average more shifted toward lower roughness values compared to the high flow rate (77 cm^3/s). The reason could be due to the fact that with increasing the flow rate the pressure increases but with that also the surface orientation, whose relaxation leads to a more wrinkled morphology. In fact, for sample IR34, which have more deformable and consequently more oriented particles, the increase in flow rate does not result in an increase of gloss. For samples IR25 and IR16, the same principle applies, but since they have lower deformability of the particles, the increase in flow rate causes an increase in pressure rather than a higher orientation. In this way they show higher gloss justified by lower roughness values.

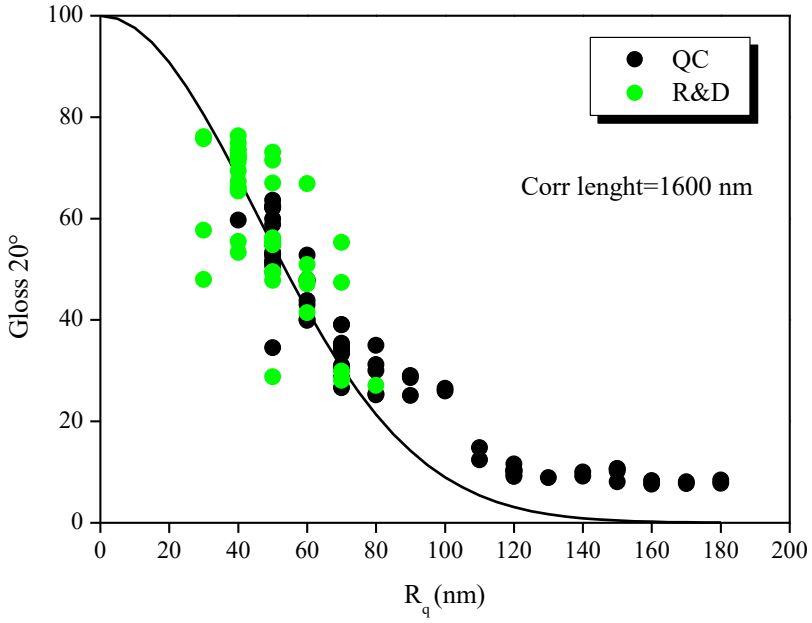

Figure 7. 33: *Correlation between gloss at 20° and R_q for both R&D and QC specimens. R&D produces lower and narrow range of roughness compared to QC.*

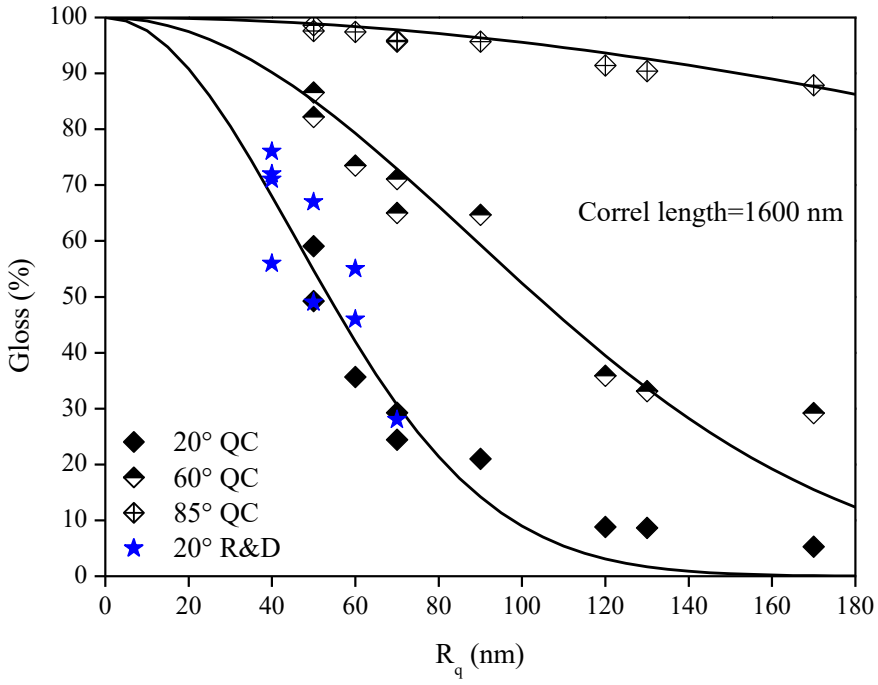

Figure 7. 34: *Gloss-roughness correlation. In this case each point represents the average values for each condition for each sample.*

Figure 7.33 shows the correlation between the gloss value measured at 20° and roughness, for both R&D and QC specimens. For practical reasons, only the gloss evaluation at 20° for R&D specimens has been done. This graph has the aim of highlighting the differences between the two labs. It is evident that, although the same molding conditions were set as similar as possible, the two labs produce specimens with different roughness and consequently with different gloss. QC produces rougher specimens than R&D lab. Furthermore, samples molded at QC lab show a wider range of roughness compared with R&D. The average values of gloss versus roughness are shown in Figure 7.34.

7.10 The rubber modification during injection molding

Given the differences of results from the two laboratories, the doubt arose that the molding process could somehow affect the cross-linking degree of the rubbery phase. To investigate if this was the case the swelling index on molded specimens was measured. The condition of T=30°C and flow injection speed of 200 mm/s for the R&D lab and the

standard condition for QC lab were chosen. The following table reports the IR values obtained using the standard internal method.

Table 7. 32: *Measure of the swelling index on molded specimens.*

Sample	Real IR	IR of R&D specimen (T=30°C, v=200mm/s)	IR of standard QC specimen (T=35°C, increasing flow rate)
IR16	18	15	18
IR25	28.5	20.5	21.5
IR34	32.5	24	27

The results confirmed that the process of injection molding altered the cross-linking degree of the rubber. Moreover, although the conditions are not properly the same, R&D changes more heavily the swelling index. This is not surprising since R&D lab, using an old injection molding machine with a less precise parameters control compared to the newer electric machine of the QC laboratory, leads to a greater polymer degradation. In any case, special attention, from a production point of view, should be paid to this aspect, especially with medium-high IR values.

7.11 Alternative measures of the swelling index

The traditional determination of the swelling index (IR) presents some problems. First of all, the long time and the high amount of solvent required for the analysis. In addition, for salami-like particles, also part of the matrix inside the rubbery phase contribute to the swelling, so the result is not only a consequence of the contribution of the rubber alone. Finally, smallest and highly-cross-linked particles tend to remain suspended and thus they don't contribute to the measure. Since the swelling index is strongly correlated with the capillary elastic number, and therefore with the elongational viscosity, an alternative method has been used to try to correlate these two parameters. Since it was demonstrated that injection-molded specimens possess a reduced IR value compared to the initial granules, it was decided to perform EVF tests at 150°C on specimens obtained from the compression molding at 190°C of pieces of the plates. Three elongational strain rates $\dot{\varepsilon}_H$ equal to 1 s^{-1}, 0.1 s^{-1} and 0.01 $s^{-1,}$ up to Hencky strain equal to

3.4 have been investigated. Figures 7.35, 7.36 and 7.37 show the comparison of elongational viscosities for ABS granules, R&D lab (T=30°C, v=200 mm/s) and QC lab standard specimens, for each sample. It is possible to see that for sample IR16 the elongational viscosity is similar to that of the granules, R&D and QC plaques. By increasing the swelling index, the differences between granules and molded specimens beginning to appear.

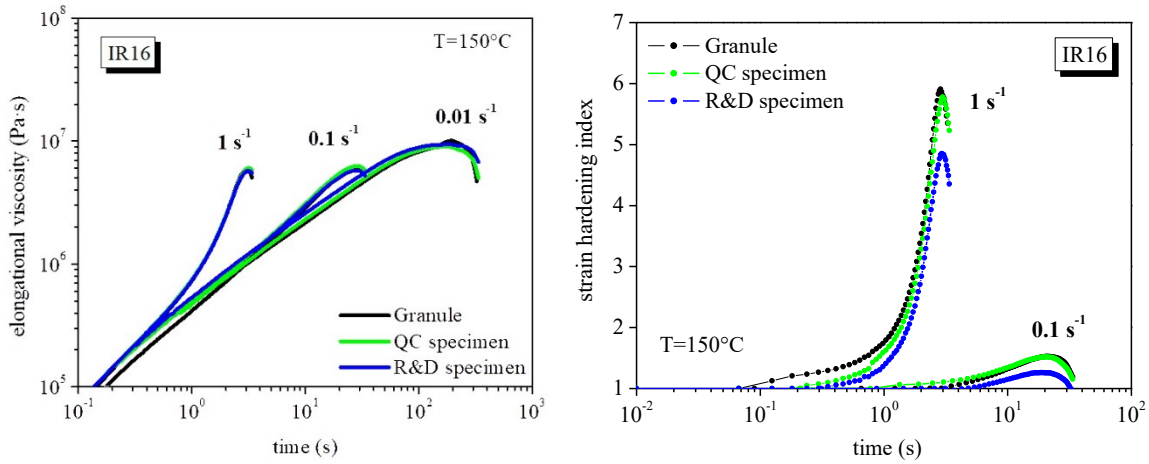

Figure 7. 35: *Elongational viscosity and strain hardening index of sample IR16 measured at 150°C by EVF tests. EVF specimens have been obtained from granules, QC and R&D specimens.*

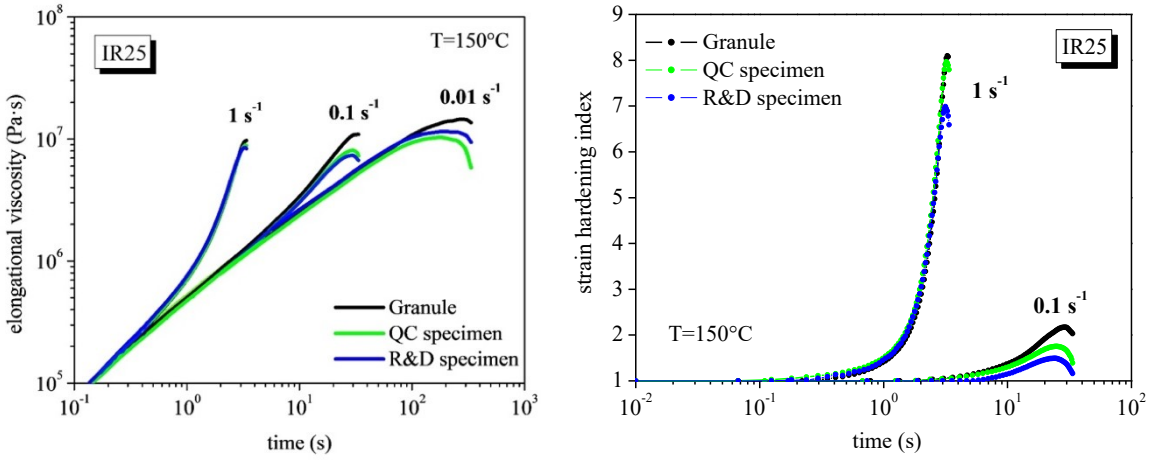

Figure 7. 36: *Elongational viscosity and strain hardening index of sample IR25 measured at 150°C by EVF tests. EVF specimens have been obtained from granules, QC and R&D specimens.*

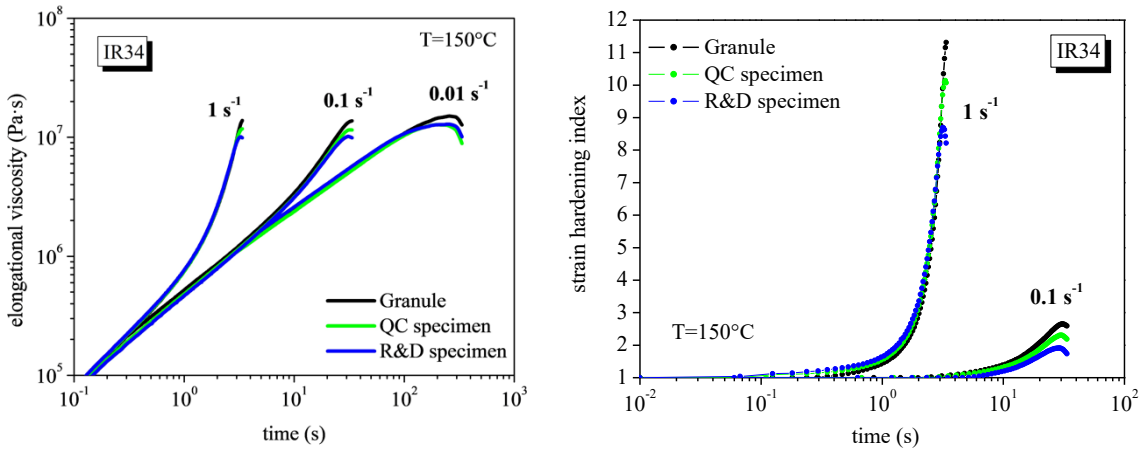

Figure 7. 37: *Elongational viscosity and strain hardening index of sample IR34 measured at 150°C by EVF tests. EVF specimens have been obtained from granules, QC and R&D specimens.*

Figure 7.38 shows the elongational viscosity linear values obtained for elongational strain rate equal to 0.1 s^{-1} and Hencky strain of 3.28 ("peak of the curve"). The data are plotted as a function of the ideal elongational viscosity linear trend obtained using the values of the granules (an ideal bisector line). The deviation from the original elongational viscosity value of the corresponding granules is thus immediately evident. The viscosity values of the granules obviously lie on the bisector of the graph, while molded specimens lie below due to their lower viscosity values. The fact that molded specimens exhibit a lower elongational viscosity confirms the results obtained with the measure of IR on plaques. As mentioned previously discussing the elongational viscosity of soft particles, this is lower for lower IR particles because of their lower deformability. In view of this promising results obtained with EVF tests, an attempt was made to see if this technique could somehow be able to indirectly measure the degree of crosslinking of the rubber particles and to prove a valuable alternative to the swelling index method.

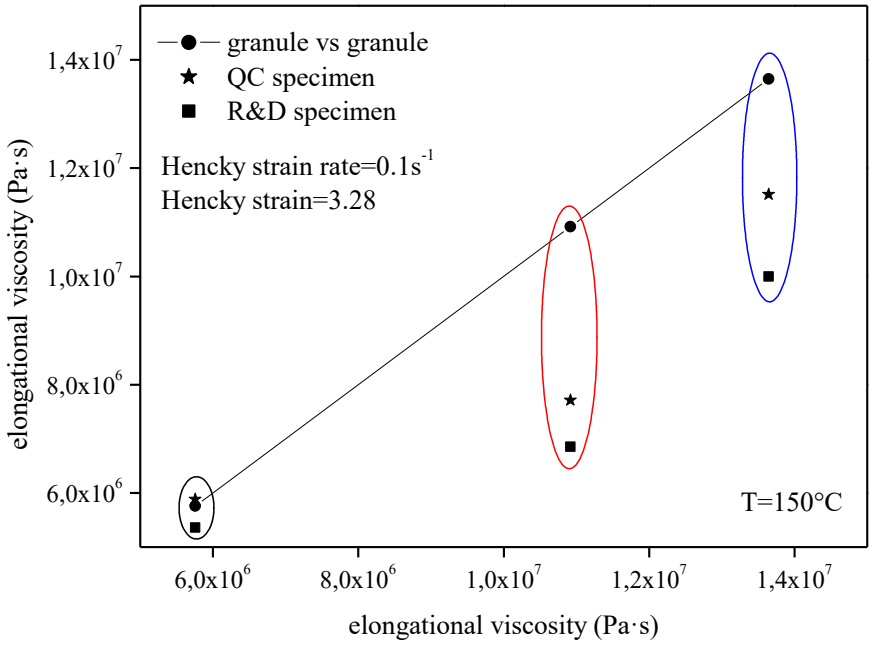

Figure 7. 38: *Elongational viscosity vs elongational viscosity for granules, R&D and QC specimens. R&D specimens have a lower elongational viscosity in support of lower IR.*

By plotting the values of elongational viscosity versus the corresponding values of swelling index Figure 7.39 was obtained. A clear excellent correlation between the elongational viscosity and the swelling index exists, which can be expressed for samples in object and strain conditions the following relation:

$$\eta_{el} = -3.064 \cdot 10^6 + 5.1323 \cdot 10^5 IR \tag{7. 9}$$

It must be stressed that this relation holds only for samples with the same molecular weight and the same particle morphology.

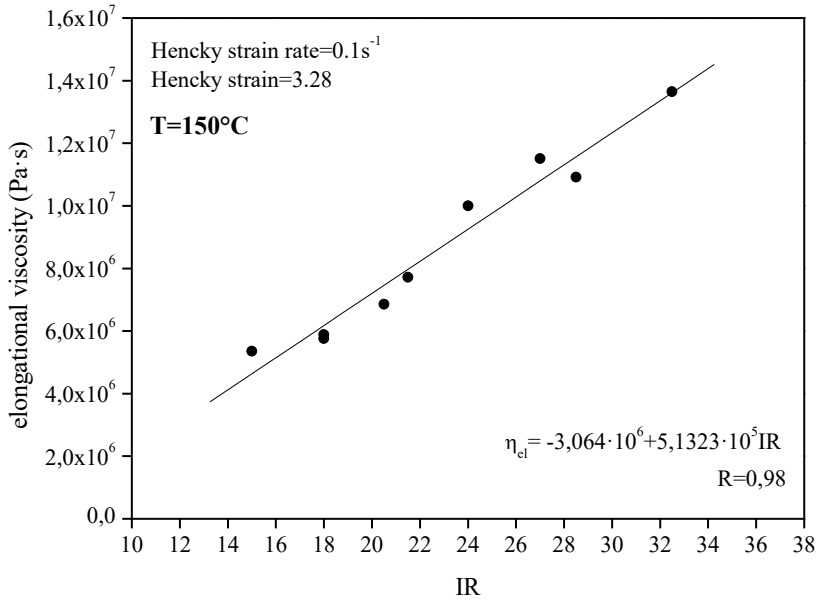

Figure 7. 39: *Correlation between the elongational viscosity and the swelling index IR. The linear fitting of experimental data shows a good correlation between the two properties.*

For completeness the following graphs showing the differences in terms of strain hardening index are also reported.

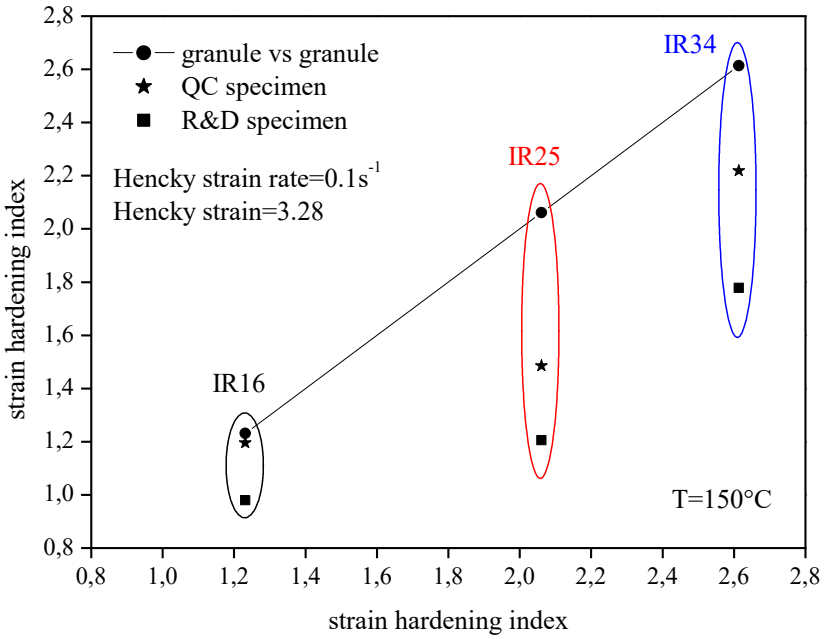

Figure 7. 40: *Strain hardening index vs strain hardening index for granules, R&D and QC specimens. R&D specimens have a lower SHI in support of lower IR.*

Figure 7.40 shows the strain hardening index of the granules, that obviously lie on the bisector of the graph, while molded specimens lie below due to their lower values. The Figure 7.41 shows the strain hardening index versus IR.

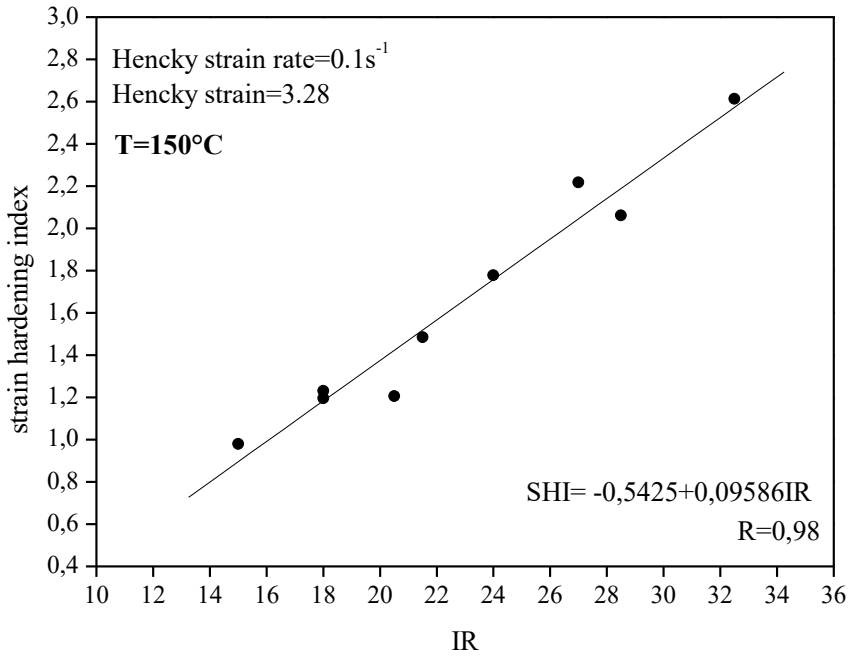

Figure 7. 41: *Strain hardening index vs the swelling index. The linear interpolation of experimental data gives an optimum correlation between the SHI and IR.*

As for the elongational viscosity, a linear relationship between the strain hardening index and the swelling index is highlighted and can be expressed as follows:

$$SHI = -0.5425 + 0.09586 \cdot IR \tag{7. 10}$$

An in-depth future study could lead to the creation of a rheological method to determine the swelling index. This would lead to the elimination of the problems of the traditional technique mentioned before.

7.12 Micrography SEM

To obtain a complete view of the surface morphology of the molded plates, micrographs were taken with a Scanning Electron Microscope (SEM), in collaboration with the Microscopy laboratory of the research center. Each image has been collected at the center of the plate, which was previously coated with gold to make the surface conductive. Figures 7.42, 7.43 and 7.44 show the surface morphology, obtained with secondary electrons, of QC lab standard specimens. The differences of gloss and surface roughness between the three samples is confirmed also by the micrographs. Sample IR16 shows more particles on the surface, although the surface appears less rough compared to sample IR25 and IR34.

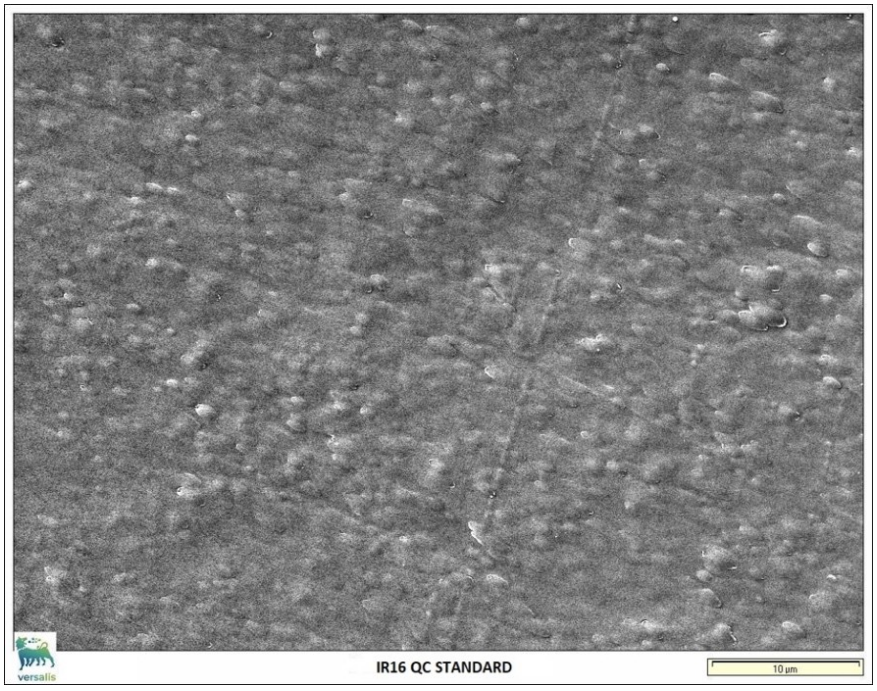

Figure 7. 42: *Micrography SEM of sample IR16 QC standard specimen.*

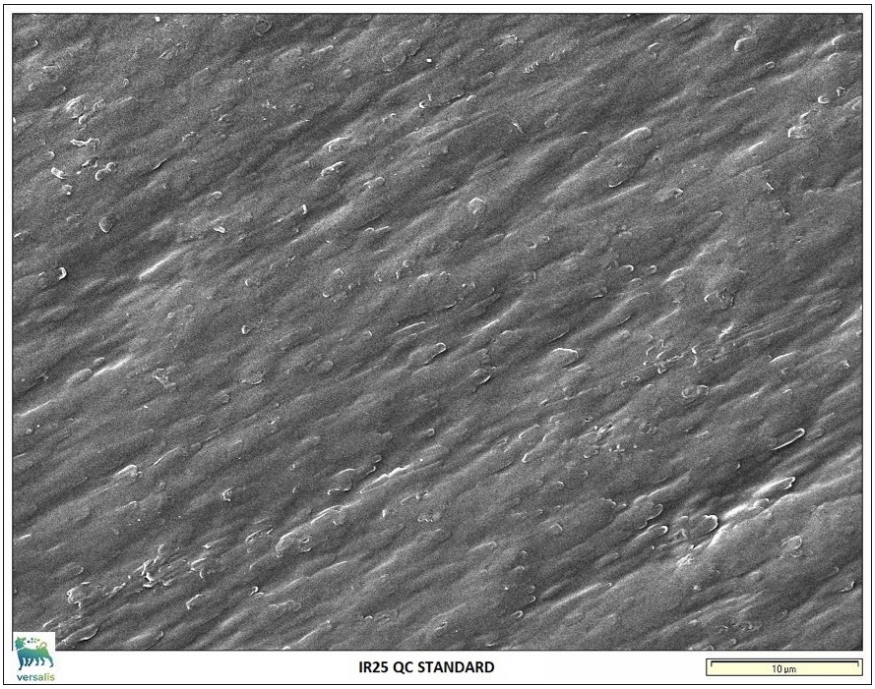

Figure 7. 43: *Micrography SEM of sample IR25 QC standard specimen.*

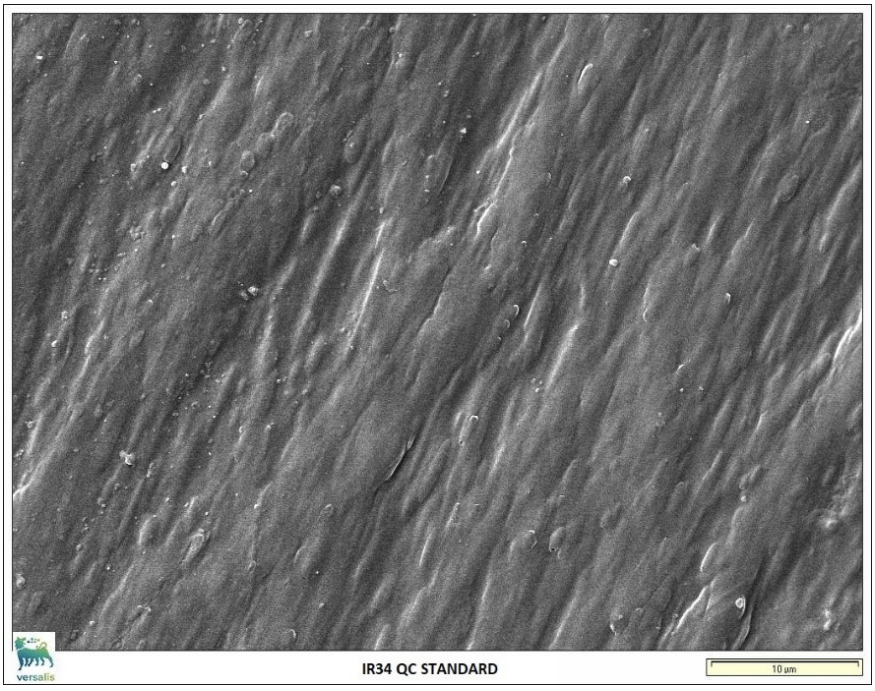

Figure 7. 44: *Micrography SEM of sample IR34 QC standard specimen.*

Figure 7.45 shows the micrographs obtained on samples molded in the condition of T_{mold}=30°C and shear rate of 430s^{-1}, both for R&D and QC labs.

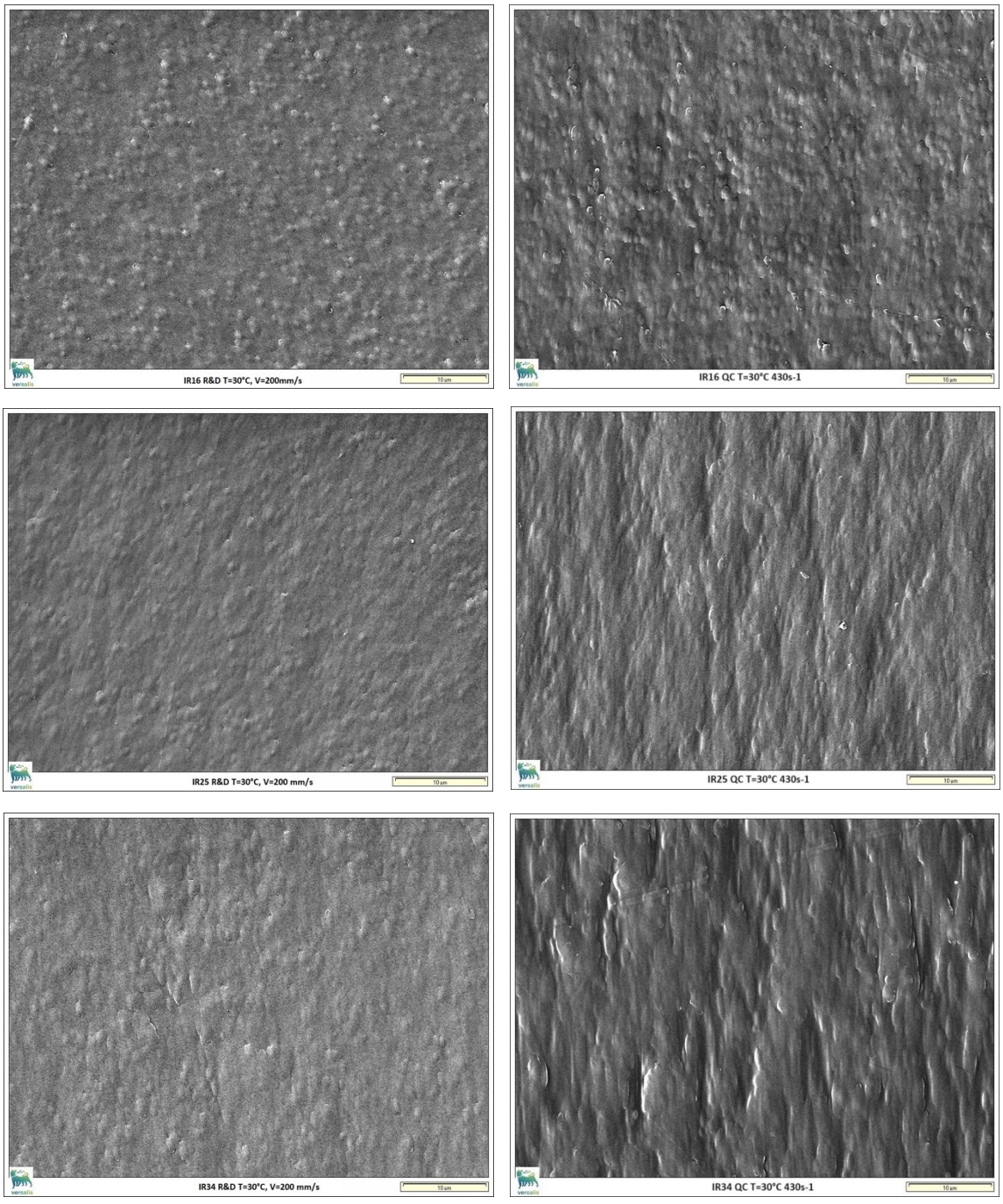

Figure 7. 45: *Micrography SEM obtained with secondary electrons on R&D and QC lab specimens molded in the same conditions (T_{mold}=30°C, shear rate 430s^{-1}).*

Some considerations for Figure 7.45 are reported:

- Sample IR16 shows more spherical particles (less deformed) as expected, for both laboratories,
- QC lab produces a more wrinkled surface, supporting the roughness measures, compared to R&D lab.
- For both labs sample IR16 shows more superficial particles, as if these were migrated to the surface. This aspect could explain the unexpected result, obtained at R&D lab, for which sample IR25 is glossier than sample IR16.

According to what was reported in §3.4, and then the theory on lateral migration of deformable particles, an investigation of this phenomenon using proper simulations is encouraged considering, instead of microchannels, the mold cavity.

In the present case the blockage ratio β is of the order of 10^{-4}, instead of 10^{-1}:

$$\beta = \frac{\emptyset_{particle}}{\emptyset_{mold\ cavity}} \cong \frac{0.6 \cdot 10^{-3}}{3} = 0.0002 \tag{7. 11}$$

The idea that sample IR16 could show more particles on the surfaces could nicely agree with the theory. In fact, although a precise measure of the capillary elastic number is not possible for the samples in object, a guess can be made. Considering Figure 7.5, where the shear stress as a function of shear rate at 220°C is reported, considering the intermediate value of shear rate developed in mold filling (432 s^{-1}) one gets a shear stress value of τ=0.18 MPa. From experimental data obtained in a previous work it is known that the uncross-linked rubber has an elastic modulus equal to 0.85 MPa. Then, for the definition of the elastic capillary number one obtains:

$$Ca_e = \frac{\tau}{G} = \frac{0.18}{0.85} = 0.21 \tag{7. 12}$$

the higher the cross-linking degree of the rubber, the greater the elastic modulus and the lower the Ca_e. Assuming for the sample IR16 a value of G equal to 5 MPa:

$$Ca_e = \frac{\tau}{G} = \frac{0.18}{5} = 0.036 \tag{7. 13}$$

The Deborah number is determined as follows:

$$De = \frac{\tau_{mat}}{\tau_{exp}} = \lambda\dot{\gamma} = 0.1s \cdot 432s^{-1} = 43.2 \tag{7. 14}$$

λ is the relaxation time and could be obtained by the inverse of frequency at which G' and G'' cross each other in the frequency sweep graphs at 220°C, shown in Figure 7.15. The value obtained is 0.1 s, equal for the samples in object. Another method for obtaining λ is from the best fit Cross equation, shown in Figure 7.55 for sample IR34. The value obtained is 0.272 s, comparable to that obtained using frequency sweeps. Considering the theory, by increasing De and decreasing Ca_e, the probability of surface migration is higher and the more prone to migration toward the surface particles of sample IR16 is a hypothesis which is worth taking into account. It still must be verified whether the extremely small blockage ratio values allow the phenomenon. For this reason and for the promising results, numerical simulations are in progress, in collaboration with the University of Naples.

In the meanwhile, an experiment has been carried out to understand if particles of sample IR16 migrate more toward the surface compared to samples IR25 and IR34. The central portion of the plate has been slightly treated with OsO_4, to contrast the most superficial rubber particles and coated with gold to obtain a conductive surface. Then the image has been acquired with backscattered electrons detector. Since they give information on sample morphology, based on different grey levels, particles on the surface will appear whiter, while innermost particles appear darker. Figure 7.46 shows the images for both R&D and QC lab samples. It is possible to see that, as previously seen in Figure 7.44, sample IR16 has a higher concentration of surface rubber particles. This result might suggest the existence of a minimum value of IR below which the gloss would not improve or might even worsen.

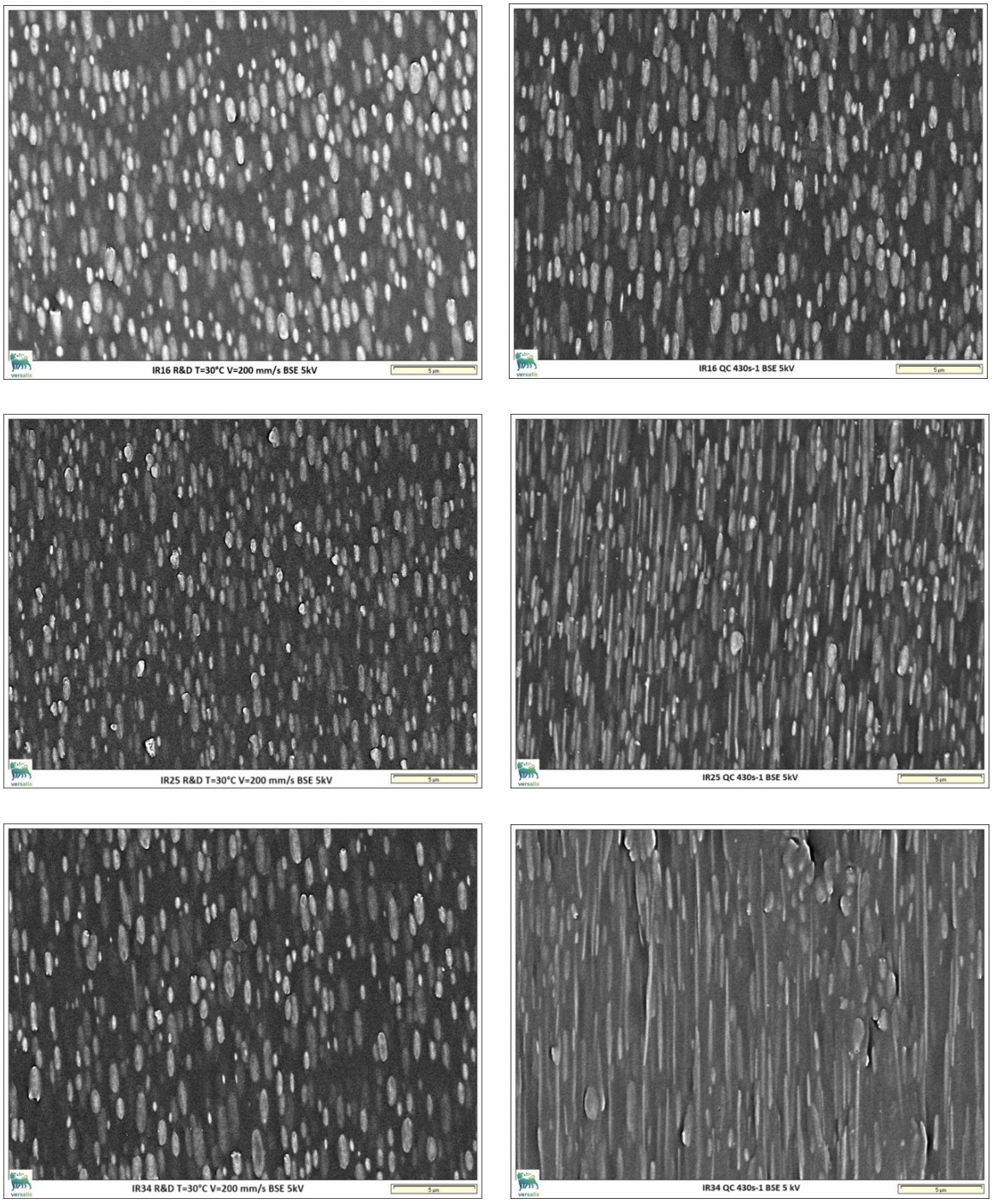

Figure 7. 46: *SEM micrography obtained with backscattered electrons (BSE) with voltage of 5kV, on specimens molded at R&D and QC labs in the same conditions (T=30°C, 430s^{-1}). White points are most superficial rubber particles, while darker points are innermost particles.*

Bucknall [43] showed the mechanism for formation of a matt surface on HIPS describing the undulations on the surface produced by the relaxation of deformed particles in extruded sheet, as shown in Figure 7.47.

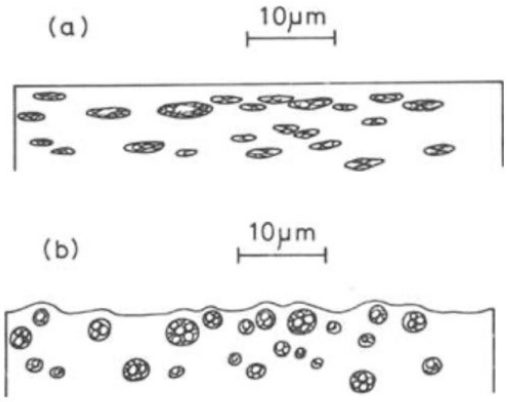

Fig. 11.12 *Mechanism for formation of a matt surface on HIPS:* (*a*) *polymer in contact with die wall or mould surface;* (*b*) *the same region after relaxation.*

Figure 7. 47: *Mechanism for formation of a matt surface on HIPS. a) deformed particles after the extrusion. B) the region after the relaxation of the particles. These have induced the roughness formation on the surface.*[43]

To visualize the elastic recovery of deformed particles the thermal annealing of the plaque of sample IR34 molded at the Quality Control lab has been done. The specimen was put in an oven at 170°C for 15 minutes. Then the surface has been slightly treated with OsO_4, to contrast the rubber phase and then the image was acquired using the BSE detector. Figure 7.48 shows the spherical shape of rubber particles, which have elastically recovered the high frozen stresses, thanks to the high temperature. Furthermore, these have induced in the matrix asperities. In fact, the differential recovery between the matrix and the particles is responsible of the roughness formation, which is as higher as the present orientation on the surface and in the immediately underlying layers. The heat-treated specimen showed as well as an overall volumetric shrinkage a marked matt appearance.

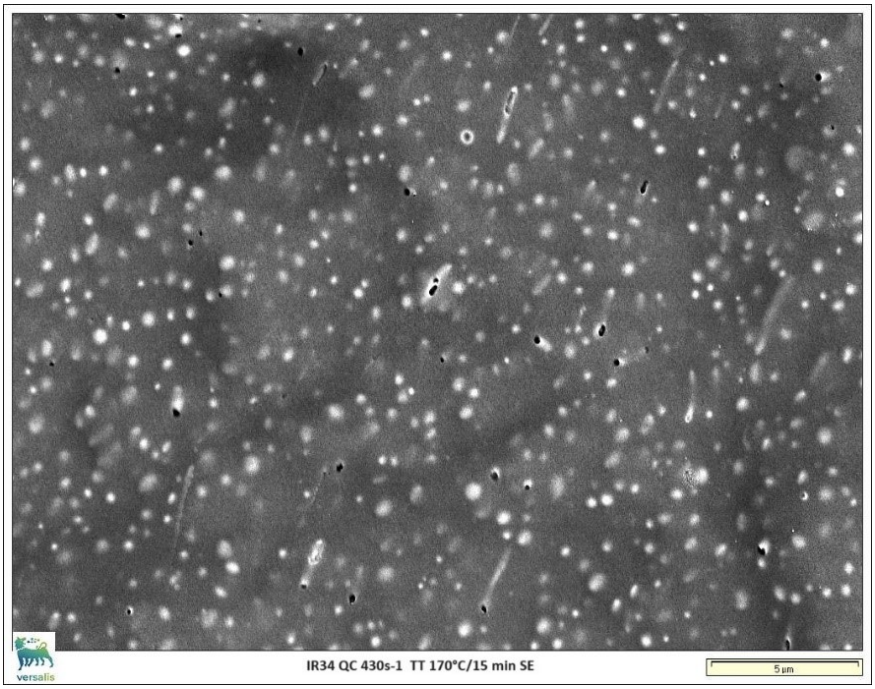

Figure 7. 48: *Surface morphology of sample IR34 molded at QC lab after thermal treatment at 170°C for 15 minutes. Rubber particles show a spherical shape due to the elastic recovery occurred during the thermal treatment.*

For completeness the thermal treatment has been done for all the specimens produced by the two laboratories for the condition of T=30°C and shear rate of $430s^{-1}$.

Table 7. 33*: Thermal annealing of molded plaques. Values % of shrinkage in the flow direction and expansion in the orthogonal direction.*

Thermal treatment of molded plaque: 170°C/15 min			
T=30°C $430s^{-1}$	**Sample**	**Flow direction (%)**	**Orthogonal direction (%)**
R&D	**IR16**	-19.5	5.2
	IR25	-23.9	6.0
	IR34	-23.9	6.1
QC	**IR16**	-22.0	4.4
	IR25	-26.2	4.2
	IR34	-27.0	5.3

Table 7.33 reports the percentual shrinkage values in the flow direction and the percentual of expansion in the orthogonal one. The results show that the plaques of the QC lab

undergo a higher shrinkage in the flow direction, as expected due to the higher orientation seen in micrographs SEM, shown in Figure 7.46.

7.13 Micrography TEM

To visualize the deformability of particles the following experiment has been done. The specimen, shown in Figure 7.18, has been stretched at 160°C with elongational strain rate of 0.1 s^{-1} up to Hencky strain equal to 3, in an EVF test. In this case it was not of interest to measure the elongational viscosity, but to subject samples to equal stretching ratios under controlled conditions. The state of deformation in the sample was frozen in with liquid nitrogen, which was directly sprayed onto the stretched sample by opening the oven once the set deformation had been reached. Figures 7.49, 7.50 and 7.51 have been obtained by photographing with a Transmission Electron Microscope (TEM) the microtomes obtained in the central portion of the stretched specimens, previously treated with OsO_4 to contrast the rubber particles.

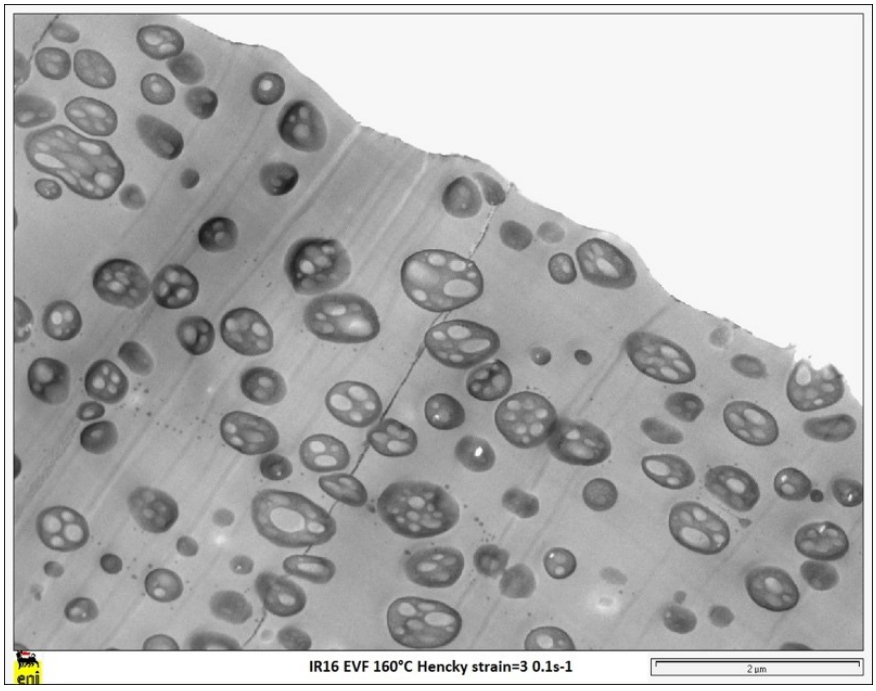

Figure 7. 49: *Micrography TEM on sample IR16 stretched at 160°C with elongational strain rate of 0.1s^{-1} and Hencky strain equal to 3.*

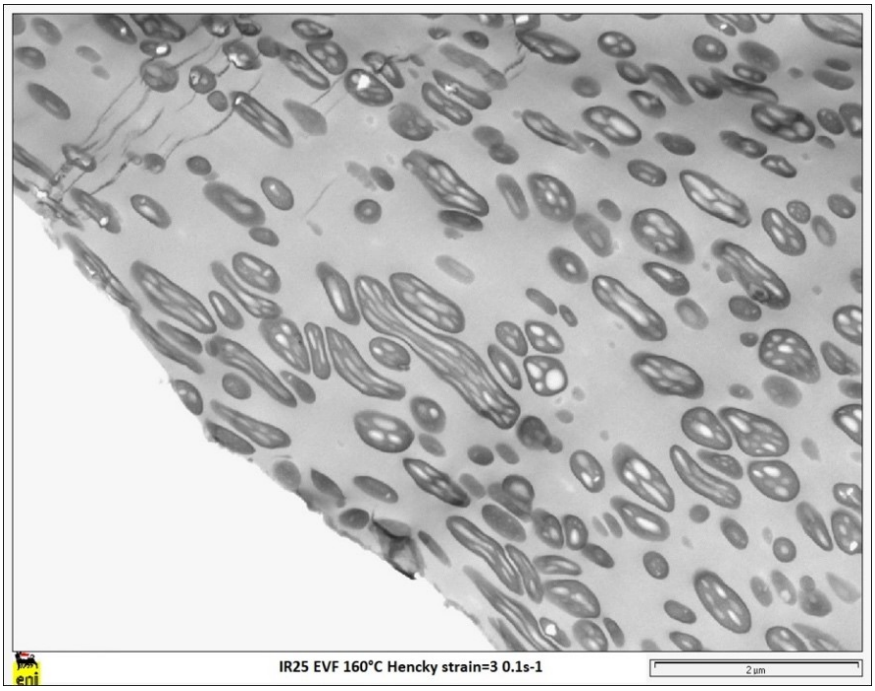

Figure 7. 50: *Micrography TEM on sample IR25 stretched at 160°C with elongational strain rate of $0.1s^{-1}$ and Hencky strain equal to 3.*

Figure 7. 51: *Micrography TEM on sample IR34 stretched at 160°C with elongational strain rate of $0.1s^{-1}$ and Hencky strain equal to 3.*

These images represent the experimental evidence that a higher swelling index leads to higher deformability of rubber particles in an elongational flow. In fact, for the same stretching ratio, sample IR34 shows highly elongated particles. Furthermore, TEM images have been obtained on microtome taken at the center of the QC specimens molded with volumetric flow rate equal to 52 cm^3/s (shear rate of $430s^{-1}$). Figures 7.52, 7.53 and 7.54 show the surface portion, parallel to the flow direction, in which particles are clearly highly oriented in the flow direction, especially for sample IR25 and IR34.

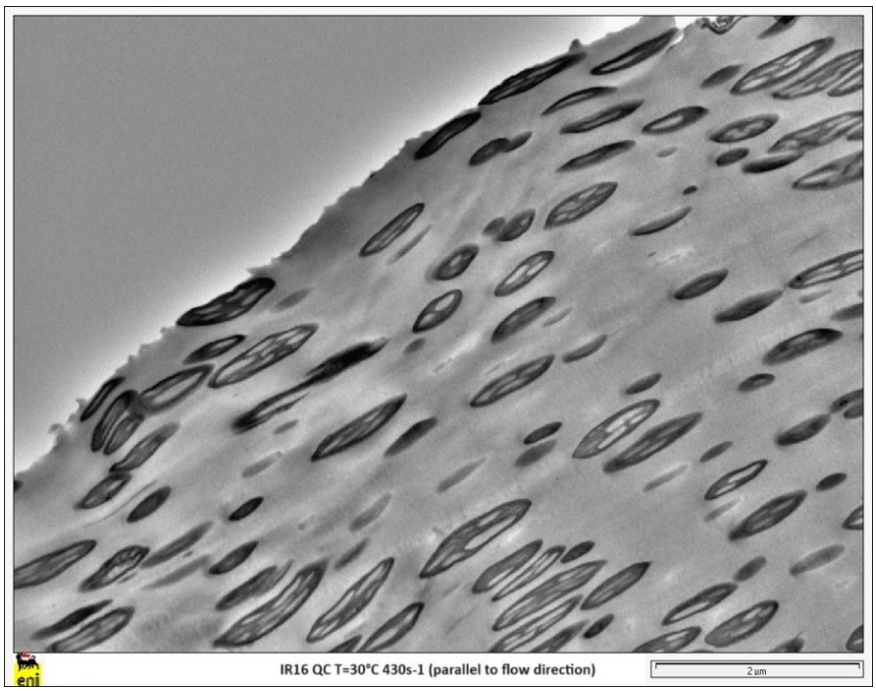

Figure 7. 52: *Micrography TEM on QC specimen IR16 (T=30°C Q=52 cm^3/s). Image obtained at the centre of the specimen near the surface of plaque, in direction parallel to the flow.*

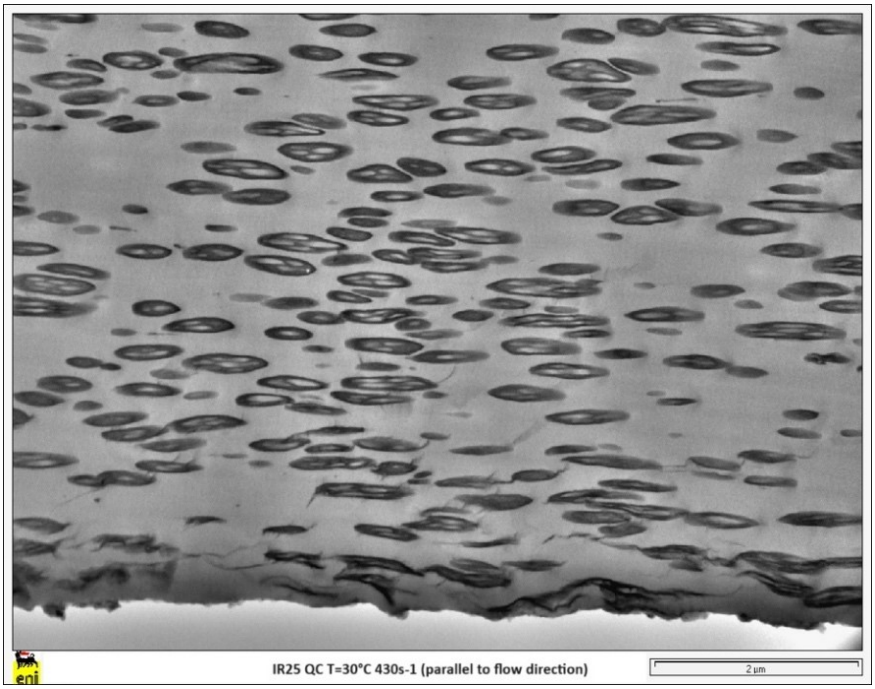

Figure 7. 53: *Micrography TEM on QC specimen IR25 (T=30°C Q=52 cm^3/s). Image obtained at the centre of the specimen near the surface of plaque, in direction parallel to the flow.*

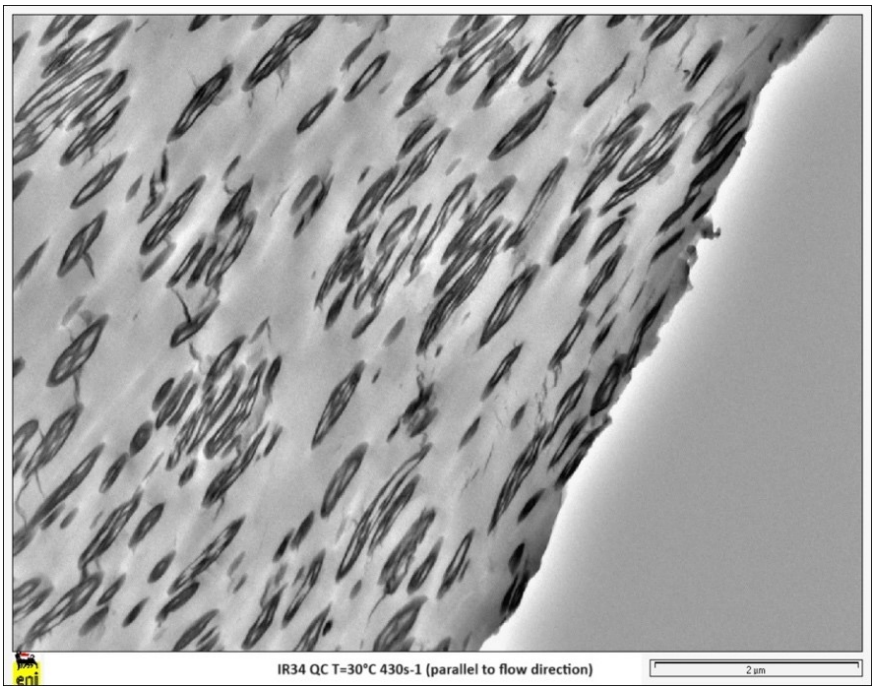

Figure 7. 54: *Micrography TEM on QC specimen IR34 (T=30°C Q=52 cm^3/s). Image obtained at the centre of the specimen near the surface of plaque, in direction parallel to the flow.*

7.14 Simulation of filling stage

To understand whether there may be appreciable differences in the stress distribution in the mold, numerical simulations were conducted. Thanks to the collaboration with the manager of Multiphysic Modelling & Data, the mold filling stage of R&D and QC labs has been analysed with the Simcenter STAR-CCM+, which is a fluid dynamics simulation software. The following assumptions were considered:

- Isothermal conditions (no heat exchange between the melt and the mold, no heating due to viscous friction);
- Constant volumetric flow rate of 36.3 cm^3/s for R&D and 52 cm^3/s for QC, which realize in the rectangular cross-section of both mold cavities, a constant shear rate of 430 s^{-1};
- Constant density of the melt: 0.968 g/cm^3;
- Purely viscous model (viscosity dependent only on shear rate) according to Cross equation (2.8).

Since the samples have the same behavior in shear, the choice of the sample is irrelevant to get the Cross parameters. Figure 7.55 shows the logarithm of viscosity versus shear rate for sample IR34, obtained with capillary rheometer at 220°C.

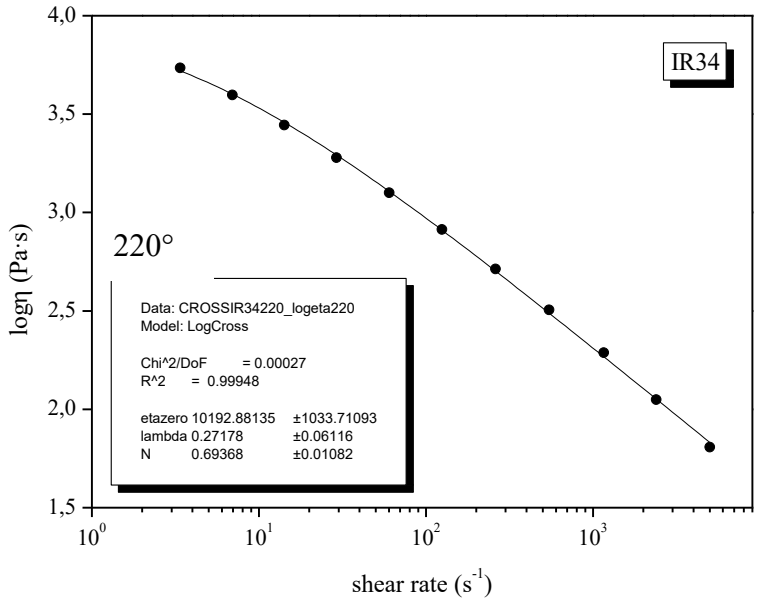

Figure 7. 55: *Cross model at 220°C for sample IR34. Since samples have the same behavior in shear they have the same parameters, and then the same dependency of viscosity on shear rate.*

Experimental points have been fitted with the Cross model, obtaining the following results:

- η_0=10192.88 Poise
- λ= 0.27178
- N=0.69368

Since the axial symmetry of the mold cavities, only semi-geometries of the plates were created in 3D and used for the simulations allowing the reduction of the requested time. The 3D plaques have been subdivided in mesh. These are small finite elements which simulates the response of the structure to the application of certain actions. Obviously by increasing the number of meshes the solutions will be more precise but will also requires much time. The filling stage of the molds takes about half a second. Figures 7.56 and 7.57 show the flow type behavior during the filling stage of R&D and QC mold cavities. The color scale indicates the type of flow, where yellow represents pure shear flow, red pure elongational flow and blue rotational flow. Considering the results of the QC simulation, it seems that immediately after the wringing zone, the elongational component is higher compared to that simulated for the R&D lab mold. Indeed, the geometrical characteristics of the R&D mold cavity were specifically prepared by an ISO commission to be intrinsically able to reduce the orientation during the injection molding process.

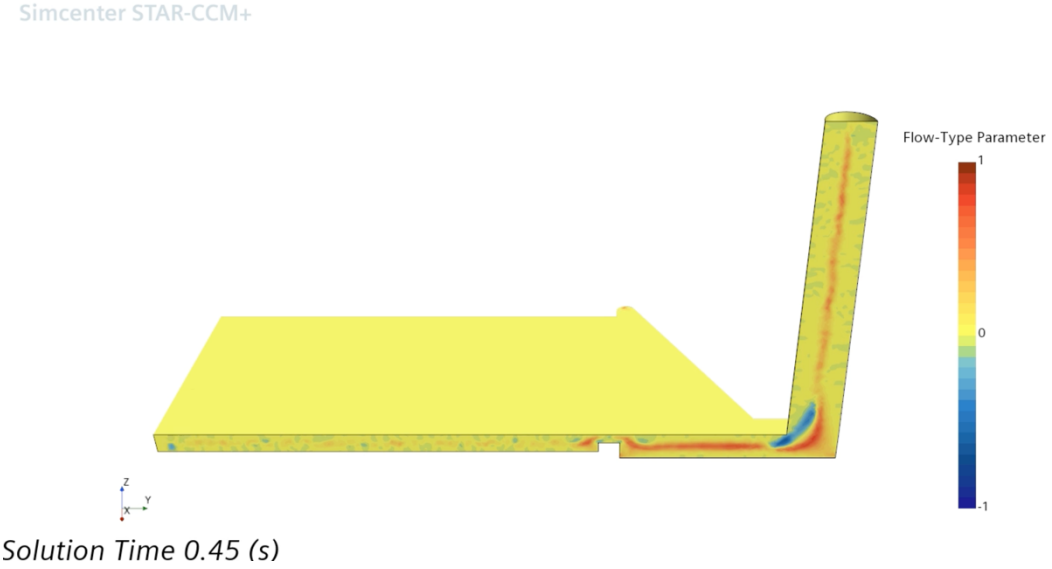

Figure 7. 56: *Flow type behaviors in R&D mold filling. The color scale indicates the type of flow: red represents pure elongational flow, yellow represents pure shear flow and blue rotational flow.*

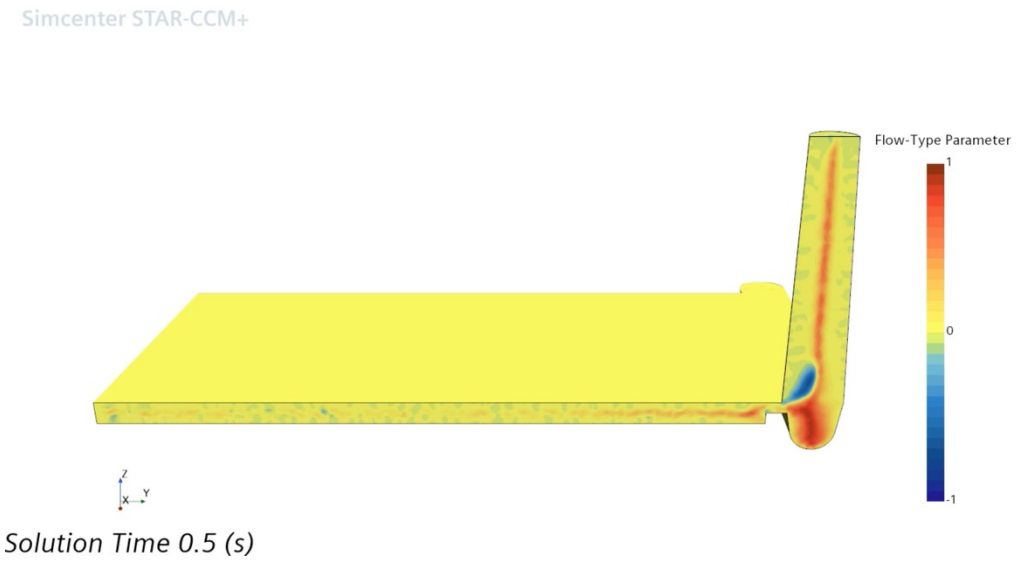

Figure 7. 57: *Flow type behaviors in QC mold filling. The color scale indicates the type of flow: red represents pure elongational flow, yellow represents pure shear flow and blue rotational flow.*

Figures 7.58 and 7.59 show the shear rate profile in the mold cavities. The scale of colors indicates the intensity of shear rate: blue corresponds to zero and red to the maximum shear rate, about 4500 s^{-1}. The maximum shear rate is developed in the wringing zone in QC mold.

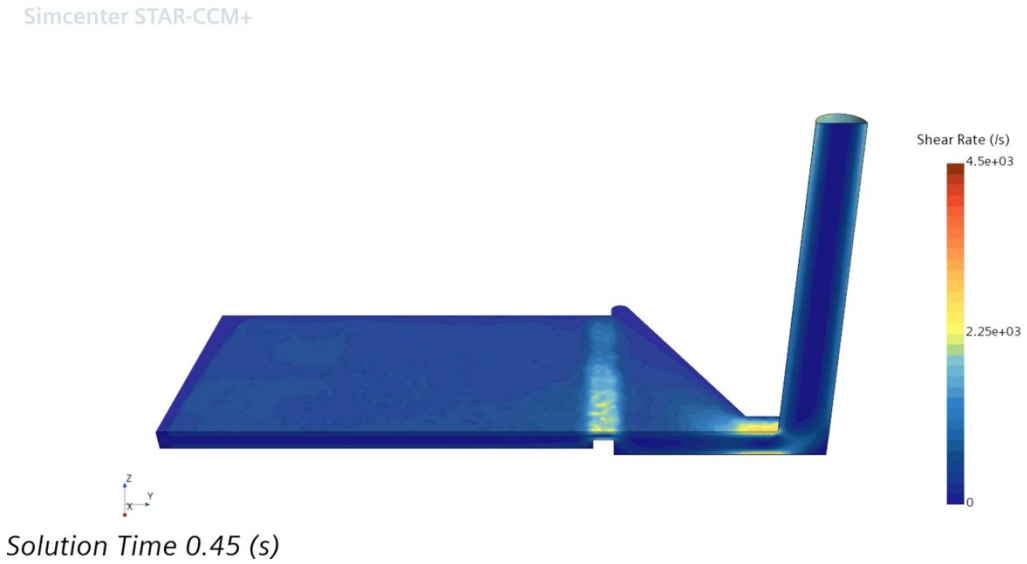

Figure 7. 58: *Shear rate profile in R&D mold filling. The color scale indicates the intensity of shear rate: blue corresponds to zero and red corresponds to the maximum shear rate.*

Figure 7. 59: *Shear rate profile in QC mold filling. The color scale indicates the intensity of shear rate: blue corresponds to zero and red corresponds to the maximum shear rate.*

The developed pressure profile during mold filling is shown in Figures 7.60 and 7.61. As shown in Figure 5.5 the melt pressure increases behind the flow front by increasing the distance from it.

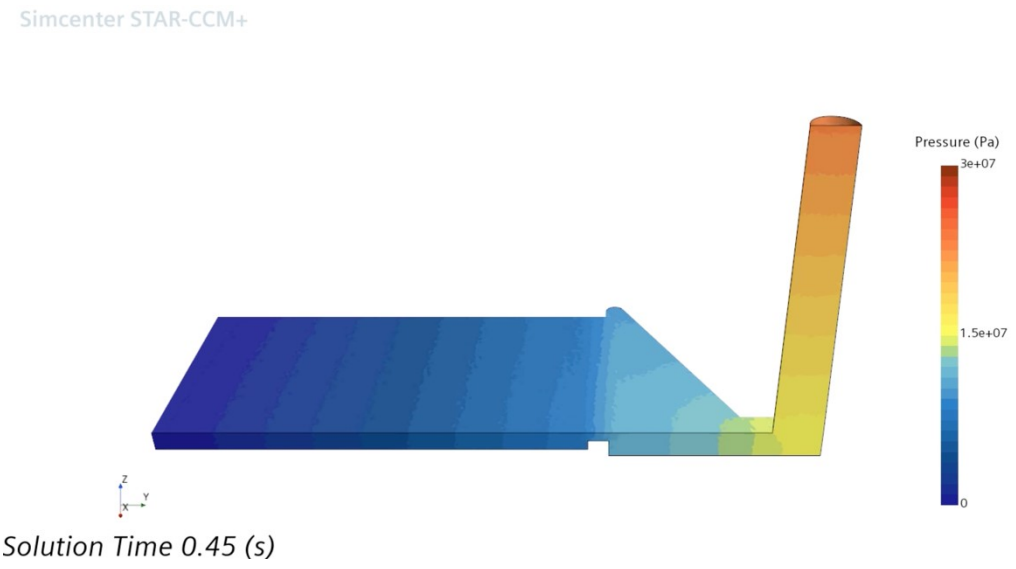

Figure 7. 60: *Pressure profile in R&D mold filling. The color scale indicates the intensity of pressure: blue correspond to zero and red to the maximum pressure.*

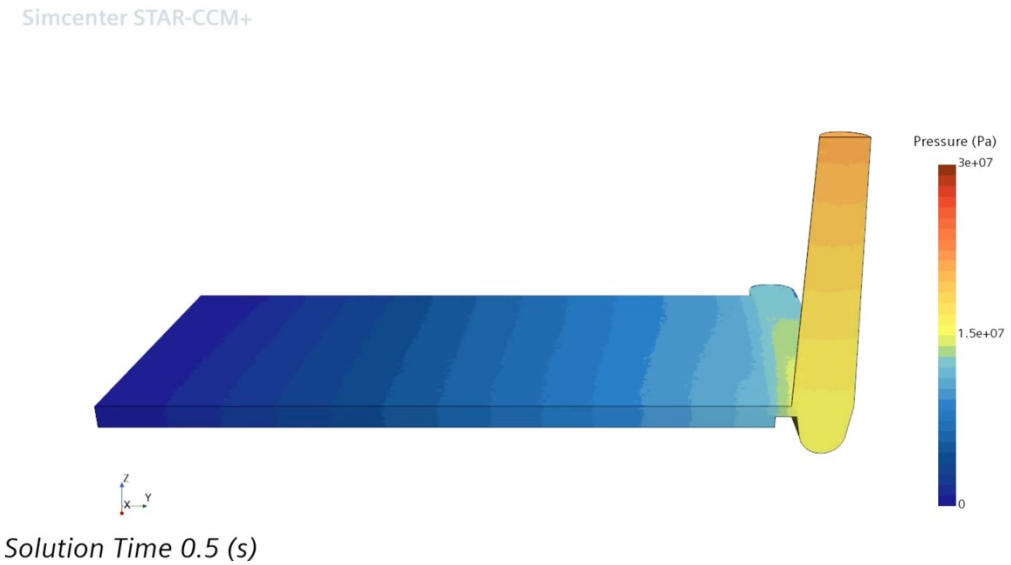

Figure 7. 61: *Pressure profile in QC mold filling. The color scale indicates the intensity of pressure: blue correspond to zero and red to the maximum pressure.*

Indeed, as the simulation suggests, in the areas preceding the flow front, the pressure increases as the mold is filled. This is the reason of the lower pressure at the end of the plaque, which explains the bad replication of the mold and consequently the gloss transition, justified by higher values of roughness at the end. To highlight the presence of fountain flow, a 2D simulation has performed in the central area of the plaque (the length is 1.5 cm and the semi-thickness is 1.5 mm), and by increasing the number of elements of the mesh. Figure 7.62 shows the clearly visible fountain flow developed in the middle section, by setting a flow injection speed of 200 mm/s.

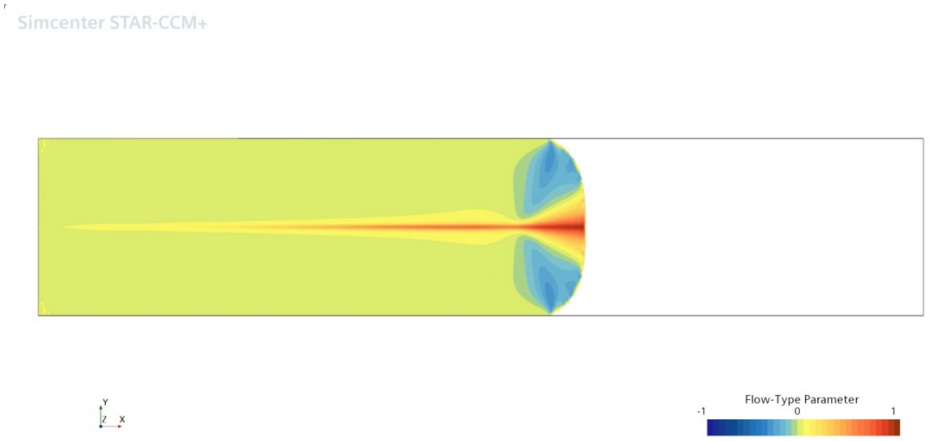

Figure 7. 62: *Fountain flow in the central region of the plaque.*

Some aspects, such as thermal exchange with the mold wall, viscous heating, and viscosity dependency on temperature were ignored for simplicity. In any case, the simulation, although carried out with a low number of elements of the mesh, has highlighted some interesting results. First of all, it confirmed that in the centerline section a pure elongational component exists which stretches the polymer. Then, the simulation showed that the shear rate is nearly zero in the areas in contact with the mold wall and that the pressure at the end of the mold cavity is lower. Future investigations, conducting simulations more closely reproducing real-world conditions and more realistic rheological models, not only the purely viscous one here employed, could explain the origin of the different surface morphology of the plaques molded in the two laboratories, apparently under the same conditions.

CONCLUSIONS

The aim of the present thesis was to try to find a correlation between the cross-linking degree of the rubbery phase and the aesthetic properties of ABS copolymers. Even though the rheological behavior of elastic particles suspended in Newtonian and viscoelastic media is still a matter of study today, for which laborious simulations are needed, this thesis provided interesting results. The great advantage of the present work was the availability of three ABS samples with the same characteristics and differing only for the swelling index (IR), and then the elastic capillary number Ca_e. The literature states that gloss is strictly correlated to the replication factor (R), which could explain its increase by increasing some processing conditions, such as the mold temperature and the flow injection speed. It has been demonstrated that the replication factor is not able to explain the differences between the samples at study. Indeed, these showed the same shear behavior and the same elastic modulus. Since gloss is the macroscopic property which reflects the surface roughness, as suggested by the Simonsen's model, it has been fundamental to understand how the rheological behavior could lead to various surface morphologies in injection molded products. The proposing idea of the different elongational behavior of samples has proven to be valid. In fact, the fountain flow, developed during the injection molding process submit the melt to high elongational rates and contributes to the deposition of the stretched polymer onto the mold walls. In this way it represents the source of the high orientation on the surface. Depending on the particle deformability, the three samples showed different elongational behaviors and different surface morphologies. The highest elastic recovery of sample IR34 resulted in highest roughness values and lowest gloss values. As seen, the increase of flow injection speed acts in opposite way: on one hand it increases the melt pressure, favoring the replication, on the other hand it increases the orientation, enhancing the roughness formation. For sample IR34, which appears to be the most susceptible to deformation and orientation, the increase in melt pressure is compensated, leading to almost the same gloss value in QC specimens. For biphasic materials, such as ABS, there is also a differential shrinkage between the elastic particles and the glassy matrix during the cooling process.

Furthermore, it has been showed that the phenomenon of particle migration, for which particles with lower elastic capillary number are more prone to migrate toward the surface, is possible. That could be the reason of the unexpected result of R&D lab and for the possible existence of a minimum value of IR beyond which gloss does not improve or may even worsen. Thus, at least three different contributions to the formation of surface roughness are suggested: the differential shrinkage between the matrix and the rubber particles in the frozen layer, the relaxation mechanism of the compression state in the frozen layer, induced by the bulk polymer and the surfacing of more rigid particles. The use of different injection molding machines had uncovered unexpected and interesting results. At first, even if one tries to replicate the molding conditions the same results are not necessarily obtained. Furthermore, the determination of the IR values on molded specimens highlighted the rubber modification during the injection molding process. Indeed, the process significantly reduces the IR values, especially when this is high. Last but not the least, the EVF tests performed on granules and on the molded specimens allowed to find a good correlation between the elongational viscosity and the swelling index, which with future in-depth studies could lead to the development of a rheological method for its quick and easy determination.

Bibliography

1. Echte, A. (1989). Rubber-Toughened Styrene Polymers. A review. In: *Rubber-Toughened Plastics*. Advances in Chemistry, Vol.222, American Chemical Society, Washington DC (U.S.A.).
2. https://www.researchgate.net/figure/Chemical-structure-of-ABS-PS-and-PVC_fig2_328589758
3. Karl Fink, J. (2010). *Handbook of Engineering and Specialty Thermoplastics: Polyolefins and Styrenics*. Wiley-Scrivener Publishing LLC, Vol.1, p.211-267.
4. https://skill-lync.com/blogs/the-02-percent-offset-method-for-yield-stress
5. https://it.wikipedia.org/wiki/Fluido_non_newtoniano#:~:text=Fluidi%20come%20le%20vernici%20sono,in%20generale%2C%20dai%20fluidi%20polimerici.
6. https://www.goettfert.com/application-knowledge/rheo-info/for-capillary-rheometer/modeling-of-viscosity-data
7. Enciclopedia degli idrocarburi, Vol.5, p.249-261.
8. https://it.wikipedia.org/wiki/Viscoelasticità
9. https://www.researchgate.net/figure/ELASTIC-AND-VISCOUS-RESPONSE-TO-STRESS_fig13_323424698
10. https://www.researchgate.net/figure/Comparison-of-calculated-and-exact-shift-factors_fig4_251307514
11. https://www.researchgate.net/figure/Concept-of-time-temperature-superposition-TTS-principle-and-master-curve-formation_fig1_336933350
12. Villone, M.M and Maffettone, P.L. (2019). Dynamics, rheology, and applications of elastic deformable particle suspensions: a review. *Rheologica Acta*, **8**, p.109–130.
13. Villone, M.M *et al*. (2016). Numerical simulations of deformable particle lateral migration in tube flow of Newtonian and viscoelastic media. *Journal of Non-Newtonian Fluid Mechanics*, **234**, p.105-113.
14. https://www.3ds.com/it/make/guide/process/injection-molding
15. https://easchangesystems.com/application/plastic-injection-molding/
16. Tadmor, Z. and Gogos, Costas G. (2006). *Principles of Polymers Processing*. John Wiley & Sons, Inc., p.753-783.

17. https://www.mdpi.com/2504-477X/4/1/11
18. Mavridis, H. *et al.* (1988). The Effect of Fountain Flow on Molecular Orientation in Injection Molding. *Journal of Rheology*, **32**, p.639-663.
19. Tadmor, Z. (1974). *Molecular orientation in injection molding*. Journal of Applied Polymer Science 18.6: 1753-1772.
20. Gim, J. and Turng, L. (2022). A review of current advancements in high surface quality injection molding: Measurement, influencing factors, prediction, and control. *Polymer testing*, **115**.
21. https://www.elcometer.com/en/how-to-measure-gloss-using-a-gloss-meter
22. Lednicky, F. and Pelzbauer, Z. (1986). Gloss as an Inner Morphology Characteristic of ABS Polymers. *Die Angewandte Makromolekulare Chemie*, **141**, p.151-160.
23. Gim, J. and Rhee, B. (2020). Generation mechanism of gloss defect for high-glossy injection-molded surface. *Korea-Australia Rheology Journal*, **32(3)**, p.183-194
24. Gim, J. *et al*. (2020). Causes of the Gloss Transition Defect on High-Gloss Injection-Molded Surfaces. *Polymers*, **12,** 2100.
25. Hirano, K. *et al.* (2007). Morphological Analysis of the Tiger Stripe on Injection Molding of Polypropylene/Etylene-Propylene Rubber/Talc Blends Dependent on Based Polypropylene Design. *Journal of Applied Polymer Science*, Vol. **104**, Issue 1, p.192-199.
26. Alexander-Katz, R. and Barrera, R.G. (1998). Surface correlation Effects on Gloss. *Polymer Physics*, Vol. **36**, Issue 8, p.1321-1334.
27. Simonsen, I. *et al*. (2005). Estimation of gloss from rough surface parameters. *Physica status solidi*, Vol. **242**, Issue 15, p.2995-3000.
28. González-Henríquez, C.M and Rodríguez-Hernández, J. (2019). *Wrinkled Polymer Surfaces Strategies, Methods and Applications*. Springer Cham, p.3-39.
29. Manual Micro-Tri-Gloss BYK. https://www.byk-instruments.com/it/Appearance/micro-gloss-Glossmetro/c/2343
30. https://luminusdevices.zendesk.com/hc/en-us/articles/4413632829581-What-is-a-Standard-Illuminant-Reference-Illuminant-
31. https://www.rheologylab.com/services/dynamic-mechanical-analysis-dma/
32. RSA-G2 TA Instruments. https://www.tainstruments.com/rsa-g2/

33. Ferri, D. (2006). Reometria di polimeri in regime oscillatorio. Παντα ρει
34. RG20 Göettfert. https://www.goettfert.com/products/capillary-rheometer/rheograph-20
35. Manual ARES Rheometer - TA Instruments. PN 902-30026 Rev.D June 2003 https://www.mrl.ucsb.edu/sites/default/files/mrl_docs/instruments/ares_user_manual.pdf
36. https://www.researchgate.net/figure/Schematic-of-the-extensional-viscosity-fixture-EVF_fig16_243529712
37. https://www.researchgate.net/figure/Schematic-depiction-of-strain-softening-in-shear-and-hardening-in-extension-in-terms-of_fig1_235918962
38. https://slideplayer.it/slide/957411/3/images/13/DIN+4760+Deutsches+Institut+f%C3%BCr+Normung.jpg
39. https://advancedopticalmetrology.com/glossary/profile-method.html
40. https://www.rrutc.msm.cam.ac.uk/outreach/articles/the-scanning-electron-microscope
41. https://microbenotes.com/transmission-electron-microscope-tem/
42. ASTM D523-14. Standard Test Method for Specular Gloss.
43. Bucknall, C.B. (1977). *Toughned Plastics*. (L. Holliday and A. Kelly, F.R.S., Ed.), Applied Science Publishers, London.

Ringraziamenti

Finalmente ci siamo, è giunto il momento di ringraziare tutte le persone che mi hanno aiutata in questo lungo e difficile percorso.

Desidero ringraziare il Prof. Michele Modesti, che, senza indugiare e con grande disponibilità, ha accolto la mia richiesta di tirocinio.

Un ringraziamento all'Ing. Silvia Zanatta, la cui estrema gentilezza e disponibilità hanno aiutato a tranquillizzarmi.

Un enorme grazie va al mio tutor, Dott. Dino Ferri, che mi ha dato la grandissima opportunità di far parte, seppur per poco tempo, di una grande realtà aziendale come Versalis. Mai avrei pensato che il mondo della ricerca potesse fare al caso mio e invece la passione che dedichi al tuo lavoro mi ha sempre stimolata nel cercare le risposte alle continue domande che ci ponevamo.

Ai miei compagni di laboratorio, Fabio e Luigi, che mi hanno aiutata in tutto e per tutto. Un sentito grazie anche a tutte le persone di Versalis che hanno fatto parte di questo bellissimo percorso, nominarvi tutti sarebbe impossibile.

Il ringraziamento più importante va alla mia mamma, che nonostante tutto ha sempre trovato la forza di reagire e starmi a fianco. Mi hai sempre supportata (e sopportata) in ogni scelta ed in ogni momento difficile. Grazie di cuore.

Un grazie al mio fratellone. Nonostante la distanza ci abbia diviso da un po' di tempo, sappiamo che ci saremo sempre l'uno per l'altra.

E ora i ringraziamenti più difficili per me, quanto vorrei poteste sentirli.

Grazie ai miei nonni, che mi sono sempre stati vicini e non mi hanno mai fatto mancare nulla.

Grazie alla mia stella più luminosa, tutta la forza e la determinazione che mi hai trasmesso mi hanno portato ad essere la persona che sono. So con tutta me stessa che saresti stato immensamente fiero. Questo traguardo è per te, Papà.